

CONFIDENTIAL

System design and control of a novel ocean wave energy converter array

Luc Hogervorst

Master of Science Thesis

MSCCONFIDENTIAL

System design and control of a novel ocean wave energy converter array

MASTER OF SCIENCE THESIS

For the degree of Master of Science in Systems & Control and
Biomechanical Design at Delft University of Technology

Luc Hogervorst

November 5, 2019

Faculty of Mechanical, Maritime and Materials Engineering (3mE) · Delft University of
Technology



Copyright © Delft Center for Systems and Control (DCSC)
All rights reserved.



Abstract

There is a great amount of wave power in earth's oceans. The amount of power harvested for electricity is however very small in comparison to solar and wind. One of the reasons for this is the lack of consensus on the best design of wave energy converters. This thesis develops a novel system design for a wave energy converter array that has promise and implements, evaluates and compares control for it. The most important benefits of this new design versus the most used type of devices are that it does not rely on a connection to the ocean floor for energy harvesting and it is space efficient, meaning that devices lie close together. Control has never been designed for the type of device in this study to the best of this author's knowledge.

The wave energy converter array consists of floating pontoons that are connected to each other. The wave energy is harvested through power take-off mechanisms in these connections. The most important requirement on the system design is survivability, as the ocean is a harsh environment. The kinematics are thus designed in such a way that forces on the connections can be set by the damping and stiffness coefficients of the connections. The array is optimized for efficient energy harvesting by its design, while keeping cost effectiveness in mind when possible.

Not only the array itself is optimized for efficiency, the control is optimized for this as well. This means that the control problem is to maximize energy capture. Reactive and Resistive control are implemented and compared. A distributed version of these algorithms is investigated as well and improves on computation time for large arrays. Reactive control can improve upon Resistive control up to three times in terms of energy capture, depending on the efficiency of the power take-off mechanism. The reason for this great improvement is that Reactive control makes it possible for the array to reach resonance with the waves. The array performs average in terms of energy capture in comparison to other wave energy converters when Resistive control is used.

Table of Contents

Preface	xiii
Acknowledgements	xv
1 Introduction	1
1-1 Global warming	1
1-2 Wave energy converters	2
1-3 Goals of this study	3
1-4 Layout of this report	3
2 Mechanical Analysis	5
2-1 Introduction	5
2-2 Mechanical Analysis	6
2-3 Design problem formulation	8
2-4 Strategy selection	10
3 System Design	13
3-1 Analysis and design requirements	13
3-2 Type and number of generators	15
3-3 Generator placement	16
3-4 Top view pontoon shape and number of connections	17
3-5 Spacing and size of pontoons	18
3-6 Final system design	19

4	Modelling and simulation	21
4-1	Wave theory	21
4-1-1	Water waves	21
4-1-2	Waves at sea	23
4-1-3	Wave power	24
4-2	Mathematical modelling of wave energy converters	25
4-2-1	Differential equations for wave energy converters	25
4-2-2	Computation of hydrodynamic coefficients	25
4-2-3	Computation of wave forces	26
4-2-4	Computation of power take-off forces	28
4-2-5	Computation of electric power	30
4-2-6	Simulation	30
4-3	Model simplification	30
4-4	Model verification	31
5	Control	39
5-1	The control problem	39
5-2	Resistive and Reactive control	40
5-3	Distributed control	41
5-4	Stability	43
6	Results	47
6-1	Pontoon movement	47
6-2	Simulation duration	48
6-3	Energy production per generator	48
6-4	Influence of the number of pontoons on energy capture	49
6-5	Influence of pontoon spacing on energy capture	50
6-6	Influence of pontoon height on energy capture	50
6-7	Sea states overview	51
6-8	Waves at a 45° angle	52
6-9	Scalability control method	52
7	Discussion	53
7-1	Eigenvalue analysis	53
7-2	Comparison with other wave energy converters	54
7-3	Improvement on energy capture with more wave information	56
8	Proof of concept	59
8-1	Top view design	59
8-2	Power take-off mechanism	60
8-2-1	Dampers	60
8-2-2	Springs	64
8-2-3	Attachment of power take-off mechanisms to pontoons	65
8-3	Energy capture	67

9	Conclusions and recommendations	69
9-1	Conclusions	69
9-2	Recommendations	69
A	Optimal damping constants of simplified energy harvesters	71
A-1	Optimal damping constant for mass damper system A	72
A-2	Optimal damping constant for mass damper system B	73
B	Motion of generators for two different generator placements	75
C	Computation of hydrostatic and gravitational stiffness coefficient in pitch	77
D	Extra Data	79
D-1	Ten consecutive optimization runs	79
D-2	Energy harvested per sea state	79
D-3	Spring and damping constants	79
E	Efficiency of springs	83
	Bibliography	85
	Glossary	93
	List of Acronyms	93
	List of Symbols	93

List of Figures

1-1	(A) Photo of the Wavestar wave energy converter. (B) Working principle of the arms of the Wavestar. From Ferri et al. [10].	2
1-2	Schematic drawing of an oscillating water column type wave energy converter, from Hashem et al. [12].	3
2-1	Examples of wave energy converters from literature; (a) the DEXA [14], (b) the Wave Dragon [15, 16].	5
2-2	Energy flow through a wave energy converter.	6
2-3	Schematic drawing of magnets moving inside a coil (ferromagnetic cores). Only part of the coil is drawn. Adapted from Graves et al. [28].	8
2-4	Three types of one-dimensional energy harvesters. Power take-off mechanism is displayed as a spring and damper. Adapted from Hogervorst [13].	9
2-5	Wave directions for location 52.528°N, 2.304°NE, from Geos [29].	11
3-1	Starting point of the system design. Top: side view of two floating bodies with the possibility to connect them with linear or rotary generators. The generators are dashed because it is not decided yet how they are connected to the pontoons. Bottom: legend.	14
3-2	Conceptual solutions with 3 generators.	15
3-3	Torque on a mechanism with two linear and one rotary generator. Applied torque is indicated with anticlockwise arrows and resultant forces perpendicular on the linear generators with straight arrows.	16
3-4	Generator placement for minimum length of connection beam.	17
3-5	Top view of arrays; (a) triangular array, (b) square array.	18
3-6	Visualisation of the difference in center to center distance between subsequent pontoons for 0° and 45° wave direction.	19
3-7	Final system design of the $2 \times n$ array connected with linear generators. Dominant wave direction is indicated with an arrow.	20
4-1	Wave parameters, adapted from Newman [32]. Arrows indicate water particle movement.	22

4-2	Domains of wave theory, adapted from Hedges [33].	22
4-3	JONSWAP wave spectrum for north sea waves with $H_s = 2.25$ m and $T_p = 6.50$ s.	24
4-4	Hydrodynamic coefficients in surge for a single pontoon.	26
4-5	Hydrodynamic coefficients in heave for a single pontoon.	27
4-6	Hydrodynamic coefficients in pitch for a single pontoon.	27
4-7	Computation time of hydrodynamic coefficients and wave excitation force factors in NEMOH versus the number of pontoons with 884 panels.	28
4-8	Schematic of two pontoons with definitions of angles and pontoon width.	28
4-9	Block diagram for the simulation of the wave energy converter array in this work.	31
4-10	Comparison of magnitude of simplified wave excitation force factors (dashed) with computed wave excitation force factors (solid) for a 3×1 array. Wave excitation force factor in surge (a), in heave (b) and wave excitation moment factor in pitch (c).	32
4-11	Comparison of phase of simplified wave excitation force factor (circle) with computed wave excitation force factor (cross) for the third pontoon.	33
4-12	Added mass in x (11), y (22) and z (33) direction, computed by Killi [44] (left) and in this work (right) for a rectangular pontoon.	35
4-13	Added damping in x (11), y (22) and z (33) direction, computed by Killi [44] (left) and in this work (right) for a rectangular pontoon.	35
4-14	Wave excitation force factors in x (11), y (22) and z (33) direction, computed by Killi [44] (left) and in this work (right) for a rectangular pontoon.	36
4-15	Hydro-dynamic coefficients in pitch computed by Abul-Azm and Gesraha [46] (left) and in this work (right) for a long square pontoon. On the horizontal axis is the wave number multiplied with half of the pontoon width.	36
4-16	Pitch angle for a 2×1 array, where the pontoons are connected with an 'infinitely stiff' connection and pitch angle for a large pontoon that has the same dimensions as the two pontoons summed. Simulated for random waves with $H_s = 2.25$ m, $T_p = 6.50$ s and a 0° wave direction.	37
4-17	Video snippet from the visualization of a 2×1 array under random seas with a 0° wave direction.	37
5-1	Block diagram for low level Resistive and Reactive control. $K_p = 0$ for Resistive control.	40
5-2	Nelder-Mead simplex method actions. Solid line is the old simplex and dashed line is the new simplex.	41
5-3	Scheme of the overarching control method for Resistive and Reactive control. Adapted from [49].	42
5-4	Power generated and used by the power take-off mechanism of a 2×1 array. Simulated for random seas with $H_s = 2.25$ m, $T_p = 6.50$ s and waves coming at 0°	42
5-5	Distributed control scheme.	43
5-6	Bode plot from force to displacement of the power take-off mechanism.	44
5-7	Bode plot of the loop transfer with Resistive Control.	45
5-8	Bode plot of the loop transfer with Reactive Control.	45
6-1	Top view of a 4×1 array with 0° wave direction indicated by the arrow.	47

6-2	Example of typical horizontal (x) and vertical (z) displacement of the two pontoons with respect to their starting position in a 2×1 array. Simulated for random seas with $H_s = 2.25$ m, $T_p = 6.50$ s and waves coming at 0°	48
6-3	Relative increase in energy when an extra pontoon is added to the array. Simulated for random seas with $H_s = 2.25$ m, $T_p = 6.50$ s and waves coming at 0°	49
6-4	Energy capture versus pontoon spacing for a 2×1 array. Simulated for random seas with $H_s = 2.25$ m, $T_p = 6.50$ s and waves coming at 0°	50
6-5	Energy capture versus pontoon height for a 2×1 array. Simulated for random seas with $H_s = 2.25$ m, $T_p = 6.50$ s and waves coming at 0°	50
6-6	Number of optimization iterations versus number of pontoons for a 2×1 array. Simulated for random seas with $H_s = 2.25$ m, $T_p = 6.50$ s and waves coming at 0°	52
7-1	Mass-spring model for the array.	54
7-2	Capture width ratio for wave energy converter types and sizes, from Babarit [58].	56
7-3	Comparison of energy capture between arrays in monochromatic and random waves. The improvement factor is computed by dividing energy capture of arrays in monochromatic waves by energy capture in random waves.	57
8-1	Top view of the proof of concept design. Pontoons are drawn in black, connections in red and the blue arrow is the dominant wave direction.	59
8-2	Schematic of the hydraulic part of the power take-off mechanism. Adapted from Cargo et al. [61].	60
8-3	Working principle of a variable displacement motor, from [72].	61
8-4	Forces exerted by optimized power take-off mechanism of a 2×1 array in random seas with $H_s = 6.50$ m, $T_p = 6.50$ and 0° wave direction.	63
8-5	Schematic drawing of hydraulic piston mechanisms.	63
8-6	Schematic drawing of a variable winding spring. Overall drawing: Top view of mechanism with part of array. Zoomed drawing: Top view and front view of mechanism.	65
8-7	Data [74] and extrapolation for the minimum tensile strength of chromium silicon steel SAE J157.	66
8-8	Render of a 2×2 array.	67
A-1	Simplified energy harvesters with mass m , damping constant b , vertical displacement of mass z and gear ratio n	71
B-1	Generator placement; (a) rotary generators on either end of the pontoons, (b) rotary generators in the middle of the pontoons.	75
C-1	Side view of a rotated pontoon in still water with hydrostatic and gravitational forces indicated by arrows. The orange dashed line indicates the water level. The blue area is above water when in rest, but under water when rotated and the red area is under water in rest, but is above water when rotated.	78
C-2	Triangle and its center of gravity.	78
E-1	Example of the displacement of an arbitrary spring with an efficiency of 0.78 after it is released from an initial position.	84

List of Tables

2-1	States of matter and forms of mechanical energy.	6
2-2	Occurrence of sea states in percentage for a location 35 km off the coast of England (52.528°N, 2.304°NE). Wave peak period T_p (s) is on the horizontal axis and significant wave height H_s (m) on the vertical. Adapted from Geos [29].	10
2-3	Power per sea state in percentage of total power for location 52.528°N, 2.304°NE.	10
2-4	Overview of functions and strategies for wave energy conversion.	12
3-1	Overview of design requirements.	14
3-2	Overview of the fulfilment of force and moment controllability criteria for all concepts.	16
4-1	Linear wave theory bounds.	22
4-2	Overview of model verification tests.	34
6-1	Energy capture of a 2×1 array with one linear and two rotary generators. Simulated for random seas with $H_s = 2.25$ m, $T_p = 6.50$ s and waves coming at 0°	49
6-2	Overview of energy capture by a 2×1 array for random seas with 0° wave direction. Values are in percentage of the total energy in the waves of each sea state. Top: Reactive control with an efficiency of 1.0, middle: Reactive control with an efficiency of 0.7, bottom: Resistive control with an efficiency of 0.7.	51
7-1	Optimized K_p , K_d and natural frequencies for monochromatic and random waves with a 0° wave direction.	55
7-2	Overview of capture width ratios (CWRs) for all control methods and wave directions (WDs).	55
8-1	Data and computed parameters for the hydraulic part of the power take-off mechanism. Top: Specifications from manufacturers. Middle: Power and viscous damping for a 2×1 array in random seas with $H_s = 6.50$ m, $T_p = 6.50$ and 0° wave direction. Bottom: Computed parameters for the hydraulic part of the power take-off mechanism.	62
8-2	Properties and computed parameters for the spring in the power take-off mechanism at dominant sea state. Top: Material properties. Middle: Spring requirements. Bottom: Computed spring parameters.	66

8-3	Overview of array parameters.	67
B-1	Movement of pontoons that results in displacement of the generators. For generator motion, first number is a result of pontoons moving in opposite directions, second number in the same direction.	76
D-1	Overview of all found values for energy capture and control parameters for ten consecutive two hour long runs per control strategy. Simulated for a 2×1 array in random seas with $H_s = 2.25$ m, $T_p = 6.50$ s and a 0° wave direction.	80
D-2	Overview of energy capture in two hours by a 2×1 array for random seas with 0° wave direction. Values are in GJ. Top: Reactive control with an efficiency of 1.0, middle: Reactive control with an efficiency of 0.7, bottom: Resistive control with an efficiency of 0.7.	81
D-3	Overview of optimized spring constants of a 2×1 array with an efficiency of 1.0 for random seas at a 0° wave direction. Values are in $\text{N/m} \times 10^5$	82
D-4	Overview of optimized damping constants of a 2×1 array with an efficiency of 1.0 for random seas at a 0° wave direction. Values are $\text{Ns/m} \times 10^4$	82

Preface

The idea for this thesis was born 8 years ago. I was in high school and a partner and I needed to have a subject for our project. We thought about it and the design of a device that could produce electricity from ocean waves seemed like a fun project. The result of this project was a buoy tied to a dynamo and a fly wheel on the ocean floor. We tested a scale model in the towing tank of the faculty of 3mE at the Delft University of Technology. The result was a tiny flicker from a led that was powered by the device. That tiny flicker sparked an interest that has been living with me ever since. I was thrilled when I got the chance to again set foot at the subject of wave energy for my thesis, but now with the knowledge of one bachelor's and two master's degrees.

This report is the result of many hours of dedication and I hope you will find it as interesting as I do.

Acknowledgements

There are many people I would like to thank. Some have been directly involved in the writing of this thesis and others have simply supported me.

First of all, I would like to thank ir. T.W.A. Blad. Thijs was there for many sessions where he gave me advice and was directly involved in the writing of this thesis.

Secondly, I would like to thank my supervisors prof. dr. ir. J.W. van Wingerden and dr.ir. N. Tolou for their constructive criticism.

Last and certainly not least, I would like to thank my friends and family for their support. Thank you for sharing in the highs and the lows.

Delft, University of Technology
November 5, 2019

Luc Hogervorst

“Every once in a while, a new technology, an old problem, and a big idea turn into an innovation.”

— *Dean Kamen*

Chapter 1

Introduction

This chapter introduces the reader to wave energy harvesting. First, the reason is explained why electricity should come from renewable sources. Then, the devices that harvest wave energy, wave energy converters, are introduced and some examples are given. After that, the goals of this thesis are presented and the layout of this report is discussed.

1-1 Global warming

The average temperature on earth has risen with about 0.2°C per decade in the last 30 years [1]. This year, on the 25th of July 2019, the Netherlands measured its highest temperature ever in recorded history with a stunning 40.7°C [2]. The increase in temperature already has visible impacts on our environment, causing the melting of glaciers [1] and the arctic ice, which is shrinking with about 3% every decade [3]. The scientific community agrees that humans are responsible for global warming by the emission of green house gases (such as CO_2) [4]. The CO_2 percentage in our atmosphere has been steadily rising since the industrial revolution [5].

Aside from most perils that come with global warming, the low lands in the Netherlands are especially in danger as sea levels rise. However, the Netherlands was the second worst country in Europe when it comes to renewable energy sources in 2017, with only 6.6% of total energy generated from renewable sources [6]. The goal set in European agreements is 14% renewable energy by 2020, so change is necessary.

A solution to reduce CO_2 emissions is generating electricity from renewable sources such as solar and wind. The problem with these is that they are variable and cannot be controlled (one cannot increase the amount of wind or sun when more electricity is needed). Therefore, it is practical to have a mixed source of renewables, so that the variability evens out and less energy storage is needed. Energy from waves at sea can bring more diversity, but is not nearly used as much as solar and wind [7].

1-2 Wave energy converters

A machine that absorbs energy from ocean waves is called a wave energy converter (WEC). WECs come in many shapes and sizes. One example is depicted in Figure 1-1. It consists of two rows of arms with floats at the end that are attached to a steel structure [8]. When waves hit the floats, the arms pivot around their attachment points and pump hydraulic fluid to a hydraulic motor. This hydraulic motor is attached to an electric generator and energy is produced in this manner. The Wavestar is producing electricity in Denmark and the amount can be followed live [9].

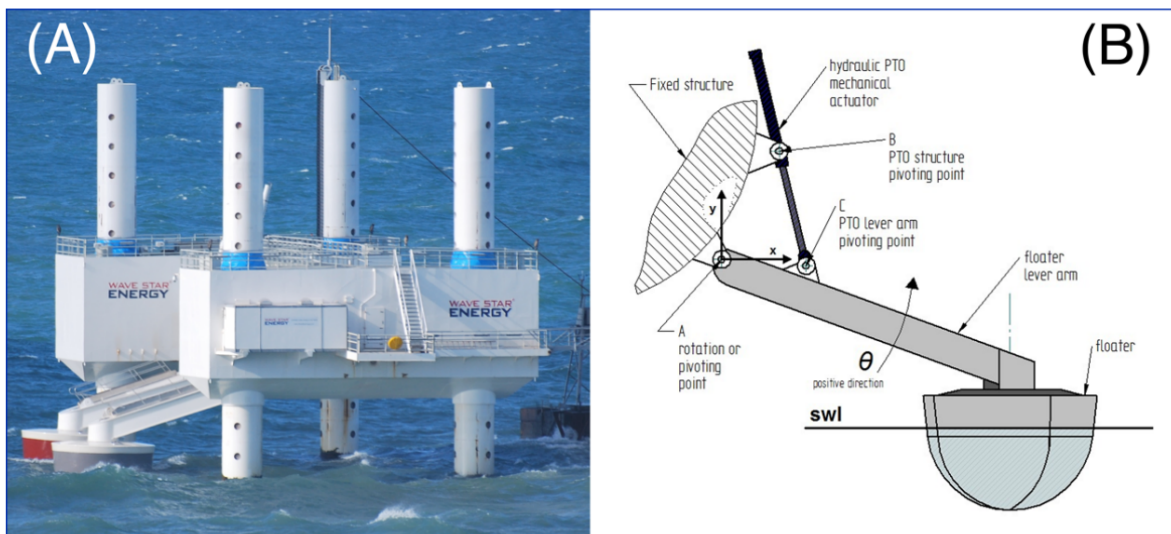


Figure 1-1: (A) Photo of the Wavestar wave energy converter. (B) Working principle of the arms of the Wavestar. From Ferri et al. [10].

Another example of a WEC but with a different principle of operation is the LIMPET [11]. It was built in 2000 on the island of Islay in Scotland. It consists of a large chamber built onto the shore that is open on the bottom and in contact with the sea, see Figure 1-2. When waves come onto and off the shore, it causes the water level in the chamber to rise and fall as well. This results in an oscillating airflow that comes in and out at a hole in the top of the chamber, in which an air turbine is built. The turbine drives an electric generator to generate electricity. This type of WEC is called an oscillating water column. So far, no consensus has been reached on the best WEC design [7]. Therefore, more research is necessary into these machines.

To generate significant power, WECs will probably be installed in groups called arrays or farms that share a power cable to shore. It was found that there was no review done for WEC devices in arrays and the control developed for them. Therefore, a literature study was done prior to this work [13]. The conclusion was that there is a type of WEC array that has promise, but is not investigated yet.

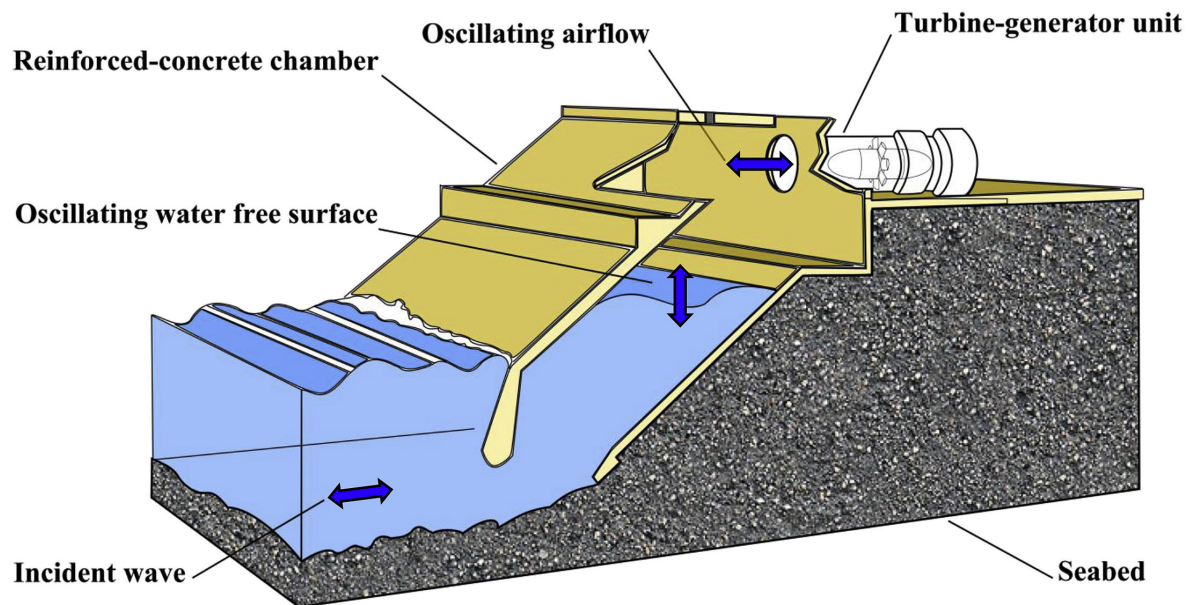


Figure 1-2: Schematic drawing of an oscillating water column type wave energy converter, from Hashem et al. [12].

1-3 Goals of this study

The first goal of this study is to make a system design of a WEC array from the category that was found lacking research. This type of array has the advantages that its energy harvesting principle does not require it to be attached to the ocean floor, it is space efficient and can in theory generate more energy with the same damping than most typically used WECs [13]. The exact design problem is given in Section 2-3, but can be summarized as the design of the kinematics and size of a mechanism that is comprised of many linked elements that are excited by the waves. The goal from the start is to design an array, instead of the usual approach where single devices are designed and are then later optimized in the array. An added bonus to the design is that solar panels can be placed on top of the array, but the focus is on harvesting wave energy.

The second goal of this study is to implement, compare and evaluate scalable Resistive and Reactive control on the new type of WEC array designed in this work. All control methods found in the literature study [13] are applied to bottom-fixed WECs that move vertically, so it is interesting to investigate how this new type of array reacts to control. Reactive control was chosen because it can improve on Resistive control with the least amount of disadvantages of all forms of control researched in the literature study. Resistive control is used as a benchmark.

1-4 Layout of this report

Chapter 2 analyses how WECs capture energy and defines the design problem and boundary conditions. It was found that there are two functions that must be fulfilled in order to capture wave energy.

The third chapter covers the system design for the design problem defined in Chapter 2. Systematically, choices are made starting with the general kinematics up to the sizing of the array components.

Chapter 4 explains the mathematical modelling. It starts with wave theory and how WEC arrays are modelled. It continues with some simplification to speed up the computation. After that, the model is verified using prior art and four other tests.

The fifth chapter covers the control methods in detail. A method to combat the curse of dimensionality is proposed using distributed optimization.

Chapter 6 shows the results for energy capture and confirms some of the design decisions made in Chapter 3. It ends with the computation benefit of distributed optimization.

The seventh chapter discusses the results found in its previous chapter. This is done by analysing the eigenfrequencies of the array, by comparing the energy capture to other WECs and by discussing how much the energy capture can be improved with more advanced control.

Chapter 8 shows that it is possible to make a physical representation of the system design. Its energy capture is computed and it turns out that it is the equivalent of 234 households from wave energy alone.

The ninth and final chapter concludes this report and gives recommendations for future work.

Mechanical Analysis

2-1 Introduction

Wave energy converters (WECs) are essentially dampers of waves. A wave comes at a WEC, the WEC interacts with it and the extraction of energy leaves the wave smaller than it was before. There are many possible ways of designing a WEC. Figure 2-1 shows two examples of vastly different WECs from literature. The DEXA in Figure 2-1a harvests energy by the movement of its two floating sections around a hinge and converts this energy to electricity by a hydraulic power take-off (PTO) mechanism [14]. The Wave Dragon in Figure 2-1b has a ramp where waves flow over and this difference in water height is used to power a water turbine [15, 16].

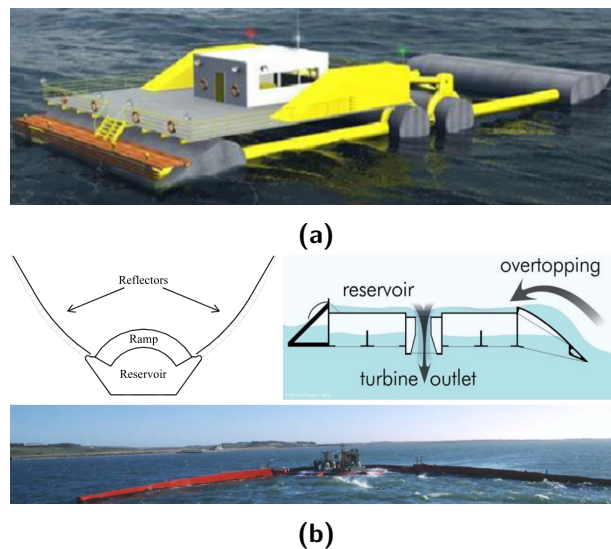


Figure 2-1: Examples of wave energy converters from literature; (a) the DEXA [14], (b) the Wave Dragon [15, 16].

This chapter presents a mechanical analysis of WECs based on how energy flows from the waves through the device up to the point where it is converted into electricity. The points where the energy is manipulated are identified as the functions of the device. The solutions that fulfil these functions are presented as strategies. A choice is made between these strategies and this is used in the system design described in Chapter 3.

2-2 Mechanical Analysis

There are two functions that every WEC must have in order to be able to convert power in the waves to usable electricity. First, it must be able to absorb potential and kinetic energy from the waves into a medium of the device and secondly, it must be able to convert this captured energy to electricity through a generator of some kind. It is possible that this generator requires a minimal velocity to function that cannot be gained by wave excitation only. In that case, an extra step is necessary in between the energy absorption and electric conversion step: velocity increase. Figure 2-2 shows the power flow from waves, through the WEC, to eventually power in the form of electrical current. Arrows represent power and blocks represent a manipulation of that power and are the functions of the WEC.

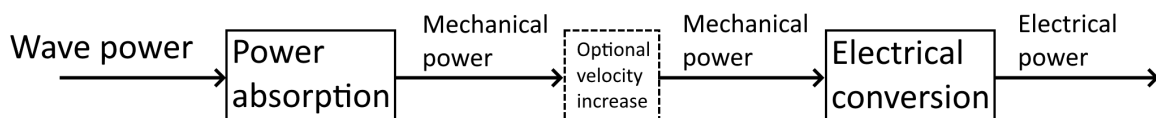


Figure 2-2: Energy flow through a wave energy converter.

The next subsections present the solution space for these three functions.

Power absorption

Power absorption is the most defining function for a WEC, as this is the first step in the energy harvesting process. The solution space can be encompassed by the medium to which the absorbed energy is transferred, the medium which is in contact with the waves. This can be a gas, liquid or a solid. Theoretically, the medium can also be a plasma, but since this state does not naturally occur on earth's surface (except when a lightning bolt strikes), it is left out. Table 2-1 shows the three states of matter that can be used to capture energy from the waves, together with the types of mechanical energy that are possible for these states.

Table 2-1: States of matter and forms of mechanical energy.

	Gas	Liquid	Solid
Kinetic	Particle velocity	Particle velocity	Velocity of body
Potential	Compressed gas	Gravitational	Gravitational
			Elastic

An example of a solid that is used to absorb wave energy is shown in Figure 2-1a. The floating bodies (solids) are moved by the waves, thus absorbing wave energy to kinetic energy of a

solid. An example of a liquid that is used to absorb wave energy is shown in Figure 2-1b. Waves are led up the ramp where they fall into a storage container, where the water (liquid) has gravitational energy and is converted to kinetic energy as it is led through a water turbine.

The amount of power (P) in waves per meter crest (which is the width w of the wave) can be computed using the following relationship [17]:

$$\frac{P_{\text{wave}}}{w_{\text{wave}}} = \frac{\rho_w g^2 H^2 T}{32\pi} \quad (2-1)$$

Where ρ_w is the density of water, g is the gravitational acceleration of earth, H is the wave height and T is the wave period.

Optional velocity increase

A velocity increase is necessary if the velocity is too low for the generator to function efficiently. The solution space again can be encompassed by the medium which is used to increase the velocity: A gas, liquid or solid. For a velocity increase to happen, the form of energy must be kinetic, but can be caused by potential energy such as compressed gas, gravitational and elastic energy. Velocity increase for a gas or liquid can be achieved by decreasing the diameter of the pipe through which the liquid or gas flows. For a solid, a velocity increase can be achieved by mechanisms such as levers, gears and pulleys.

The medium that absorbs the power from the waves is not necessarily the medium which is used for velocity increase. An example of this is shown in Figure 2-1a, where the medium of absorption is a solid, but the velocity increase is realized by a liquid: pressurized hydraulic fluid. The size of such a hydraulic cylinder can be easily calculated. If the maximum necessary force is 1 MN (which is a realistic value for a WEC [18]) and the maximum pressure in the hydraulic cylinder is 300 bar [19], then the diameter can be computed from the relationship between force and pressure:

$$F = pA_p \quad (2-2)$$

$$= p\pi r^2 \quad (2-3)$$

Where A_p is the surface area of the hydraulic piston, r is the radius of the cylinder, p is the internal pressure and F is the force exerted by the piston.

From this relationship, a force of 1 MN can be generated if the piston has a diameter of 0.21 m and a pressure of 300 bar. In the case of a piston, the velocity increase is linear, but a rotational velocity increase is possible as well by using a rotating pump or gears for example.

Electrical conversion

Electricity can be generated from motion by triboelectric [20], piezoelectric [21] and electromagnetic induction [22] principles. Here, only electromagnetic generation is explained because it is most commonly used for utility scale electricity generation and for WECs as well [23–27].

For the working principles of the other two methods is referred to their respective sources. Electromagnetic generation functions by inducing a changing magnetic field, usually with magnets, that produces an electrical current in surrounding coils [22]. Graves et al. [28] use Faraday's law of induction to derive the reactive force of a simple generator made up of a magnet in a coil (fig. 2-3):

$$F_{gen} = \frac{2\pi^2}{d_m^2} \frac{(NA_m B_0)^2}{(R_{int} + R_{ext})} v_m \quad (2-4)$$

Where d_m is the distance between two magnets with the same orientation, N is the number of coil windings, A_m is the cross-sectional area of the magnets, B_0 is the magnetic flux density amplitude (determined by the magnets), R is the resistance, which can be internal (resistance in the wires) or external and v_m is the velocity of the magnets.

It is assumed that the magnetic field is uniform and its amplitude varies sinusoidally as the magnets move through the coil.

One can see from Equation (2-4) that the generator force is proportional to the velocity, which makes it a pure damper. The damping constant can be influenced by changing the external resistance, without changing anything about the device itself.

Generators can produce electricity from linear motion as well as rotation. An example of a direct drive linear generator for a WEC has been made by Polinder et al. [18] and is capable of producing a resistant force of 1 MN. An example of a direct drive rotary generator for WECs was not found. In most WECs, a rotary generator is used in conjunction with velocity increase [23].

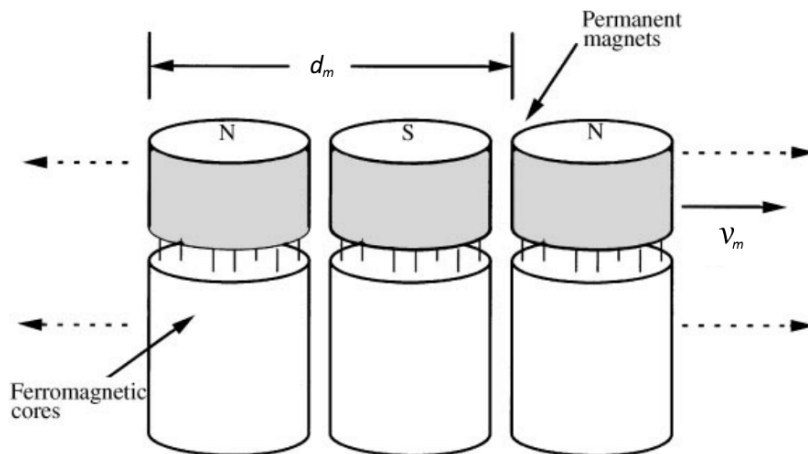


Figure 2-3: Schematic drawing of magnets moving inside a coil (ferromagnetic cores). Only part of the coil is drawn. Adapted from Graves et al. [28].

2-3 Design problem formulation

As mentioned in Chapter 1, the starting point of the system design comes from the literature study [13]. There, a classification is made based upon the boundary conditions that an energy harvester can have and the number of inputs. There are three boundaries possible: fixed to

the ground, forced motion (i.e. an external force is applied) and free motion, where a mass can oscillate freely. This gives rise to the three possible types that can harvest energy in Figure 2-4. The input is defined as the place where energy is added to the system, which is the Forced boundary condition. It was found that the category of WEC arrays named 'Forced-Forced n input' is an interesting research direction, where n means many inputs. The advantages of this type of array are that they do not need to be attached to the ground for energy harvesting, they are space-efficient and can in theory harvest more energy with the same damping constant as the most used type of array. The fact that they are not attached to the ground means that they should be floating. This means that it should be possible to place solar panels on top.

The design problem is formulated as follows: "Efficiently harvest energy from ocean waves through a Forced-Forced, n input array." Having many inputs is too vague, so n is defined as the possibility to extend the array, such that the number of inputs in the array can go to infinity in theory. The part about integration of solar panels is left out of the design problem intentionally, because this is not the focus of this research. It will however be added as a design requirement, which will be discussed in Section 3-1.

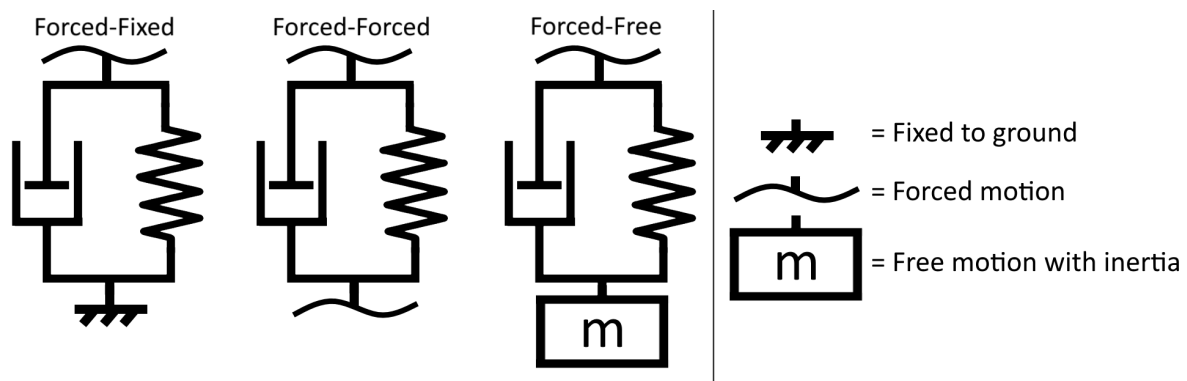


Figure 2-4: Three types of one-dimensional energy harvesters. Power take-off mechanism is displayed as a spring and damper. Adapted from Hogervorst [13].

The design problem has two boundary conditions which need to be taken into account. Firstly, waves induce large forces with low frequency. Wave climate varies from place to place, so a location has to be chosen to have specific data about the wave climate that can be used later in simulation. This is chosen to be a place 35 km off the east coast of England (52.528°N , 2.304°NE) where wave data is available. Table 2-2 shows the occurrence of sea states at that location measured in significant wave height (H_s) and wave peak period (T_p) and Figure 2-5 shows its wave directions [29]. H_s is equal to the mean of one third of the highest waves and T_p is the period in the wave spectrum with maximum energy [29]. These two parameters together can be used to compute the wave spectrum and this is shown in Chapter 4. The average power for such a spectrum can be computed with a formula similar to Equation (2-1) [30] and will be explained in Chapter 4. This average power can be multiplied with the occurrence of the sea states to compute the total power for each sea state and this is done in Table 2-3. One can see that for the sea state with the most power, $H_s = 2.25$ m and $T_p = 6.50$ s. The design will be optimized for this sea state.

The second boundary condition is on the minimal velocity needs and maximum torque or force that the electrical conversion system can deliver. This is not relevant for the system

design (as will become clear in Section 2-4), but it is for the proof of concept, where realistic values should be used for forces that actual generators can deliver.

Table 2-2: Occurrence of sea states in percentage for a location 35 km off the coast of England (52.528°N, 2.304°NE). Wave peak period T_p (s) is on the horizontal axis and significant wave height H_s (m) on the vertical. Adapted from Geos [29].

H_s (m)	3.5-6	0	0	0	0	0	0.5	0.4	0.1
	3.0-3.5	0	0	0	0	0.2	1.2	0.2	0
	2.5-3.0	0	0	0	0	2.1	1.4	0.1	0
	2.0-2.5	0	0	0	0.4	5.6	0.8	0	0
	1.5-2.0	0	0	0.1	6.7	4.8	0.4	0	0
	1.0-1.5	0	0.1	6.9	13.7	3.6	0.4	0	0
	0.5-1.0	0	7.1	16.7	8.8	5.5	0.1	0	0
	0-0.5	0.4	6.0	2.9	2.3	0.4	0	0	0
			2-3	3-4	4-5	5-6	6-7	7-8	8-9
		T_p (s)							

Table 2-3: Power per sea state in percentage of total power for location 52.528°N, 2.304°NE.

H_s (m)	3.5-6.0	0.0	0.0	0.0	0.0	0.0	6.5	6.2	2.3	0.4
	3.0-3.5	0.0	0.0	0.0	0.0	0.8	7.7	1.6	0.0	0.0
	2.5-3.0	0.0	0.0	0.0	0.0	8.0	6.4	0.4	0.0	0.0
	2.0-2.5	0.0	0.0	0.0	0.8	14.4	2.5	0.1	0.0	0.0
	1.5-2.0	0.0	0.0	0.1	8.8	7.4	0.7	0.0	0.0	0.0
	1.0-1.5	0.0	0.0	3.8	9.2	2.8	0.3	0.0	0.0	0.0
	0.5-1.0	0.0	1.1	3.3	2.1	1.6	0.0	0.0	0.0	0.0
	0-0.5	0.0	0.1	0.1	0.1	0.0	0.0	0.0	0.0	0.0
			2-3	3-4	4-5	5-6	6-7	7-8	8-9	9-10
		T_p (s)								

2-4 Strategy selection

In order to get started with the system design, a choice in strategy has to be made for the functions discussed in Section 2-2. An overview of the functions and their strategies is given in Table 2-4.

Firstly, a choice has to be made concerning the power absorption function. The principles vary too much for this to be left to abstraction. The choice is between using a solid, liquid or a gas as the medium in which wave energy is absorbed. It is the most interesting to choose the solid medium for the design problem in this thesis, because a Forced-Forced n input array requires multiple objects that move with respect to each other. If these moving objects are solids, then it makes sense to extract energy from their relative velocities, but this is not the case for fluids and gases and the following example shows why:

A n input gas or liquid WEC array would have several chambers floating in the water that capture water or air by their movements caused by the waves or waves flowing in a reservoir.

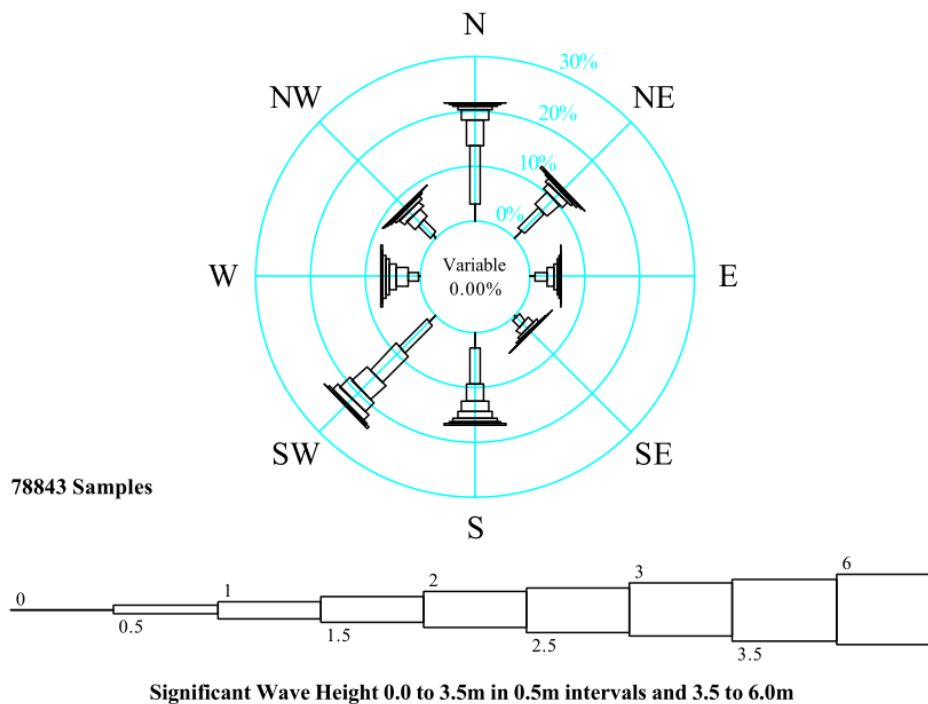


Figure 2-5: Wave directions for location 52.528°N, 2.304°NE, from Geos [29].

They move separately from each other and liquid or gas flows between them. Electricity is generated from the flow between them.

It is not useful however to have these chambers interconnected since there already is a place where this liquid or gas can go to (the sea or the atmosphere). There is only a possibility of generating equal or less energy than if they were connected to the sea or atmosphere. Particles always go always go from a high to a low pressure and if two chambers coincidentally both have an equally high pressure, then no flow occurs and no energy is generated, while they both could produce energy if they were connected to the sea/air. However, for solid objects there is a definite benefit to linking them because without links, no energy can be generated.

Secondly, for the function velocity increase, a choice in particular technology such as using gears or pistons does not have to be made yet. This is because the system design only considers the kinematics of the overall mechanism. The two kinematic forms that are possible for velocity increase are linear or rotational and a choice will be made regarding this in the next chapter. The actual embodiment of these kinematics will be covered in Chapter 8.

Lastly, the electrical conversion strategy choice is to use electromagnetic induction since this is a proven technology for macro systems, while the other two are not (as was mentioned in Section 2-2). The design of a new generator is out of the scope of this research, so conventional linear or rotary generators will be used in this regard. The choice between linear and/or rotary generators is one that has to be made in the system design.

Table 2-4: Overview of functions and strategies for wave energy conversion.

Function	Strategy
Power absorption	Liquid absorption medium
	Gaseous absorption medium
	Solid absorption medium
Optional velocity increase	Liquid medium
	Gaseous medium
	Solid medium
Electrical conversion	Triboelectric
	Piezoelectric
	Electromagnetic induction

Chapter 3

System Design

This chapter describes the design of the wave energy converter (WEC) array at an abstract level. This means that the kinematics of the array are designed, but how this is physically possible is not considered in this chapter. It must however be possible to make a physical design that resembles these kinematics and for this reason, a not necessarily optimal physical design is proposed in Chapter 8.

The following section describes the design requirements and the starting point of the system design and each of the sections after that explain the system design choices.

3-1 Analysis and design requirements

A choice in strategy was made in Chapter 2 concerning the power absorption medium and the electrical conversion strategy. The solid absorption medium and electromagnetic induction were chosen respectively for these functions. This results in a starting point for the system design: a number of floating bodies (pontoons) and the option to connect these with linear or rotary generators or velocity increase mechanisms, as depicted in Figure 3-1. Only two pontoons are drawn, but the array can be extended to an arbitrary number of pontoons by copying the mechanism used on two pontoons. The bodies must be floating, if they are not, then it would be a Forced-Fixed array instead of a Forced-Forced array. The generators and velocity increase mechanisms have the same kinematics, they can be either linear or rotary ‘hinges’, so it is not important for the system design to make a distinction between them. Only the term generator will be used throughout this chapter for the sake of compactness.

Before the system design can be started, the requirements on the system should be clear. The most important requirement on this system is that it does not break. Waves can introduce great forces on a structure, especially when there are multiple parts that are moving with respect to each other. This is the reason for the first design requirement: Forces on connections should be controllable. Controllable means that the forces and torques on the connections can be made as low as one wants, by setting the parameters (damping and stiffness) of the generators.

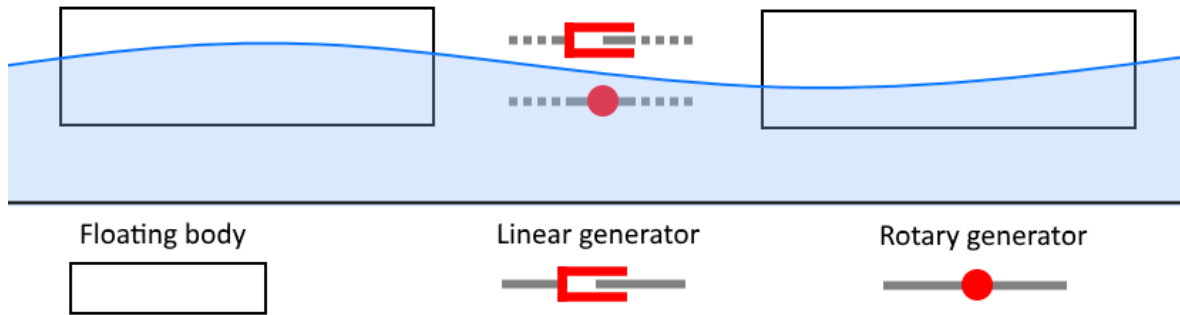


Figure 3-1: Starting point of the system design. Top: side view of two floating bodies with the possibility to connect them with linear or rotary generators. The generators are dashed because it is not decided yet how they are connected to the pontoons. Bottom: legend.

The second requirement is related to energy harvesting efficiency. To get the most energy out of two bodies that move relative to each other, all relative degrees of freedom should be harvested if there is motion in these degrees of freedom. For 2D bodies in water, this is the case for all three degrees of freedom. So the requirement will be: All degrees of freedom should be used in energy harvesting. If it later turns out that some degrees of freedom in fact do not generate as much energy as others, then these generators can be replaced by ordinary hinges.

The third requirement is on the space for solar panels. There should be space available for solar panels on top of the pontoons. The connections have moving parts so it is not convenient to put solar panels on those.

Lastly, the connections should prevent the pontoons from hitting each other. This is dependent on the connections but also on the amount of force exerted by the generators. It will be assessed in simulation if the pontoons indeed do not collide for all types of seas in Section 6-7 and this is indeed not the case.

An overview of all design requirements is given in Table 3-1.

There are some requirements that one might think of that are not in the list of design requirements. For example, there could be a requirement that says that the pontoons should be excited by the waves, indeed if this is not the case no energy can be produced. This is however already fulfilled if there is a pontoon so this requirement is omitted. Requirements on the electricity (phase and frequency for example) are omitted as these are important for the power equipment, but will not influence the system design. This is also the case for requirements related to strength of the material or the amount of material needed to not break under the stress induced by the waves.

Table 3-1: Overview of design requirements.

Design requirement

1. Forces on connections should be controllable.
2. It should be possible to use all degrees of freedom in energy harvesting.
3. Space should be available on top of the pontoons for solar panels.
4. The pontoons should not hit each other.

3-2 Type and number of generators

Section 2-2 showed that generators and velocity increase come in two variants: linear and rotary movements. This can be used to create conceptual solutions. A solution space can be created by the number of generators and the two variants. For now, it is assumed they are all generators, later it will be assessed how much energy each of the generators contributes to the total energy production and if some can be replaced by ordinary linear or rotational hinges. Figure 3-2 shows the conceptual solutions with three generators in the connections, where the orientation and placement of the generators are arbitrary. These concepts are drawn in two dimensions as a side view, but can be made three dimensional by using the same principle but extended into the third dimension. Concepts with one or two generators are not shown because they do not fulfil the requirement of using all degrees of freedom in energy harvesting, since each generator harvests one degree of freedom. The concepts can be named after the generators from left to right, using L for a linear generator and R for a rotational generator (for example, the concept in the bottom left is named LLR). There are two generator types and three generators, so that makes $2^3 = 8$ possible combinations. However, there are two mirrored concept couples: LLR and RLL, and RRL and LRR. The mirrored versions are left out as they have the same properties as their counterpart.

The concepts are evaluated on their survivability requirement: Forces on connections should be controllable. This is only possible if the pontoons are able to move relative to each other in all degrees of freedom. If this is not the case, then the forces and moments on the connections and the bodies are determined by the waves. This criterion coincides with the requirement on efficient energy harvesting: All degrees of freedom should be used in energy harvesting. This is used next to make a choice in the six concepts of Figure 3-2.

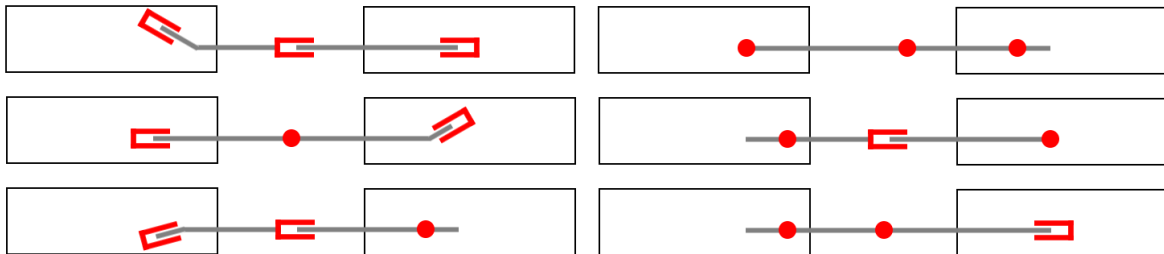


Figure 3-2: Conceptual solutions with 3 generators.

The LLL concept can be excluded on first sight, because the pontoons cannot move in rotation relative to each other. Concepts LRL and LLR can move in all DoF relative to each other. However, in practice a non controllable moment can occur if the left pontoon rotates and the right pontoon keeps its orientation. This happens because the rotation of the linear generator on the left pontoon forces it to extend and this results in unwanted friction forces which will cause problems in practice. An example of this is given in Figure 3-3 for a simplified case. Concepts RRR and RRL have states in which they cannot move relative to each other in all directions and where forces and moments are thus not controllable. This happens for both of these concepts when the beams are straight as in the figure, then the pontoons cannot move relative to each other in the vertical direction while keeping the same orientation. This makes them not impossible candidates since the mechanism can be designed to avoid this

state, but it makes them less suitable. The most suitable concept is RLR, but only if the linear generator is positioned along the line between the two rotational generators (as it is in the figure). It harvests energy from all degrees of freedom and all forces and moment on the connections are totally controllable.

An overview of the criteria considered for the decision in concepts in this section is given in Table 3-2.

Concepts that have more than 3 generators were not considered because a concept with 3 generators has been found that fulfils all requirements and more generators will not improve this.

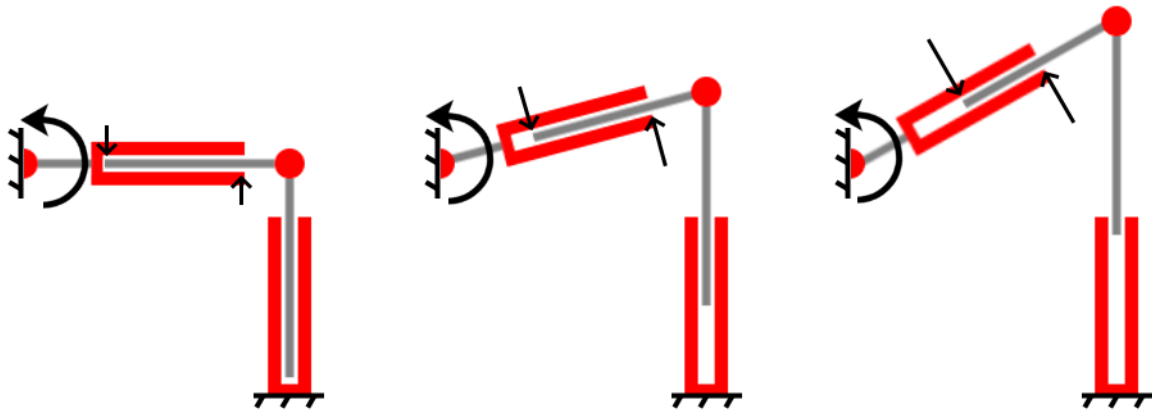


Figure 3-3: Torque on a mechanism with two linear and one rotary generator. Applied torque is indicated with anticlockwise arrows and resultant forces perpendicular on the linear generators with straight arrows.

Table 3-2: Overview of the fulfilment of force and moment controllability criteria for all concepts.

Criterion	RLR	RRR	RRL	LLR	LRL	LLL
Forces and moments are controllable in theory	✓	✓	✓	✓	✓	×
Forces and moments are controllable in practice	✓	✓	✓	×	×	×
Forces and moments are controllable in all states	✓	×	×	×	×	×

3-3 Generator placement

Now that a concept has been chosen for the type, ordering and number of generators, the place of these generators needs to be chosen. To keep the bending moment on the connection beam as small as possible it is beneficial to make it as short as possible. In that case the rotary generator will be placed on the far end of each pontoon as depicted in Figure 3-4. They are placed at half the height so that the rotary generators have enough space to be built around that place.

The placement of the generators will not affect the amount of energy harvested, since energy is harvested from all degrees of freedom and the damping coefficients are optimized. The optimum damping coefficients will however change depending on where the generators are

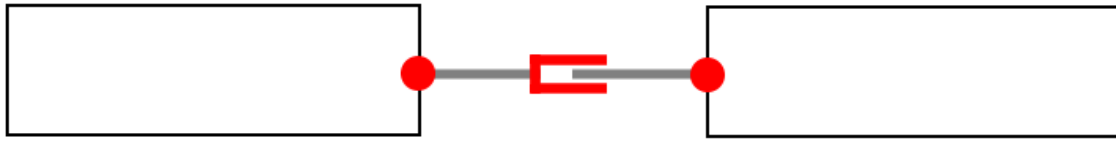


Figure 3-4: Generator placement for minimum length of connection beam.

placed. Appendix A proves the two previous statements for a simplified energy harvester and Appendix B shows that the motion of the generators change when they are placed in the middle of the pontoons and that greater damping coefficients are to be expected for optimality in that case.

3-4 Top view pontoon shape and number of connections

Now that a choice has been made on the placement for the connections, the next step is to determine the number of connections and the pontoon shape. This is the design of the top view of the array. From an engineering perspective, the least number of connections per pontoon would be preferred, as adding more connections while the requirements have already been met seems pointless. The least amount of connections is three per pontoon, as the array will span in two dimensions in the horizontal plane. The space for solar panels should be maximized, while keeping a gap between the pontoons so that they do not collide. This results in a triangular pontoon shape, as shown in Figure 3-5a. This maximization of space can be done with a pen and a sheet of paper. One starts with a top view of round pontoons with three connections per pontoon and draws the array. Then space for solar panels is maximized while keeping a gap between the pontoons by drawing straight lines perpendicular to the connections at the places where connections are attached to the pontoons. This results in triangular pontoons with equal spacing between the pontoons at all points.

There is however a problem when the triangular array is simulated. The least amount of pontoons to be simulated to get a good idea of the behaviour of the whole array is six, otherwise there would be pontoons that have only one connection and will go out of control because there are forces perpendicular to the one connection. However, the computation time for six pontoons would probably be several days, as the parameters for four pontoons take half a day to compute and the computation time increases exponentially with array size (this will be shown in Chapter 4).

The solution to this problem is to look at square arrays with four connections per pontoon instead of triangular arrays. One can see in Figure 3-5b that for this array, the minimum amount of pontoons is two for wave directions that are perpendicular to the array or four pontoons otherwise. There is also the added benefit that this array is more regular. The pontoons line up behind each other with the same orientation and spacing for perpendicular wave directions, which is not the case for the triangular array. This can be used to simplify the mathematical model and makes analysis of eigenvalues easier.

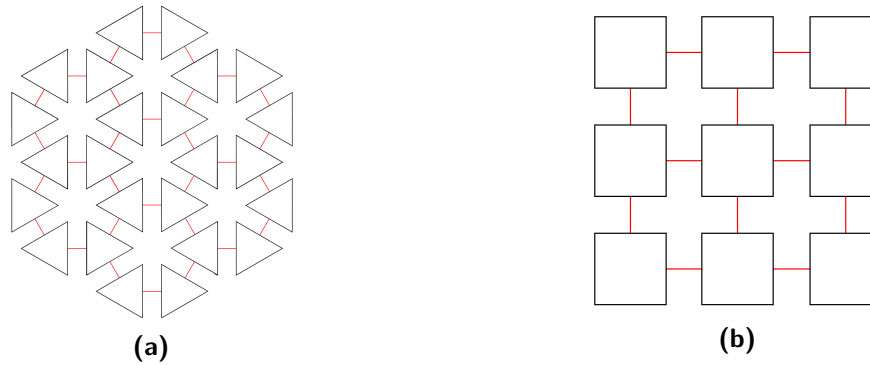


Figure 3-5: Top view of arrays; (a) triangular array, (b) square array.

3-5 Spacing and size of pontoons

For energy harvesting, it is optimal if wave forces between subsequent pontoons are 180° out of phase. This means that the size and spacing of pontoons should be adapted to the wave climate and this is dependent on the array location.

The wavelength (λ) in deep water is formulated as follows [31, 32]:

$$\lambda = \frac{gT^2}{2\pi} \quad (3-1)$$

Where g is the gravitational acceleration of earth and T is the wave period.

The peak period of the sea state that the array is designed for is 6.50 s. This results in a wavelength of 66.0 m. So the pontoons should be spaced 33.0 m apart, from centre to centre. Chapter 6 shows that this is indeed an efficient spacing. The centre to centre distance is dependent on the wave direction. Figure 3-6 shows the centre to centre distance for a 0° and 45° wave direction, where the centre to centre distance for 45° is $\cos(0.25\pi) = 0.707$ smaller than for 0° . Figure 2-5 shows that about 75% of the waves come from N-NE and S-SW directions, so it is beneficial to place the array in this direction and optimize the spacing in this direction. It is possible for other locations that the wave directions are more evenly distributed, then a compromise has to be made between the different directions.

The space between pontoons should be as small as possible, because this will minimize the bending moment on the connections and maximize space efficiency. However, the linear generator needs space and a minimum distance is needed so that the pontoons do not collide. In Chapter 6, the array is simulated and it is shown that the pontoons move with a maximum of 2 m from their starting position, this means that the generator has a stroke of 8 m and a minimum of 4 m is necessary in between pontoons to prevent them from colliding. However, the power take-off (PTO) mechanism (i.e. the linear generator) needs more space than that, as one can see in Chapter 8 for a proof of concept detailed design. There, the PTO mechanism has a maximum stroke of 10 m (8 m plus a 25% safety margin) and this mechanism needs a spacing of 10 m in between pontoons. This results in a pontoon size of 23 m.

The height of the pontoons is a question of cost versus the amount of energy generated, as a higher pontoon will absorb more wave energy but will cost more as more material is needed.

The relationship between pontoon height and energy capture is displayed in Figure 6-5 in the results chapter for pontoons that are half submerged. One can see that it resembles an asymptotic function which levels out at a pontoon height of 6 m. The variable costs of the array are not only dependent on the material for the pontoons, but also on the PTO mechanism (which will become more expensive as more energy is harvested), labour and many other cost factors. A detailed cost analysis would involve computation of these variable costs and also constant costs such as workshop location. This is out of the scope of this research. An estimation of the optimal height can be made from Figure 6-5 however. One can see that when the height increases from 1 to 2 m, the energy capture increases with a factor of 1.84, but when the height goes from 2 to 4 m it only goes up with a factor of 1.39. Therefore it might not be cost effective to make the height as great as 4 m and 2 m is chosen as a conservative estimation of the height of the pontoons.

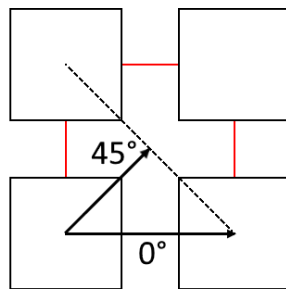


Figure 3-6: Visualisation of the difference in center to center distance between subsequent pontoons for 0° and 45° wave direction.

3-6 Final system design

The design choices in this chapter together with simulation results from Chapter 6 conclude to a final system design. Chapter 6 has two important points that have not been mentioned yet. Firstly, it shows that the rotary generators do not contribute much to the total energy production and secondly, that a $2 \times n$ array generates the most energy per pontoon. Variable n can be set to infinity in theory, but will be limited in reality by practical problems such as available space.

The final system design that thus arises is a $2 \times n$ array connected with linear generators and where the rotary generators are replaced by rotary hinges. This is depicted in Figure 3-7.

The design problem as stated in Section 2-3 was: "Efficiently harvest energy from ocean waves through a Forced-Forced, n input array." This final design is indeed optimized for efficiency, by harvesting as much wave energy while keeping costs in mind where possible, it is a Forced-Forced array and it can be extended to infinite pontoons in theory. The requirements are fulfilled because all forces on the connections are controllable, it is possible to harvest energy from all degrees of freedom (but it was found that the rotary generators do not contribute much), solar panels can be put on top of the pontoons and lastly, it was found in simulation that the pontoons do not collide.

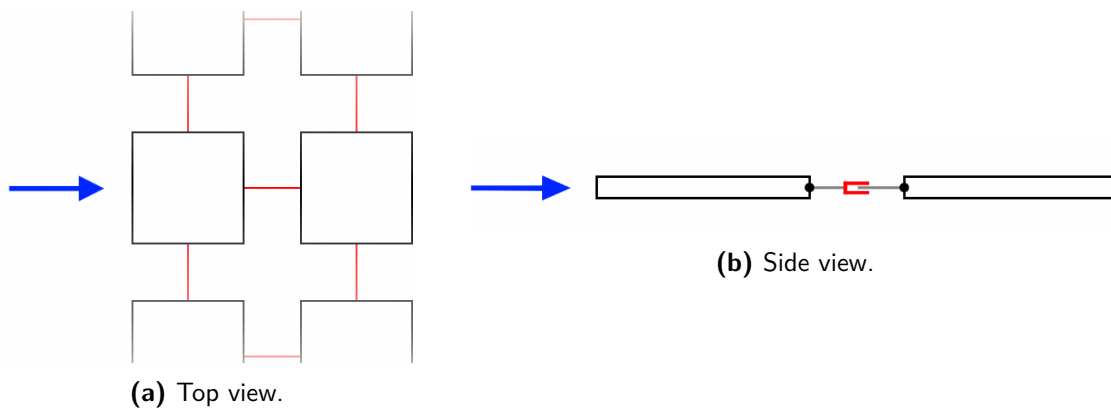


Figure 3-7: Final system design of the $2 \times n$ array connected with linear generators. Dominant wave direction is indicated with an arrow.

Modelling and simulation

This chapter explains how the mathematical model is build up that is used to simulate the wave energy converter (WEC) array. The first section introduces the necessary background information, the section after that explains the mathematical model for WECs, the next section goes into model simplification and lastly, the model is verified with five tests to see if the model is sound.

4-1 Wave theory

4-1-1 Water waves

A wave is depicted in Figure 4-1, where λ is wavelength, H is wave height, d_w is the water depth. There are different forms of wave theory for different waves and which to use is dependent on these parameters [33], see Figure 4-2. If one assumes that the water is deep, then the maximum wave height for linear theory can be calculated with just the wavelength. The wavelength can be computed as follows [34]:

$$\lambda = \frac{gT^2}{2\pi} \quad (4-1)$$

Where g is the gravitational acceleration of earth and T is the wave period.

With the wavelength known, the maximum wave height where linear wave theory can still be applied to, is computed in Table 4-1.

The significant wave height (H_s), introduced in Chapter 2, is the average height of the 33% highest waves and the peak period T_p is the period in the wavespectrum where the spectral density is greatest, see Figure 4-3. It can be seen in Table 2-3 that for most of the sea states that have a significant power contribution, even the mean of the one third highest waves lie in the linear domain, except for the sea state with $H_s = 4.75$ m and $T_p = 7.5$ m. However, that

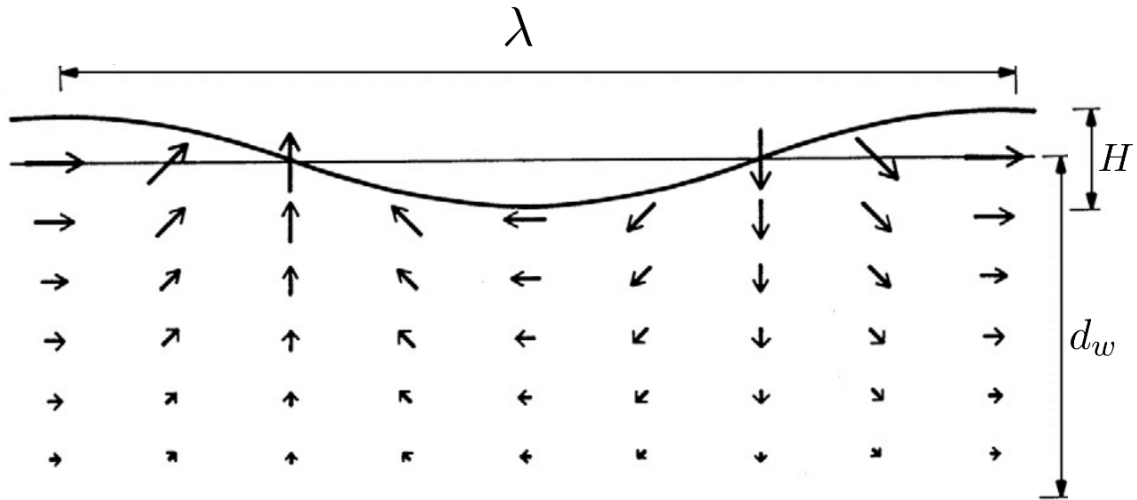


Figure 4-1: Wave parameters, adapted from Newman [32]. Arrows indicate water particle movement.

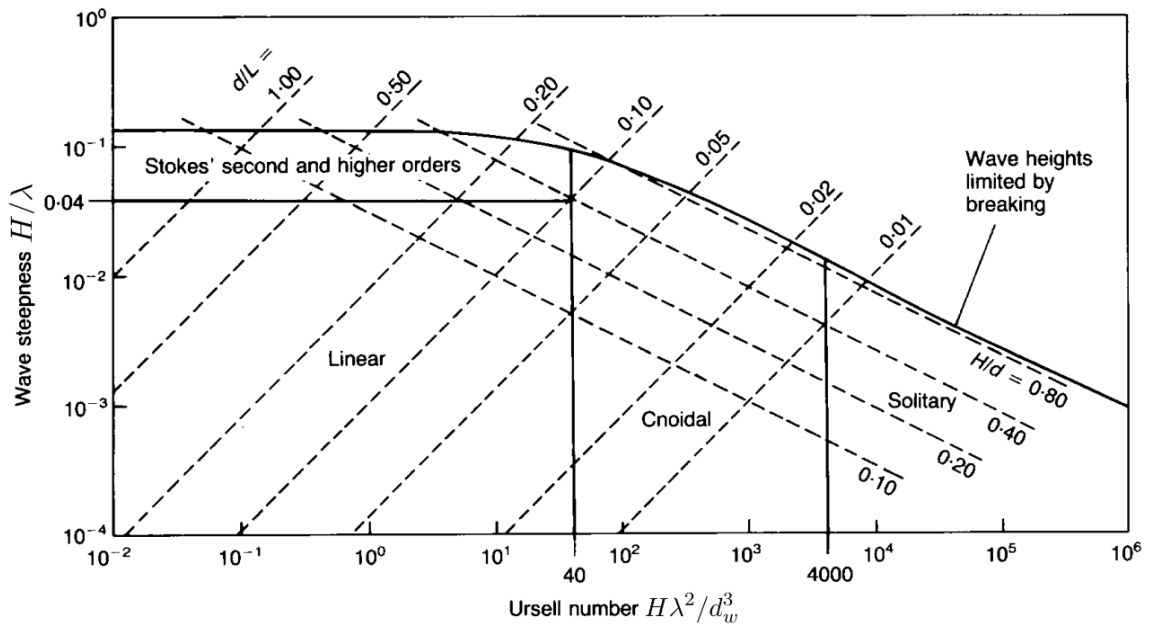


Figure 4-2: Domains of wave theory, adapted from Hedges [33].

Table 4-1: Linear wave theory bounds.

Wave period (s)	3.5	4.5	5.5	6.5	7.5	8.5	9.5
Wavelength (m)	19.1	31.6	47.2	66.0	87.8	113	141
Maximum wave height for linear theory (m)	0.765	1.26	1.89	2.64	3.51	4.51	5.64

sea state only contributes to 6.5 % of the total power so this will only have a small impact on the accuracy of total energy capture. Thus it was decided to use linear wave theory.

In linear wave theory, the water particles move in circles when a wave comes by [32], as can be seen in Figure 4-1. The forces and moments that these exert on floating bodies in the water are thus also cyclic. Using linear theory, the surface elevation of monochromatic waves can be described as follows [35]:

$$\eta(x, y, t) = A \cos\left(\frac{2\pi}{\lambda}(x \cos \beta + y \sin \beta) - \omega t\right) = \Re\left(Ae^{i\left(\frac{2\pi}{\lambda}(x \cos \beta + y \sin \beta) - \omega t\right)}\right) \quad (4-2)$$

Where among already mentioned variables, x and y are distance in the horizontal plane, β is the wave direction (angle around the z -axis) and A is the wave amplitude.

4-1-2 Waves at sea

Waves at sea are not monochromatic. However, the wave elevation can be described by a superposition of many monochromatic waves according to a spectrum and with random phase [36]. In the north sea, the wave spectrum can be computed with H_s and T_p according to the JONSWAP spectrum. The JONSWAP spectrum [37] is a variance spectrum that was fitted to data on waves in the North Sea. Spectral density of a parametrized JONSWAP spectrum [36] is described by:

$$S_\eta(f) = \alpha H_s^2 f_p^4 f^{-5} \gamma^\beta \exp\left(-\frac{5}{4} \left(\frac{f_p}{f}\right)^4\right) \quad (4-3)$$

$$\alpha \approx \frac{0.0624}{0.230 + 0.0336\gamma - \left(\frac{0.185}{1.9+\gamma}\right)} \quad (4-4)$$

$$\beta = \exp\left(-\frac{(f - f_p)^2}{2\sigma^2 f_p^2}\right) \quad (4-5)$$

$$\sigma \approx 0.07 \quad f \leq f_p \quad (4-6)$$

$$\sigma \approx 0.07 \quad f \geq f_p \quad (4-7)$$

$$(4-8)$$

Where among previously mentioned variables, f is frequency, f_p is the peak frequency (inverse of T_p) and γ is the peak enhancement coefficient, which is on average 3.3 for the North Sea [36].

The JONSWAP spectrum for $H_s = 2.25$ m and $T_p = 6.50$ s can be found in Figure 4-3.

The definition of the variance spectral density is as follows [36]:

$$S_\eta(f) = \frac{\frac{1}{2}A^2(f)}{\Delta f} \quad (4-9)$$

Where among previously mentioned variables, Δf is the bandwidth, which is the frequency range divided by the number of frequency components.

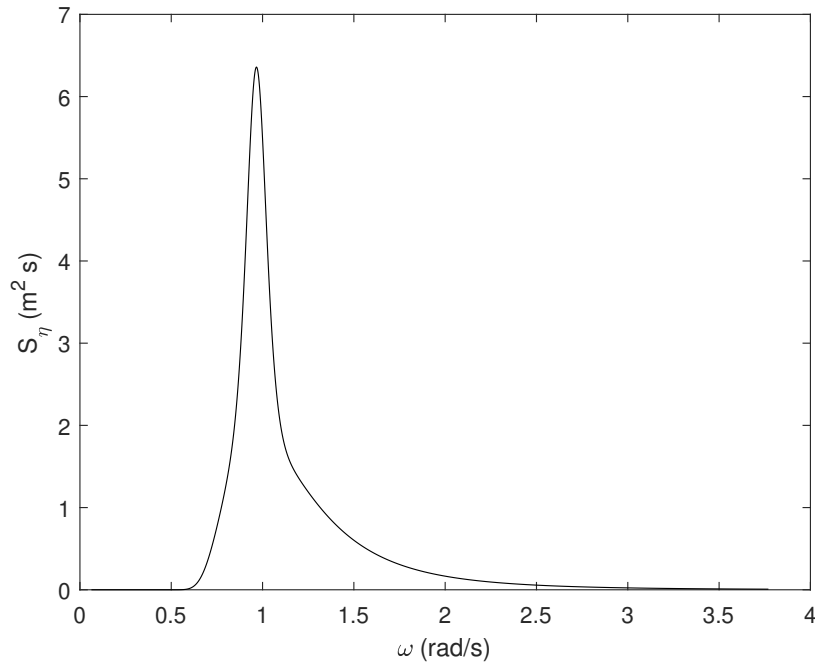


Figure 4-3: JONSWAP wave spectrum for north sea waves with $H_s = 2.25$ m and $T_p = 6.50$ s.

So to simulate waves for random seas, one chooses a number of frequency components, computes the bandwidth that belongs with it, and uses Equation (4-9) to get the wave amplitude for each frequency. The superposition of these frequencies with random phase results in ocean waves according to that spectrum [36]. If more frequency components are used, then the approximation of real waves becomes better. In this work, 1000 monochromatic waves added together make up the random seas. The wave force $\mathbf{f}_{wave}(t)$ is determined in a similar way to the wave elevation η , which will be explained in Section 4-2-3.

4-1-3 Wave power

Power in monochromatic waves was explained in Section 2-2, which can be computed from the wave height, period, density of sea water and the gravitational acceleration of earth. Average power in waves at sea is a little bit more complex because it is comprised of a spectrum, but can be computed using the following formula [30]:

$$\bar{P}_{sea} = \frac{\rho_w g^2}{4\pi} \int_0^\infty \frac{S_\eta(f)}{f} df \quad (4-10)$$

Where among previously mentioned variables, ρ_w is the density of sea water.

Using Equation (4-10), the average power per meter wave crest in the dominant sea state ($H_s = 2.25$ m and $T_p = 6.50$ m) was computed to be 14.5 kW/m.

4-2 Mathematical modelling of wave energy converters

4-2-1 Differential equations for wave energy converters

Folley et al. [38] recommend using the following time-domain model for the simulation of WECs arrays when control is used:

$$(\mathbf{M} + \mathbf{A}_M(\infty))\ddot{\mathbf{x}}(t) + \int_0^t \mathbf{k}(t - \tau)\dot{\mathbf{x}}(\tau)d\tau + \mathbf{C}\mathbf{x}(t) = \mathbf{f}_{wave}(t) + \mathbf{f}_{pto}(t) \quad (4-11)$$

Where $\mathbf{x}(t)$ is the state which holds all translations and rotations of all the WECs in the array, \mathbf{M} is the mass matrix that has all mass and inertial terms of the array, $\mathbf{A}_M(\infty)$ is the added mass at infinite frequency, $\mathbf{k}(t)$ is the radiation impulse response matrix, \mathbf{C} has the hydrostatic and gravitational restoring coefficients, $\mathbf{f}_{wave}(t)$ is the wave force and $\mathbf{f}_{pto}(t)$ is the force of the power take-off (PTO) mechanism.

This equation, due to Cummins [39], was originally meant for ship motions and assumes linearity. It is derived from the frequency domain model of a mass-spring-damper system with frequency dependent mass and damping coefficients and wave force, see Equations (4-12) and (4-13). The mass and damping are frequency dependent due to the displacement of water [32].

$$\left[-\omega^2(\mathbf{M} + \mathbf{A}_M(\omega)) + i\omega\mathbf{B}(\omega) + \mathbf{C}\right] \mathbf{X}(\omega) = \mathbf{F}_{wave}(\omega) + \mathbf{F}_{pto}(\omega) \quad (4-12)$$

$$\left[-\omega^2(\mathbf{M} + \mathbf{A}_M(\infty)) + i\omega\mathbf{K}(\omega) + \mathbf{C}\right] \mathbf{X}(\omega) = \mathbf{F}_{wave}(\omega) + \mathbf{F}_{pto}(\omega) \quad (4-13)$$

$$\text{with } \mathbf{K}(\omega) = \mathbf{B}(\omega) + i\omega(\mathbf{A}_M(\omega) - \mathbf{A}_M(\infty)) \quad (4-14)$$

Where among previously mentioned variables, ω is the wave frequency, $\mathbf{B}(\omega)$ is the added damping and $\mathbf{X}(\omega)$, $\mathbf{F}(\omega)$ and $\mathbf{K}(\omega)$ are the Fourier transform of $\mathbf{x}(t)$, $\mathbf{f}(t)$ and $\mathbf{k}(t)$.

4-2-2 Computation of hydrodynamic coefficients

The hydrodynamic coefficients in matrices $\mathbf{A}_M(\omega)$, $\mathbf{B}(\omega)$, \mathbf{C} and the wave excitation force factor can be computed by boundary element solvers such as WAMIT and NEMOH [40]. NEMOH [41] is used in this work because it is open source software. The reader is referred to Babarit and Delhommeau [41] for the theoretical and numerical background. The software needs a shape as input, which is a box, and the number of WECs. Together with the centre of gravity, translations and number of panels, this shape can become a mesh through the NEMOH software and this is used to compute all necessary functions. When more panels are used, the accuracy of the hydrodynamic coefficients becomes greater, but will also take more time to compute. Therefore, a study is done to see when the solution converges, as can be seen in Figures 4-4 to 4-6. The degree of freedom is indicated with a number: 1 for surge (horizontal translation x), 2 for sway (horizontal translation y), 3 for heave (vertical translation z), 4 for roll (rotation around x -axis), 5 for pitch (rotation around y -axis), 6 for yaw (rotation around z -axis), 7 for surge of the second pontoon and so on. For the hydrodynamic coefficients, two numbers are used because these coefficients appear in a matrix. To give examples for a 2×1

array, 11 is the upper left coefficient of the matrices $\mathbf{A}_M(\omega)$, $\mathbf{B}(\omega)$, \mathbf{C} and 1212 the coefficient in the downright corner.

A number of panels of 884 was chosen as a compromise between computation time and accuracy. The difference between 884 and 1665 is at most 3.17% with the exception of some discrepancies in the added damping in heave and pitch at frequencies higher than 3.00 rad/s. But this is not a problem since the frequency at which the pontoons will move is lower than that, see Figure 4-3. The time to compute the hydrodynamic coefficients and wave excitation force factors rise exponentially with the number of pontoons and are plotted in Figure 4-7.

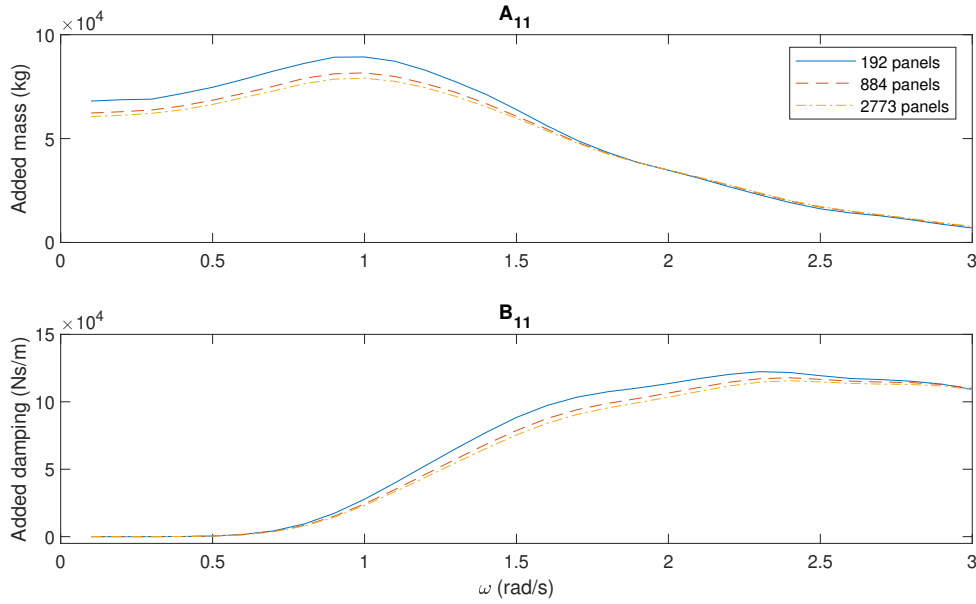


Figure 4-4: Hydrodynamic coefficients in surge for a single pontoon.

To speed up the simulation, the term $\int_0^t \mathbf{k}(t - \tau) \dot{\mathbf{x}}(\tau) d\tau$ is often replaced by a state-space approximation [42]. In this work, the Matlab tool developed by Perez and Fossen [43] was used to compute this approximation. It needs $\mathbf{A}_M(\omega)$ and $\mathbf{B}(\omega)$ as input and uses least-squares fitting to optimize the approximation. The tool showed that the state-space model is a good approximation and this was double checked by computing its impulse response and comparing it to $\mathbf{k}(t)$, which is given by NEMOH.

4-2-3 Computation of wave forces

NEMOH does not compute the wave force directly, it computes the wave excitation force factor, which is a complex number. The actual wave force is computed by multiplying the magnitude of this wave excitation force factor (see Figure 4-10) with the amplitudes of the waves (which is half of the wave height) that are present in the wave spectrum and shifting them with the phase of the wave excitation force factor. All these are then added together to get the random waves, just like it was done for the wave elevation in Section 4-1. Equation (4-15) shows how the wave force for a single frequency component [35] can be computed.

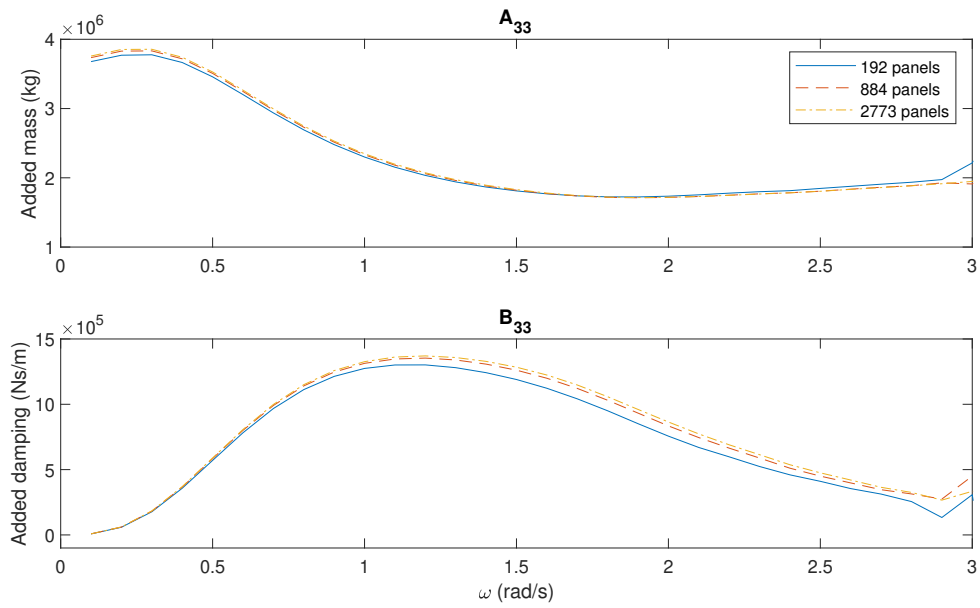


Figure 4-5: Hydrodynamic coefficients in heave for a single pontoon.

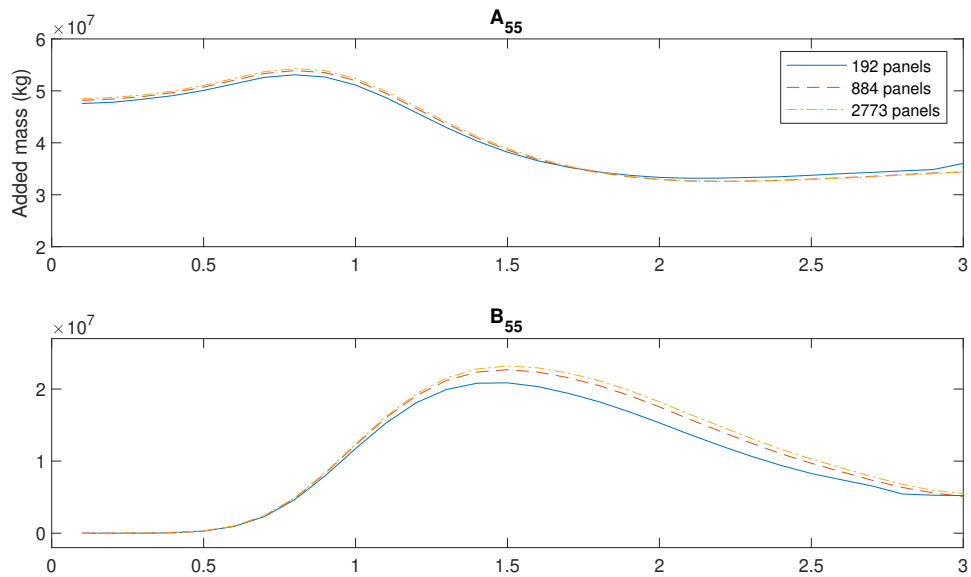


Figure 4-6: Hydrodynamic coefficients in pitch for a single pontoon.

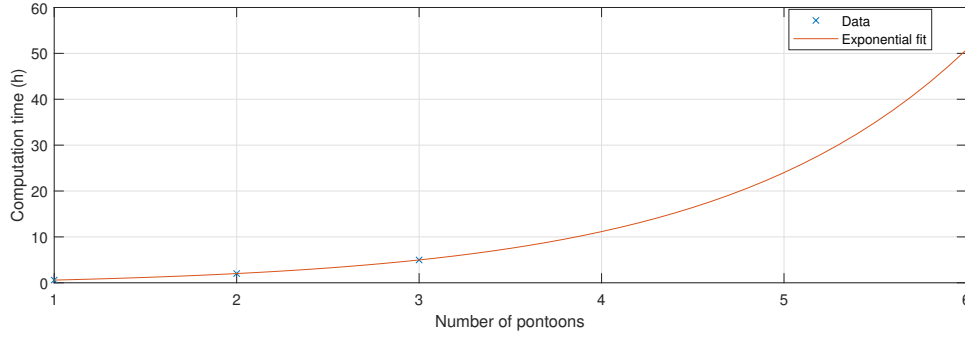


Figure 4-7: Computation time of hydrodynamic coefficients and wave excitation force factors in NEMOH versus the number of pontoons with 884 panels.

$$f_{wave}(t) = \Re \left(A \tilde{F}_e(\omega) e^{-i\omega t} \right) = \Re \left(A \left| \tilde{F}_e(\omega) \right| e^{-i(\omega t - \angle \tilde{F}_e(\omega))} \right) \quad (4-15)$$

Where among previously mentioned variables, \tilde{F}_e is the wave excitation force factor.

4-2-4 Computation of power take-off forces

There are three PTO mechanisms (or generators) that can exert forces and moments on the pontoons as can be seen Figure 4-8: Two rotary and one linear generator. The centre-mass forces and moments can be computed from the trigonometric relations. The left pontoon is

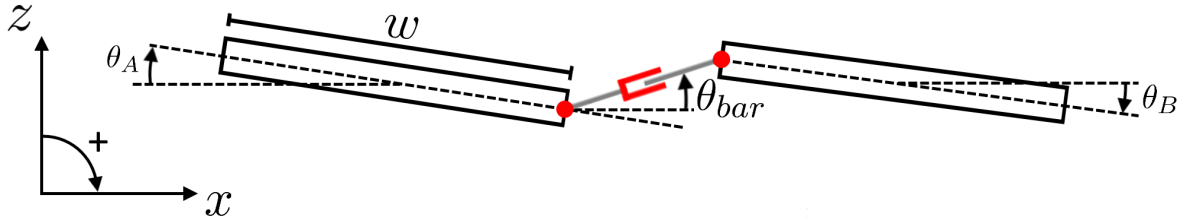


Figure 4-8: Schematic of two pontoons with definitions of angles and pontoon width.

called pontoon A and the right pontoon B and both have width w . The distance in horizontal direction is x and vertical is z , the rotation is θ . The explanation here is done for two pontoons. For larger arrays, the process is repeated for each pair of pontoons in the array in x and y -direction.

First, the horizontal width (w_{bar}), vertical height (h_{bar}), length (L_{bar}) and angle θ_{bar} of the connection bar have to be computed:

$$w_{bar} = x_B - (0.5w(\cos(\theta_A) + \cos(\theta_B)) + x_A) \quad (4-16)$$

$$h_{bar} = z_A - (0.5w(\sin(\theta_A) + \sin(\theta_B)) + z_B) \quad (4-17)$$

$$L_{bar} = \sqrt{w_{bar}^2 + h_{bar}^2} \quad (4-18)$$

$$\theta_{bar} = \arctan\left(\frac{h_{bar}}{w_{bar}}\right) \quad (4-19)$$

The PTO force (and moments) vector (with respect to the centre of mass of the pontoons), \mathbf{f}_{pto} can then be computed from previously mentioned variables, using trigonometric rules, the force of the linear generator (f_{lgen}) and the torques of the rotary generators (M_{gen}). The force vector of each generator is displayed separately for clarity in Equations (4-20) to (4-23).

$$\mathbf{f}_{genA} = \begin{bmatrix} f_{genA1} \\ f_{genA2} \\ f_{genA3} \\ f_{genA4} \\ f_{genA5} \\ f_{genA6} \\ f_{genA7} \\ f_{genA8} \\ f_{genA9} \\ f_{genA10} \\ f_{genA11} \\ f_{genA12} \end{bmatrix} = \begin{bmatrix} -(M_{genA}) \frac{\sin(\theta_{bar})}{L_{bar}} \\ 0 \\ -(M_{genA}) \frac{\cos(\theta_{bar})}{L_{bar}} \\ 0 \\ M_{genA} + \frac{(M_{genA})}{L_{bar}} (\frac{1}{2}w(\sin(\theta_A) \sin(\theta_{bar}) + \cos(\theta_A) \cos(\theta_{bar}))) \\ 0 \\ (M_{genA}) \frac{\sin(\theta_{bar})}{L_{bar}} \\ 0 \\ (M_{genA}) \frac{\cos(\theta_{bar})}{L_{bar}} \\ 0 \\ \frac{(M_{genA})}{L_{bar}} (\frac{1}{2}w(\sin(\theta_B) \sin(\theta_{bar}) + \cos(\theta_B) \cos(\theta_{bar}))) \\ 0 \end{bmatrix} \quad (4-20)$$

$$\mathbf{f}_{genB} = \begin{bmatrix} -(M_{genB}) \frac{\sin(\theta_{bar})}{L_{bar}} \\ 0 \\ -(M_{genB}) \frac{\cos(\theta_{bar})}{L_{bar}} \\ 0 \\ \frac{(M_{genB})}{L_{bar}} (\frac{1}{2}w(\sin(\theta_A) \sin(\theta_{bar}) + \cos(\theta_A) \cos(\theta_{bar}))) \\ 0 \\ (M_{genB}) \frac{\sin(\theta_{bar})}{L_{bar}} \\ 0 \\ (M_{genB}) \frac{\cos(\theta_{bar})}{L_{bar}} \\ 0 \\ M_{genB} + \frac{(M_{genB})}{L_{bar}} (\frac{1}{2}w(\sin(\theta_B) \sin(\theta_{bar}) + \cos(\theta_B) \cos(\theta_{bar}))) \\ 0 \end{bmatrix} \quad (4-21)$$

$$\mathbf{f}_{lgen} = \begin{bmatrix} -f_{lgen} \cos(\theta_{bar}) \\ 0 \\ f_{lgen} \sin(\theta_{bar}) \\ 0 \\ \frac{1}{2}w f_{lgen} (\sin(\theta_A) \cos(\theta_{bar}) - \cos(\theta_A) \sin(\theta_{bar})) \\ 0 \\ f_{lgen} \cos(\theta_{bar}) \\ 0 \\ -f_{lgen} \sin(\theta_{bar}) \\ 0 \\ \frac{1}{2}w f_{lgen} (\sin(\theta_B) \cos(\theta_{bar}) - \cos(\theta_B) \sin(\theta_{bar})) \\ 0 \end{bmatrix} \quad (4-22)$$

$$\mathbf{f}_{pto} = \mathbf{f}_{genA} + \mathbf{f}_{genB} + \mathbf{f}_{lgen} \quad (4-23)$$

4-2-5 Computation of electric power

The power absorbed or used by the PTO mechanism is computed by the definition of power: velocity multiplied with force. When the direction of the velocity of the PTO mechanism is the reverse of the direction of the PTO force, then power is absorbed. If they are both aligned, then the mechanism uses power (from the grid) to perform mechanical work. Efficiency is introduced to compute how much power absorbed by the PTO mechanism actually can be turned into electricity. Absorbed power is multiplied with the efficiency and used power is divided by the efficiency. Therefore less electric power is generated than absorbed and more electric power is needed than comes out as mechanical work performed by the PTO mechanism. The results in Chapter 6 are computed for efficiencies of 0.7 and 1.0, as the former is a representative number for the efficiency of a PTO mechanism of a WEC [42] and the latter gives valuable insight into the best case scenario.

4-2-6 Simulation

All parts of the model that have been explained previously come together in a Simulink model, see Figure 4-9. It starts by summing all forces (PTO forces, wave forces, hydrostatic forces and radiation forces) and multiplying them with the inverse of the mass matrix to compute the acceleration of the pontoons. This is then integrated to get the velocity and integrated again to get the position of the pontoons. Velocity and position are used to compute all forces and the mechanical power and the cycle starts again. The mechanical power is multiplied or divided with the efficiency, in case it is absorbed or used respectively, and integrated to get the absorbed energy minus the used energy. This netto electric energy is used in the optimization of the array.

4-3 Model simplification

When the wave direction is 0° , 90° , 180° or 270° , the pontoons are directly behind each other in a straight line. When one looks at the magnitude of the wave excitation force factor of pontoons in a straight line, such as in Figure 4-10, one can see a trend. The wave excitation force factor from the first pontoon to the last pontoon goes down with a factor of about 0.7 for each pontoon. This trend can be used to create models of arrays from the parameters of just one pontoon, since all other parameters except for the interaction terms are the same for each pontoon. When one neglects the interaction terms of the added mass and damping, it means that the pontoons do not interact with each other through waves (but still interact with each other through the forces on the connections). This also means that pontoons that are next to each other will thus move in phase and will not generate any energy. The energy production of a $n \times n$ array at a 0° wave direction can thus be computed simply by multiplying the energy production of a $n \times 1$ array by n .

The simplification is far from perfect. The wave excitation force factor of the second and third pontoon in surge and pitch show a large discrepancy for the frequency range between 1.5 rad/s and 2 rad/s in Figure 4-10 for example. The most important frequency is however 1 rad/s, as can be seen from Figure 4-3 and the simplification is quite good at that point. The phase of the wave excitation factor of all pontoons can be derived from the first pontoon

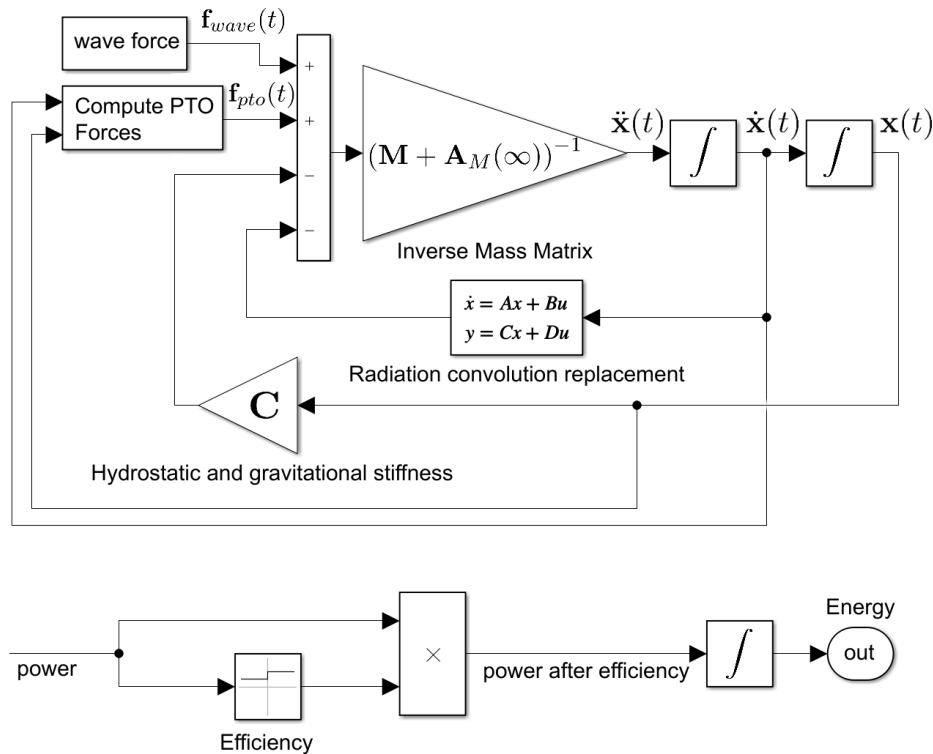


Figure 4-9: Block diagram for the simulation of the wave energy converter array in this work.

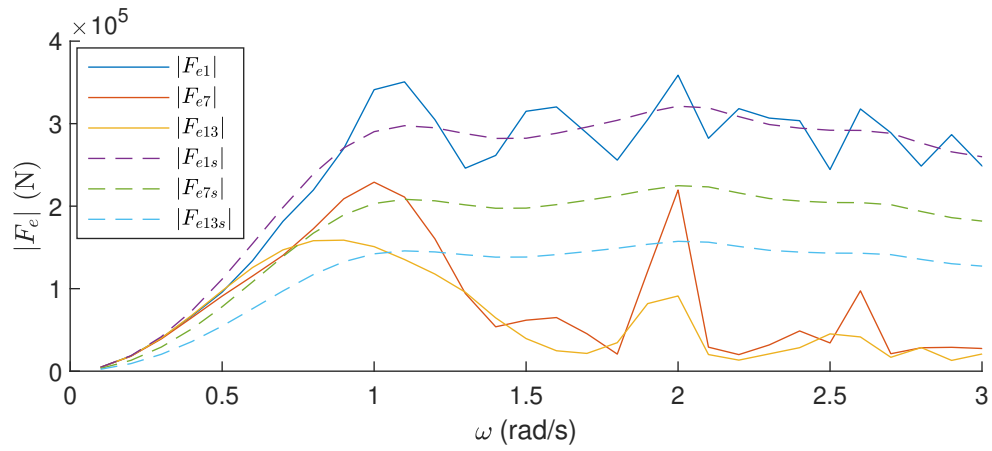
as well. This can be done by looking at the centre to centre distance of the pontoons and dividing this by the wave length (see Equation (4-1)). This fraction multiplied with 2π is the phase that has to be added to the phase of the first pontoon. This is done in Figure 4-11 and one can see that is a good approximation, especially at the frequency where it is most important.

To see how the simplification stacks up against the original model, both were optimized for energy capture with Reactive control that will be explained in Chapter 5. The simplified model extracts 12% less energy, the stiffness terms were within 2% and the damping terms within 30%. It was deemed acceptable that the model gives a conservative view of the extracted energy. The deviation for the damping terms is unfortunate, but was also deemed acceptable since these are not used in the analysis of the behaviour of the array.

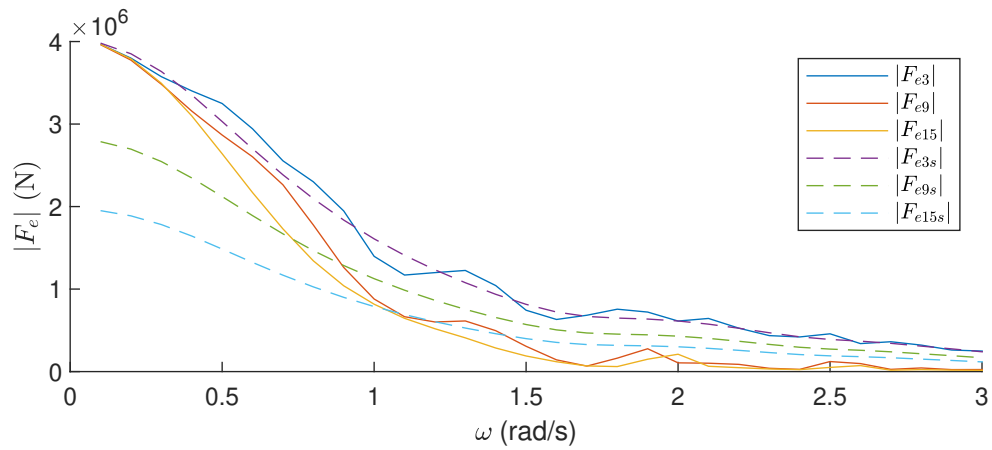
4-4 Model verification

In order to verify the model, five tests are done on different parts of Equation (4-11). An overview of the tests and what they verify can be found in Table 4-2. The tests are:

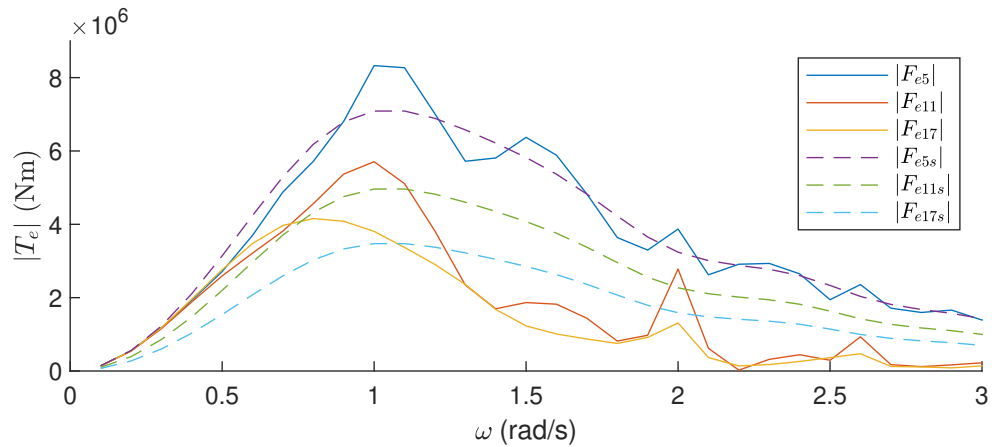
Comparison with literature The first test compares the most important hydrodynamic coefficients and wave force excitation factor amplitudes that NEMOH computes with literature. Killi [44] uses WADAM [45] to compute parameters of pontoons that are



(a)



(b)



(c)

Figure 4-10: Comparison of magnitude of simplified wave excitation force factors (dashed) with computed wave excitation force factors (solid) for a 3×1 array. Wave excitation force factor in surge (a), in heave (b) and wave excitation moment factor in pitch (c).

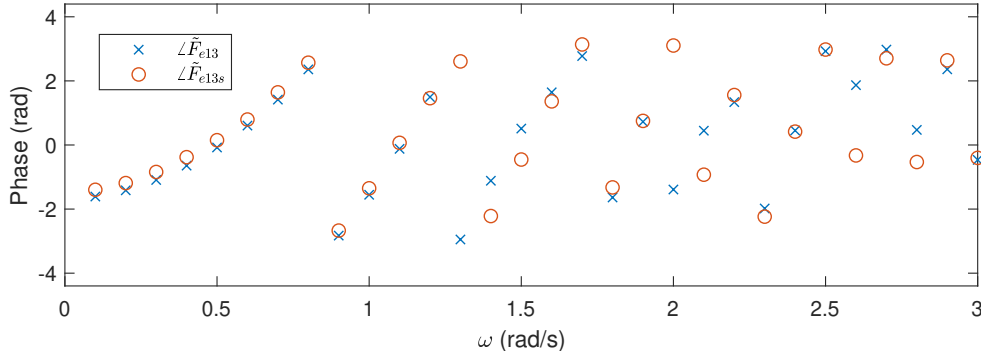


Figure 4-11: Comparison of phase of simplified wave excitation force factor (circle) with computed wave excitation force factor (cross) for the third pontoon.

58 m long, 10 m wide and have a draft (vertical length of pontoon that is underwater) of 5 m. pontoons of the same size were modelled in NEMOH, with straight corners instead of rounded, and the comparison can be found in Figures 4-12 to 4-14.

Abul-Azm and Gesraha [46] theoretically examine the hydrodynamic coefficients and forces on a square, infinitely long pontoon and confirm the results found by Andersen and Wuzhou [47]. In NEMOH, it is not possible to model infinite sizes, but a long pontoon gives the same results, as can be seen in Figure 4-15.

Archimedes' principle The second test uses Archimedes' principle to determine the accuracy of the mass matrix and the hydrostatic and gravitational restoring coefficients. The mass of the pontoons can be computed by how much water they displace and the density of seawater of 1025 kg/m^3 . The pontoons lie 1.00 m deep, so the mass of one pontoon is $5.42 \times 10^5 \text{ kg}$. NEMOH computes the same but with a 0.195 % difference. The moment of inertia in roll (I_x) and pitch (I_y) can be computed with the following formula for the moment of inertia of a solid cuboid [48]:

$$I_x = I_y = \frac{m}{12}(w^2 + h^2) \quad (4-24)$$

Where m is the mass of the cuboid, w is its width and h is its height.

When this is applied to the pontoons, the result is the same as NEMOH computes it with again a 0.195 % deviation.

The hydrostatic and gravitational restoring coefficient in vertical direction can be computed by the force that is generated when the pontoon is pushed 1.00 m into the water. This can again be computed from the water displacement and this can be compared to what NEMOH finds. The difference is negligible with NEMOH's computation. The angular restoring coefficient is a little harder to compute since they are non-linear normally, but are linearised for the use in Equation (4-11). The computation of these is done in Appendix C and the difference with the coefficient computed by NEMOH is only 1.28 %.

Energy balance The energy balance test determines if the forces exerted by the PTO mechanism are correct. The test starts by giving the pontoons an initial position and an initial speed, which gives the initial kinetic and potential energy. Then the simulation is run

without wave forces and the radiation component and an efficiency of 1.0. This means that no energy is added to the system and no energy losses are present, except for the energy captured by the PTO mechanism. The result of energy capture is compared with the initial energy and should be the same if the simulation ended with the system at rest. This was indeed the case with very high accuracy, which increased as the step size of the model was set smaller.

Infinite stiffness The infinite stiffness test is to see if two pontoons coupled with an infinitely stiff beam behave the same as a single big pontoon of the same dimensions as the two pontoons combined. Their movements will differ somewhat, because the large pontoon has mass in the place where the connection is for the two normal pontoons, but this will be small for the rotation because this mass lies close to the centre of rotation. The results for the pitch angle in random waves are shown in Figure 4-16. One can see that the results are very similar, but have slight variations.

Visual inspection of simulation The movement of the pontoons together with the waves can be plotted in a video, to see if the pontoons follow the waves. Figure 4-17 displays a snippet of this video. The interaction of the pontoons with the waves looks natural.

Table 4-2: Overview of model verification tests.

Subject	Symbol	Test
Added mass	\mathbf{A}_M	Comparison with literature
Added damping	\mathbf{B}	Comparison with literature
Wave excitation force factor	\mathbf{f}_{wave}	Comparison with literature
Mass	\mathbf{M}	Archimedes' principle
Hydrostatic and gravitational restoring coefficients	\mathbf{C}	Archimedes' principle
Force of power take-off mechanism	\mathbf{f}_{pto}	Energy balance
NEMOH consistency single pontoon and arrays		Infinite stiffness
Equation (4-11) as a whole		Visual inspection of simulation

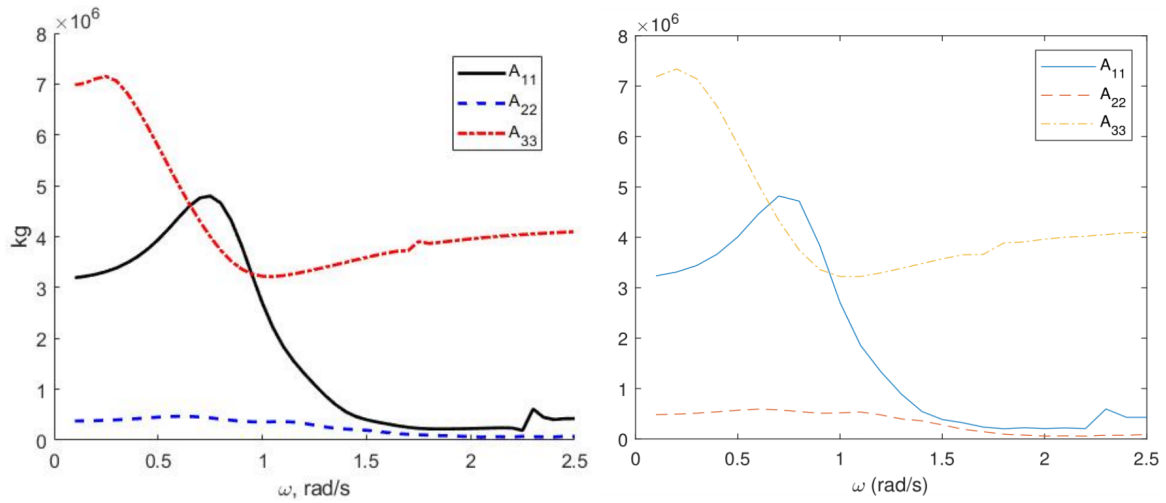


Figure 4-12: Added mass in x (11), y (22) and z (33) direction, computed by Killi [44] (left) and in this work (right) for a rectangular pontoon.

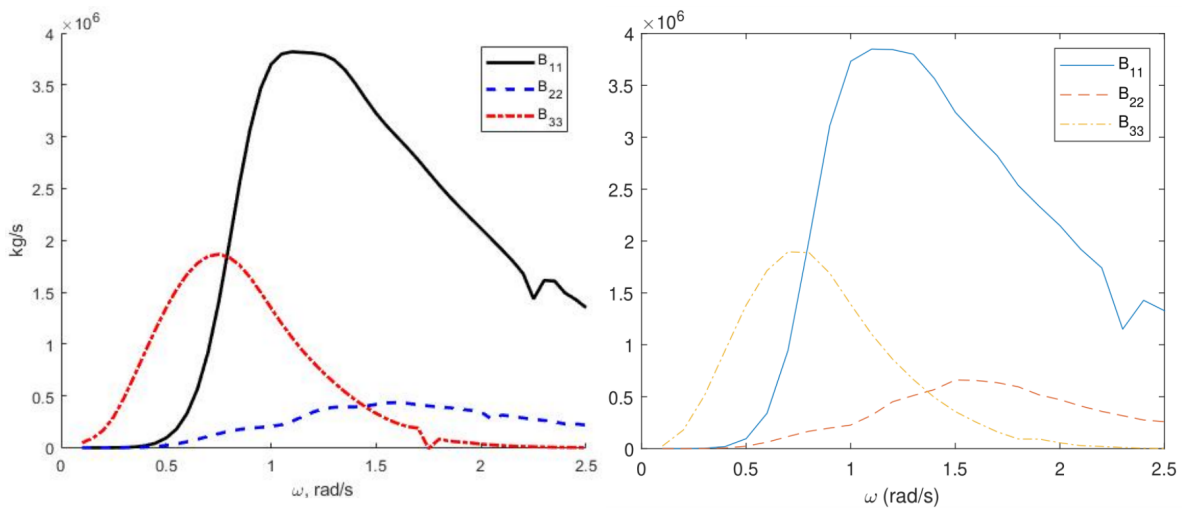


Figure 4-13: Added damping in x (11), y (22) and z (33) direction, computed by Killi [44] (left) and in this work (right) for a rectangular pontoon.

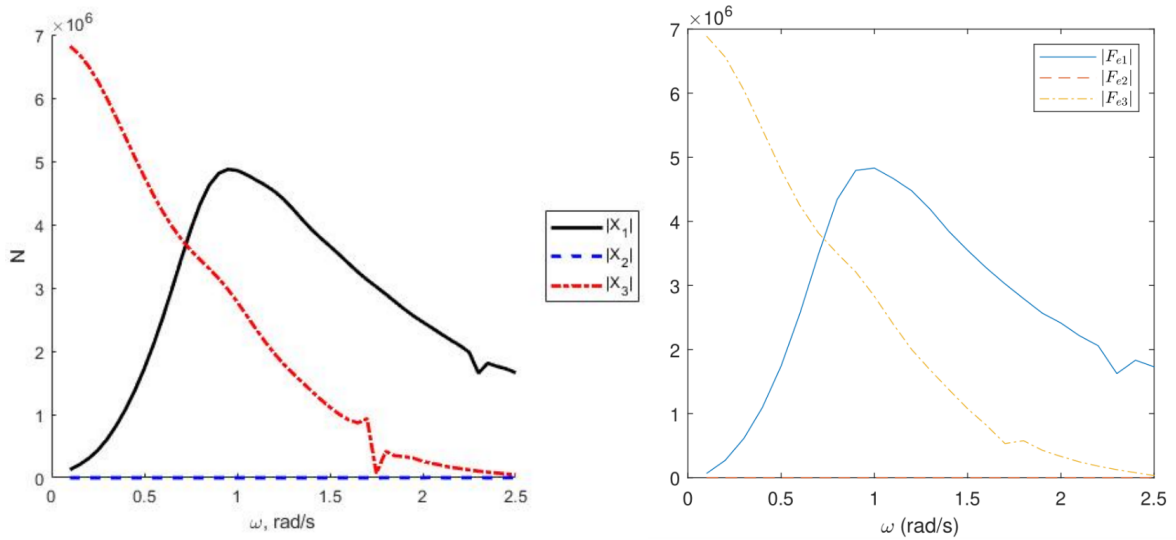


Figure 4-14: Wave excitation force factors in x (11), y (22) and z (33) direction, computed by Killi [44] (left) and in this work (right) for a rectangular pontoon.

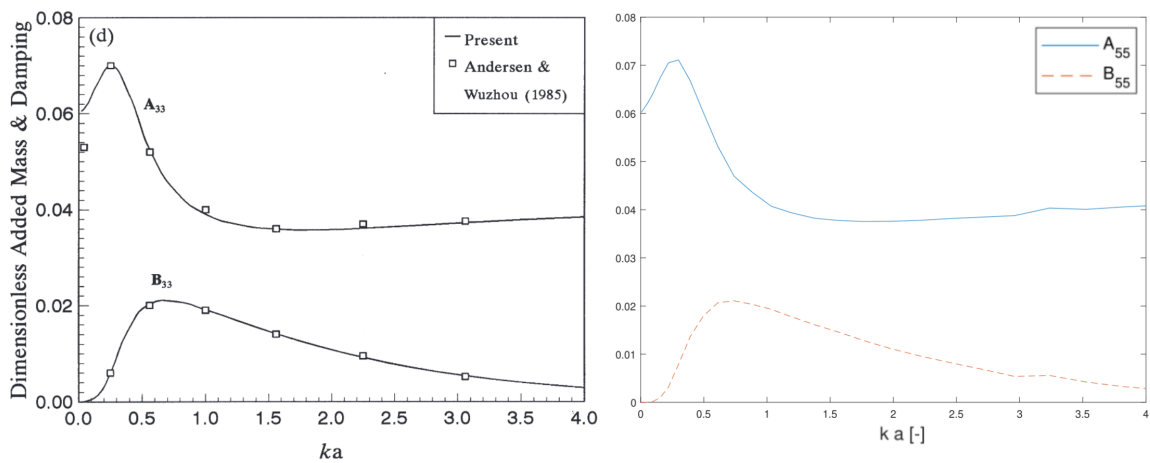


Figure 4-15: Hydro-dynamic coefficients in pitch computed by Abul-Azm and Gesraha [46] (left) and in this work (right) for a long square pontoon. On the horizontal axis is the wave number multiplied with half of the pontoon width.

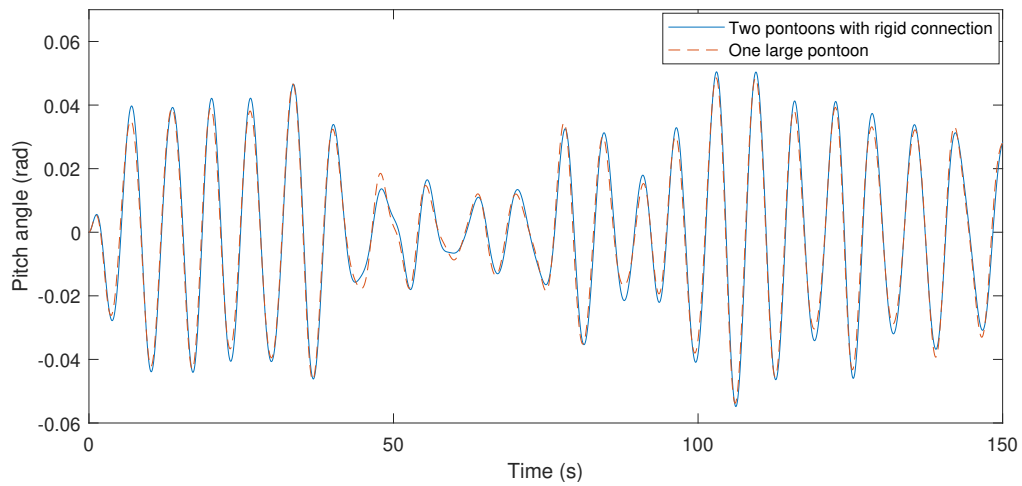


Figure 4-16: Pitch angle for a 2×1 array, where the pontoons are connected with an 'infinitely stiff' connection and pitch angle for a large pontoon that has the same dimensions as the two pontoons summed. Simulated for random waves with $H_s = 2.25$ m, $T_p = 6.50$ s and a 0° wave direction.



Figure 4-17: Video snippet from the visualization of a 2×1 array under random seas with a 0° wave direction.

Chapter 5

Control

This chapter explains the control that is applied to the wave energy converter (WEC) array: Reactive control. This type of control was chosen in the literature study [13] because it improves over the most simple form of control (Resistive control) in performance with the least amount of disadvantages.

The next section defines the control problem, the section after that explains the control algorithm, the third section proposes a distributed control strategy, which is a way to decrease computation time for large dimensionalities and the last section determines the stability of the system.

5-1 The control problem

The control problem is to maximize the amount of energy harvested by the generator, which is part of the power take-off (PTO) mechanism. This captured energy is negative from the point of view of the array (because energy is taken from the system and converted into electricity), so it is actually a minimization problem. This minimization is done for all generators over a period of time:

$$\min E(t_0, t_1) = \min \int_{t_0}^{t_1} P(t) dt \quad (5-1)$$

$$= \min \int_{t_0}^{t_1} \sum_{i=1}^q f_{pto}^i(t) z_{pto}^i(t) dt \quad (5-2)$$

Where E is energy, P is power, f_{pto} is force of the PTO mechanism, z_{pto} is displacement of the PTO mechanism, q is the number of generators and t is time. The force of the whole PTO mechanism is taken into account because although only the generator captures energy, losses in other parts of the mechanism will degrade the captured energy.

5-2 Resistive and Reactive control

Resistive [49] and Reactive control [42] are D and PD control [50] respectively, with an overarching algorithm. PD control is often applied to make a system go to a certain state and to influence criteria such as overshoot and settling time using control parameters K_p and K_d . For energy harvesting however, K_p and K_d are used to influence the natural frequency of the array and the amount of energy harvested, respectively.

Resistive and Reactive control are thus both feedback control with a control law that is formulated in Equation (5-3), where $K_p = 0$ for Resistive control. The block diagram that belongs together with this law can be found in Figure 5-1.

$$f_{pto}(t) = -K_p z_{pto}(t) - K_d \dot{z}_{pto}(t) \quad (5-3)$$

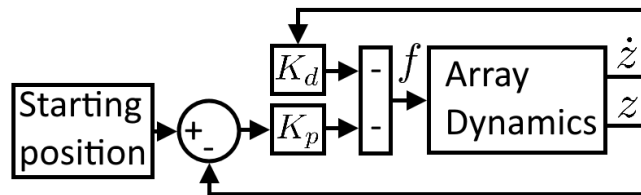


Figure 5-1: Block diagram for low level Resistive and Reactive control. $K_p = 0$ for Resistive control.

K_p and K_d are optimized in Nambiar et al. [42] with the Nelder-Mead simplex search method [51] and this method will also be used in this work. It is a gradient-free optimization algorithm to find the minimum of a cost function (which, in this work, is the amount of energy harvested) with k variables. The simplex search method starts by computing the cost function for values of the variables that lie in the vertices of a simplex. This simplex is a polytope with $k + 1$ vertices in k dimensions, which is a triangle in two dimensions, a tetrahedron in three dimensions and so on. The initial simplex is an input to the algorithm by the user. After that, the algorithm takes over and tries to find the minimum of the cost function by following a set of actions: reflection, expansion, contraction and shrink (see Figure 5-2).

Step one is to perform a reflection. The worst point is chosen as the point to reflect away from. Then based on the function value of this new point, a next action is chosen. If the reflected point is the best of all points, expansion is chosen as the next action and the best of either the expanded or reflected point is chosen as a vertex in a new simplex, replacing the worst point in the old simplex. Then it goes back to step one.

If the reflected point of step one is the worst or second worst point of all points, a contraction is performed. The contracted point replaces the worst point and forms a new simplex if it has a better function value, if not, then the shrink action is performed and the algorithm goes back to step one.

If neither expansion nor contraction can be done after step one, the reflected point replaces the worst point in the simplex and the algorithm goes back to step one.

The algorithm stops when the difference in function values of the vertices becomes too small and/or the simplex itself becomes too small. The Nelder-Mead simplex method does not allow for constraints, but they can be included in the model itself.

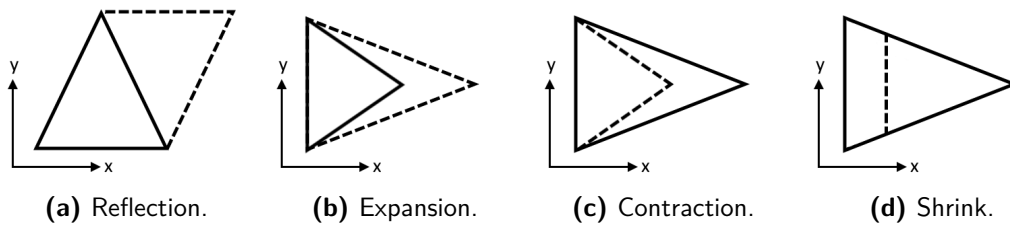


Figure 5-2: Nelder-Mead simplex method actions. Solid line is the old simplex and dashed line is the new simplex.

The overarching control method is depicted in Figure 5-3. Step one is providing the necessary information for the model, such as the sea state and the number of pontoons. Then the optimizer (with the simplex method) uses the model to find the best values for K_p and K_d . These values are then transferred to the array as the spring and damping coefficients. The process starts again with step one when the sea state changes.

It is possible to compute optimal K_p and K_d for each sea state beforehand and store this in a look-up table if computation times are too long.

Chapter 4 mentioned that it is possible for the power of the PTO mechanism to reverse (i.e. power is used instead of captured). This used power will be divided by the PTO efficiency as more (electric) power has to be put in the mechanism than comes out because of losses such as friction. Power is reversed for Reactive control when K_p is great enough, but will never be reversed for Resistive control. Figure 5-4 shows the negative captured power and positive used power for optimized Resistive and Reactive control. One can see that reversals of the power flow indeed happen for optimized Reactive control.

5-3 Distributed control

As the dimension of an optimization problem becomes larger, so does the size of the solution space (exponentially). This makes it harder to find the optimum value of a function in higher dimensions and is called the "curse of dimensionality" [52]. The simplex method described in this chapter also makes less progress per iteration with increasing dimensionality [53]. It is therefore possible that a distributed control scheme, where there are many controllers with a lower dimension, performs better than a global algorithm. A distributed scheme for PID controllers is proposed by Vázquez et al. [54]. The controllers are iteratively tuned for a multi-variable problem until design specifications are met.

A scheme similar to Vázquez et al. [54] is proposed here in Figure 5-5, where energy is the measure of performance instead of design specifications and the tuning method is the simplex algorithm. This scheme would replace the "find optimal control parameters" block in Figure 5-3. The algorithm starts with initial values for K_p and K_d for all controllers (equal to the number of PTO mechanisms). Next, each controller is optimized separately, but energy is computed for the whole array, to take interaction effects between pontoons into account. The optimized values of K_p and K_d are the starting points for a new iteration and this keeps going until the difference between iterations falls below a certain level. A difference of 1% is used in this work, as this would in practice be an acceptable loss, but other values can be chosen as well that suit the goal of the user. Chapter 6 shows that the computation time of

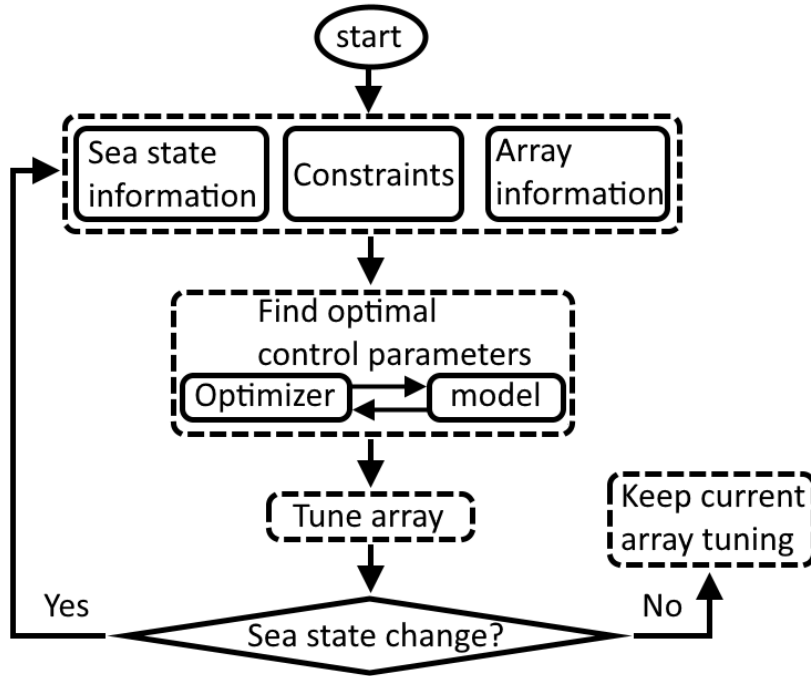


Figure 5-3: Scheme of the overarching control method for Resistive and Reactive control. Adapted from [49].

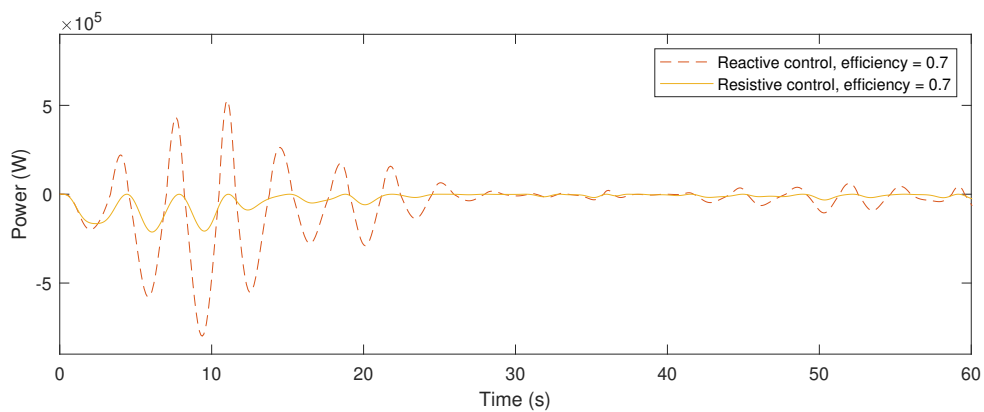


Figure 5-4: Power generated and used by the power take-off mechanism of a 2×1 array. Simulated for random seas with $H_s = 2.25$ m, $T_p = 6.50$ s and waves coming at 0° .

the distributed algorithm is greater when there are few pontoons, but becomes smaller than global control at five pontoons and higher when Reactive control is used.

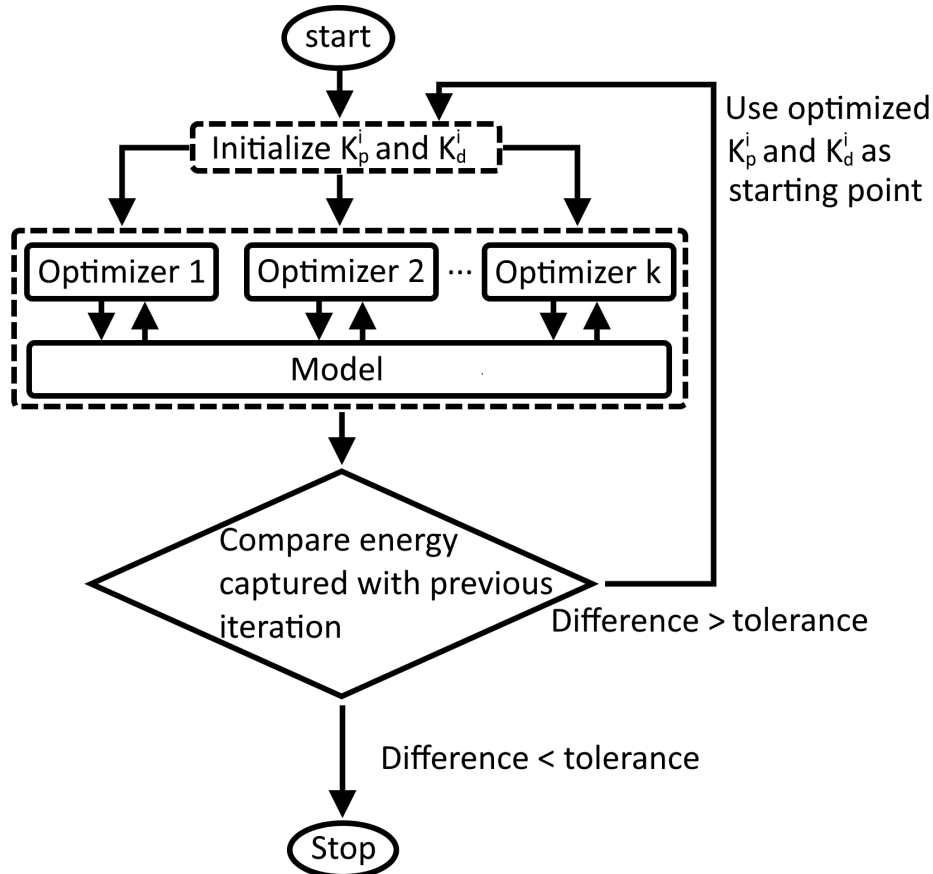


Figure 5-5: Distributed control scheme.

5-4 Stability

Pontoons that lie in the water experience drag and this damping makes it unlikely that they go unstable. However, for good measure, a stability analysis is performed in this section for a 2×1 array. The dynamics of the PTO mechanism are non-linear and one dimensional. The dynamics must thus be linearised for the use in a single-input single-output Bode plot. To make the system simpler and linearised, we assume that the pontoons only move in horizontal direction x . The displacement of the PTO mechanism, which is the output, can then linearly be computed as follows:

$$z = L_{bar} = x_B - x_A - w \quad (5-4)$$

Where A is the left pontoon, B is the right pontoon and w is the pontoon width.

The power capture of this linearised system only differs from the original with 5.60%. The open loop is minimum phase and stable because all poles and zeros lie in the left half plane

[55]. It must be noted that a small spring constant of 0.00001 N/m was applied on the horizontal position of the pontoons to make the model open-loop stable, if not, then there is a pole at 0 rad/s . This pole is due to the fact that there is nothing pulling the pontoons back to their original position if they get a velocity. The very small spring constant does not influence the Bode plot however in the range plotted in Figures 5-6 to 5-8.

Figure 5-6 shows the Bode plot of the open loop without controller. One can see that it resembles a second order system with very little stiffness and some perturbations around 1 rad/s . These perturbations are caused by the frequency dependent damping that comes from the water. The bode plots of the open loop with controller, i.e. the loop transfer, can be found in Figures 5-7 and 5-8. The system with Resistive controller has a phase margin (PM) of 97.1° and an infinite gain margin (GM). For Reactive control with an efficiency of 1.0 , the PM is 16.5° and the GM is infinite as well. This means that the closed loop is stable for both controllers. The closed loop is less stable when Reactive control is used than the recommended PM of 30.0° [55]. It is thus quite susceptible to phase delay. The disk margin is 0.288 which is also lower than recommended. It is logical however that the Reactive controller is less stable because in a sense it is trying to become unstable. It wants to become unstable because it tries to reach resonance with the dominant wave frequency. This will be analysed in Chapter 7.

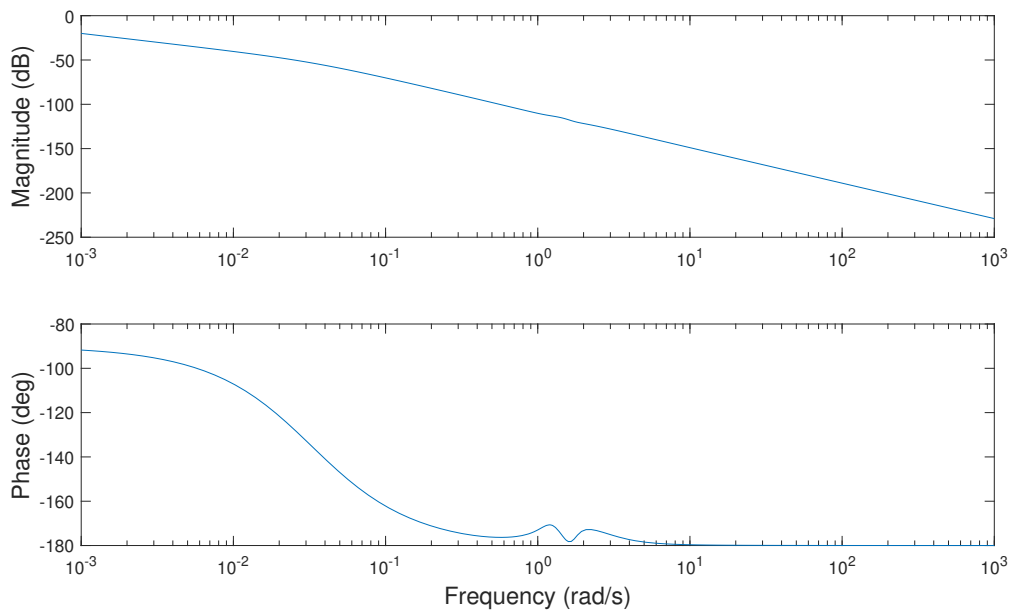


Figure 5-6: Bode plot from force to displacement of the power take-off mechanism.

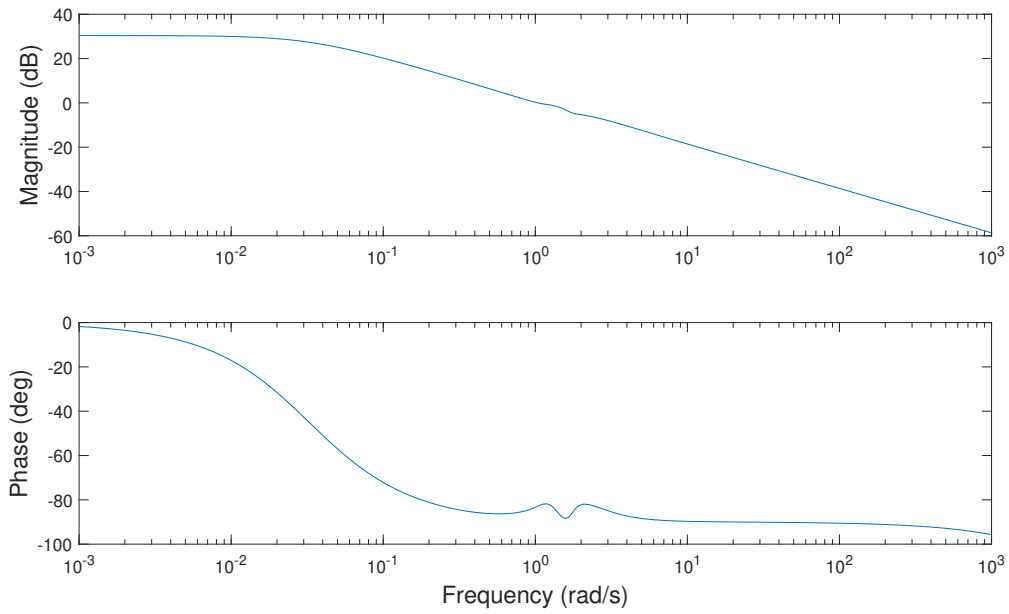


Figure 5-7: Bode plot of the loop transfer with Resistive Control.

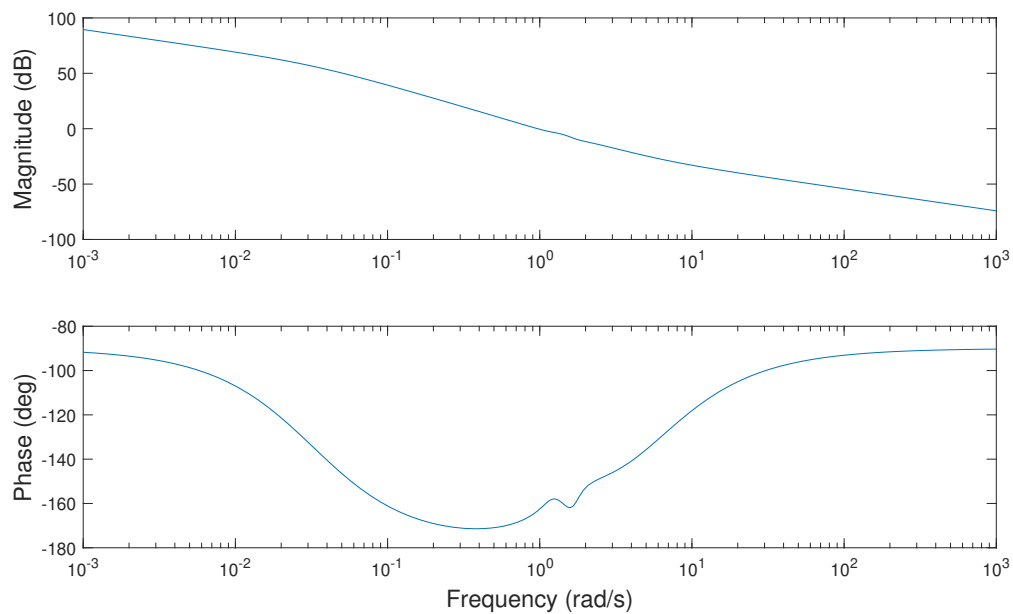


Figure 5-8: Bode plot of the loop transfer with Reactive Control.

Chapter 6

Results

This chapter shows the results of the numerous optimizations done for different aspects of the wave energy converter (WEC) array designed in this report. Most are done for waves coming at an angle of 0° , as about 75% of the waves come at this angle (see Figure 2-5), but Section 6-8 presents results of what happens when waves come at a 45° angle. Waves that come at an angle of 0° are directed straight at the array, in line with the linear generators, as is shown in Figure 6-1. In this case, only an array of pontoons behind each other ($n \times 1$) has to be simulated, because all pontoons next to each other would have the same control coefficients and the same energy production, as was mentioned in Section 4-3.

The next section shows a plot of how the pontoons move, the section after that explains how the simulation duration was chosen, the sections after that present results of optimized energy production for Resistive and Reactive control and the last section shows the scalability of the control methods. Values for captured energy are positive in this chapter (as opposed to the previous chapter) to improve readability.

6-1 Pontoon movement

Figure 6-2 shows the movement of two pontoons with waves coming straight at the array (at 0°). The damping and stiffness coefficients are optimized for the dominant sea state for Reactive control with an efficiency of 1.0. One can see that the movement of the pontoons with respect to each other is about 4 m in the horizontal direction (x) and this was used for the system design in Section 3-5.

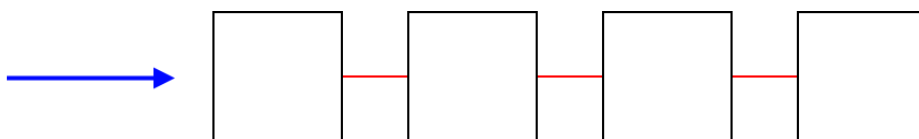


Figure 6-1: Top view of a 4×1 array with 0° wave direction indicated by the arrow.

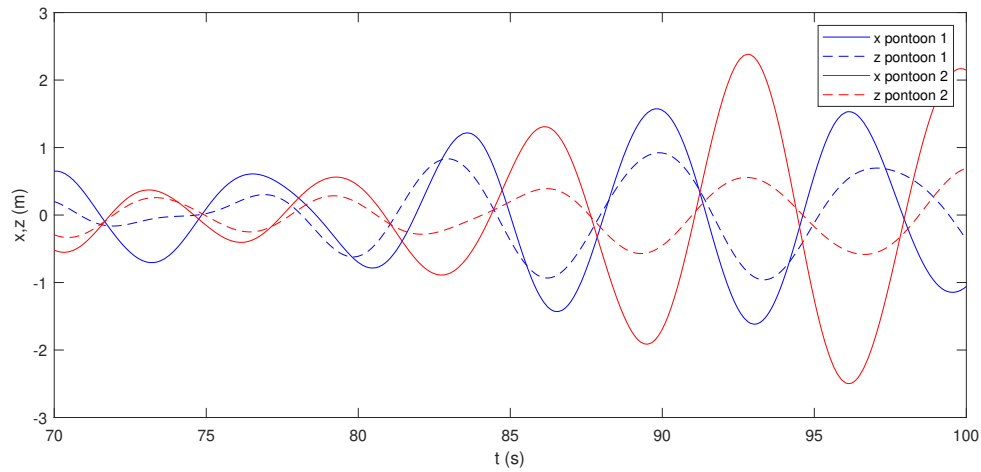


Figure 6-2: Example of typical horizontal (x) and vertical (z) displacement of the two pontoons with respect to their starting position in a 2×1 array. Simulated for random seas with $H_s = 2.25$ m, $T_p = 6.50$ s and waves coming at 0° .

6-2 Simulation duration

First a simulation duration has to be chosen. This is preferably as short as possible, as this reduces the time it takes to run the simulation. However, waves are generated with random phase, so some variability in energy production and optimal control coefficients will occur. This is preferred to be as small as possible and variability reduces with simulation duration, so a compromise has to be found between computation time and variability. This was found to be a simulation duration of 2 hours. Ten optimization runs for all forms of control for a duration of 2 hours show that the variability between greatest and smallest value in energy is 4.96%. For K_p and K_d this is 0.664% and 4.01% respectively, which was deemed acceptable. See Appendix D-1 for values of energy production and optimization variables for each run.

6-3 Energy production per generator

In the system design in Chapter 3, it was mentioned that energy should be harvested for all degrees of freedom, but that some might be less interesting to harvest than others. This section shows results of the amount of energy harvested for the single linear and two rotary generators for an array of two pontoons to see if all degrees of freedom are worth harvesting. One can see in Table 6-1 that the two rotary generators only harvest between 18.6% and 31.0% of the total energy. This is too low to warrant using the rotary generators, so it was decided to only keep the linear generator. The next sections show results of energy capture with only linear generators between the pontoons.

Table 6-1: Energy capture of a 2×1 array with one linear and two rotary generators. Simulated for random seas with $H_s = 2.25$ m, $T_p = 6.50$ s and waves coming at 0° .

Control method	Resistive	Reactive	Reactive
Efficiency	0.700	0.700	1.00
Total energy capture	3.33×10^8 J	5.98×10^8 J	1.73×10^9 J
Rotary generators	23.6 %	18.6 %	31.0 %
Linear generator	76.4 %	81.4 %	69.0 %

6-4 Influence of the number of pontoons on energy capture

As the number of pontoons increases, so does the amount of energy harvested. Figure 6-3 shows the increase in energy when another pontoon is added to a $n \times 1$ array with linear generators. One can see that the increase in energy generally declines with increasing number of pontoons, except for Reactive control when going from an odd to an even number of pontoons. This could be explained by the fact that for even number of pontoons, the optimized solution for energy generation is for the pontoons to form pairs which oscillate at the peak frequency of the spectrum and to set the connections in between with small control coefficients (i.e. almost free movement). For uneven number of pontoons, there is always one pontoon which cannot be in a pair. Chapter 7 will go deeper into the subject of eigenfrequencies of the pontoons.

The choice for the number of pontoons behind each other in the array will be one of costs. As Figure 6-3 shows, the amount of energy generated does not increase equally with the number of pontoons. For example, when using three pontoons instead of two in the array, an increase in the number of pontoons by 50 %, then the energy capture increases with only 12 % at best. If the cost of the array grows equally with the number of pontoons (which is assumed here), then it is the most cost efficient to design the array as a $2 \times n$ array.

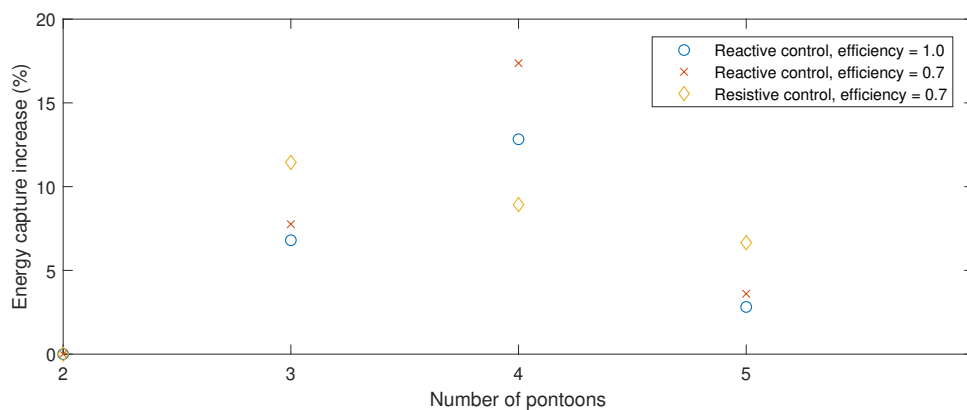


Figure 6-3: Relative increase in energy when an extra pontoon is added to the array. Simulated for random seas with $H_s = 2.25$ m, $T_p = 6.50$ s and waves coming at 0° .

6-5 Influence of pontoon spacing on energy capture

A pontoon spacing was chosen in Chapter 3 based on the peak period of the sea state with the highest average energy. To see if this was indeed the right choice, some optimization runs are done for different pontoon spacings. Figure 6-4 shows the results of these runs for a 2×1 array with linear generators.

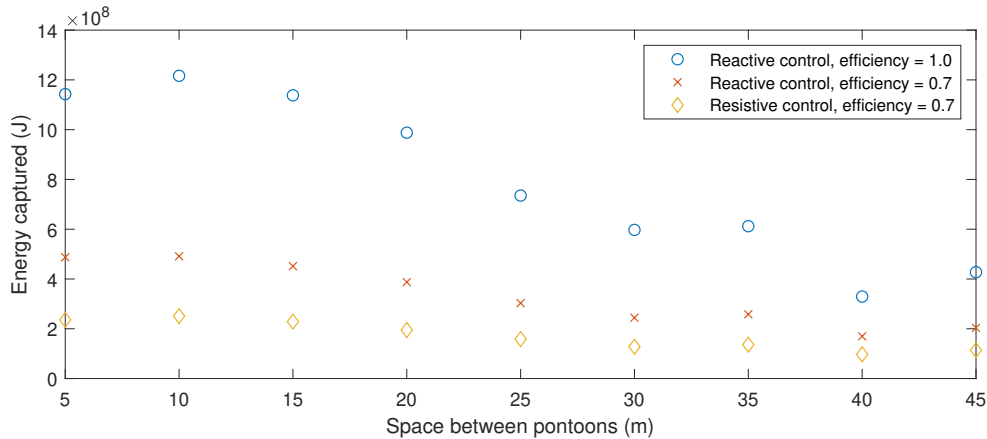


Figure 6-4: Energy capture versus pontoon spacing for a 2×1 array. Simulated for random seas with $H_s = 2.25$ m, $T_p = 6.50$ s and waves coming at 0° .

6-6 Influence of pontoon height on energy capture

A pontoon height was chosen in Chapter 3 based on results of optimization runs in Figure 6-5. It shows that energy capture increases up to a height of 6 m and remains around the same level when the height increases further.

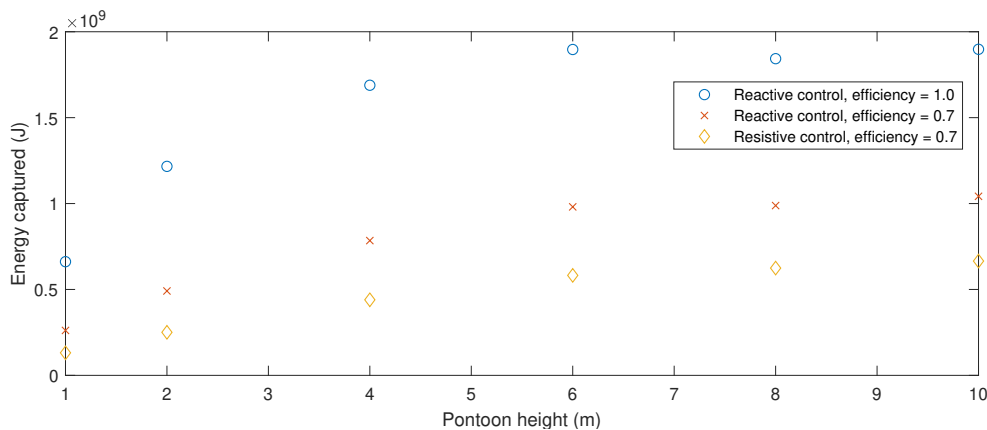


Figure 6-5: Energy capture versus pontoon height for a 2×1 array. Simulated for random seas with $H_s = 2.25$ m, $T_p = 6.50$ s and waves coming at 0° .

6-7 Sea states overview

So far, all simulation runs have been done for the dominant sea state with $H_s = 2.25$ m and $T_p = 6.50$ s. There are however many other sea states that contribute to the average power production, as can be seen in Table 2-3. Optimization runs were done for all sea states that have a higher than 1.00% part in the energy production. The results for energy capture are presented in Table 6-2 expressed as a percentage of the total energy that is present in the waves along the width of the pontoons. The power in the waves per meter wave crest was calculated using the method described in Section 4-1. The raw data of the amount of energy harvested can be found in Appendix D-2.

Table 6-2: Overview of energy capture by a 2×1 array for random seas with 0° wave direction. Values are in percentage of the total energy in the waves of each sea state. Top: Reactive control with an efficiency of 1.0, middle: Reactive control with an efficiency of 0.7, bottom: Resistive control with an efficiency of 0.7.

H_s (m)	3.5-6.0				39.2	25.0	15.3
	3.0-3.5				39.0	26.4	
	2.5-3.0			50.0	40.0		
	2.0-2.5			49.0	41.4		
	1.5-2.0		36.4	49.7			
	1.0-1.5	18.3	36.7	52.2			
	0.5-1.0	21.0	17.8	36.3	49.3		
	3-4	4-5	5-6	6-7	7-8	8-9	9-10
	T_p (s)						

H_s (m)	3.5-6.0				16.0	10.8	6.90
	3.0-3.5				15.8	10.9	
	2.5-3.0			19.8	16.0		
	2.0-2.5			20.3	16.2		
	1.5-2.0		16.9	19.5			
	1.0-1.5	7.83	15.9	20.2			
	0.5-1.0	7.59	6.95	15.9	20.2		
	3-4	4-5	5-6	6-7	7-8	8-9	9-10
	T_p (s)						

H_s (m)	3.5-6.0				8.46	5.67	3.78
	3.0-3.5				8.10	5.60	
	2.5-3.0			10.5	7.99		
	2.0-2.5			10.6	7.85		
	1.5-2.0		9.04	10.3			
	1.0-1.5	4.60	8.77	9.99			
	0.5-1.0	3.67	3.99	8.46	9.91		
	3-4	4-5	5-6	6-7	7-8	8-9	9-10
	T_p (s)						

6-8 Waves at a 45° angle

So far, all simulation runs are done for a 0° wave direction and although this is the direction that most waves will have, it is interesting to see what happens to the optimal control parameters and energy capture when waves come at an angle. The chosen array size for this experiment is 2×2 . The amount of wave energy that is available to the array is 3.44 times larger than for the 2×1 array with 0° wave direction, because the wave crest that comes in contact with the 2×2 array (the diagonal of the whole array) is 3.44 times larger than for the 2×1 array (the width of one pontoon).

With Resistive control, the energy capture of the 2×2 array is 2.61 times the energy capture of the 2×1 array with the same control strategy. For Reactive control with an efficiency of 0.7 and 1.0, it captures 3.27 and 2.68 as much respectively. The optimal damping and stiffness constants of the 2×2 array are within 36.1% and 17.7% of the constants of the 2×1 array respectively for all forms of control.

6-9 Scalability control method

The number of iterations necessary for global optimization in Section 6-4 were counted to see how the computation time of the method increases with the number of pontoons. The same was done for distributed optimization and the results can be found in Figure 6-6. Reactive control with an efficiency of 1.0 was left out because the results were very similar to 0.7 efficiency and made the figure less readable. The energy captured with distributed optimization was at most 2% lower than global optimization for Reactive control and was the same for Resistive control. The global algorithm needs fewer iterations than the distributed algorithm when there are few optimization variables, but needs more iterations when ten or more variables need to be optimized.

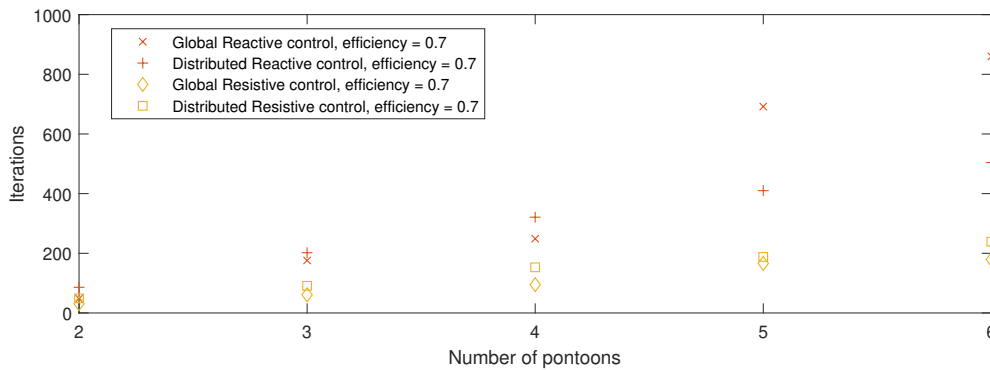


Figure 6-6: Number of optimization iterations versus number of pontoons for a 2×1 array. Simulated for random seas with $H_s = 2.25$ m, $T_p = 6.50$ s and waves coming at 0°.

Chapter 7

Discussion

This chapter first asks the question if the optima found in Chapter 6 are the best solutions to the optimization problem. Then, the performance of the array designed in this work is compared to prior art. Finally, it is discussed if more wave information can result in greater energy capture.

7-1 Eigenvalue analysis

In Chapter 5, the control problem and the optimization method was explained. In general, it is possible that optimizers get stuck in local minima and thus do not find the best solution. To see if this is the case in this work, the optimal values for the spring constants (K_p) that the optimizer has found can be compared to what is to be expected logically.

When there are no losses (i.e. efficiency = 1.0), then the expected value of the spring constants are such that the natural frequencies (ω_n) of the wave energy converter (WEC) array lie at the frequency of the waves and resonance occurs. For monochromatic waves, this would be the frequency of the wave and for sea states, this would be around the peak frequency (which is the inverse of the peak period). Data of spring and damping constants that the optimizer found for monochromatic waves and random seas can be found in Table 7-1. The natural frequencies of the array can be found there as well. To compute these, the array is simplified to masses and springs, as shown in Figure 7-1. Three pontoons are depicted in the figure as an example, but the eigenfrequencies of the array can be computed for any number of pontoons. The first step in computing the eigenfrequencies is the derivation of the equations of motion [56] in the frequency domain:

$$\mathbf{F}(t) = \mathbf{m}\ddot{\mathbf{x}}(t) \tag{7-1}$$

$$\mathbf{m}\ddot{\mathbf{x}}(t) + \mathbf{K}\mathbf{x}(t) = 0 \tag{7-2}$$

$$(-\mathbf{m}\omega^2 + \mathbf{K})\mathbf{X}(\omega) = 0 \tag{7-3}$$

Then, the natural frequencies are computed by taking the determinant of $(-m\omega^2 + \mathbf{K})$, equalizing it to 0 and solving for ω . For the system in Figure 7-1, this matrix and $\mathbf{X}(\omega)$ look as follows:

$$(-m\omega^2 + \mathbf{K}) = \begin{bmatrix} -m\omega^2 + K_{p1} & -K_{p1} & 0 \\ -K_{p1} & -m\omega^2 + K_{p1} + K_{p2} & -K_{p2} \\ 0 & -K_{p2} & -m\omega^2 + K_{p2} \end{bmatrix} \quad (7-4)$$

$$\mathbf{X}(\omega) = \begin{bmatrix} X_1(\omega) \\ X_2(\omega) \\ X_3(\omega) \end{bmatrix} \quad (7-5)$$

The mass of the system changes with its resonating frequency due to the moving water, as mentioned in Chapter 4. Therefore an iteration scheme is applied. It starts by first computing the natural frequencies without the added mass, then computes the added mass at that frequency and then computes the eigenfrequencies again. This continues until convergence.

The real system not only has springs, but also damping and this influences the natural frequency. How much this affected the natural frequency was checked in simulation by giving the pontoons an offset to their initial position. The found value of the damped natural frequency was 4.85% lower than the undamped natural frequency.

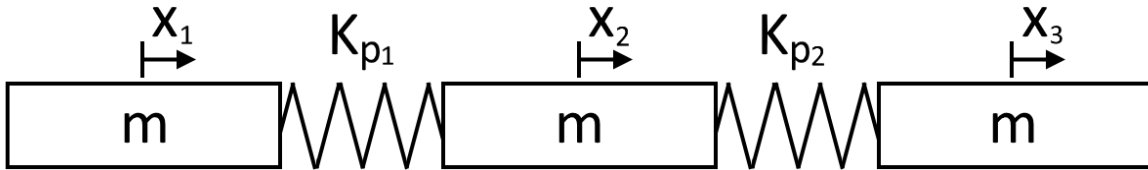


Figure 7-1: Mass-spring model for the array.

What can be learned from the undamped natural frequency in Table 7-1 for arrays with two pontoons, is that they lie close to the wave frequency of monochromatic waves and to the peak frequency of random waves. When there are four or more pontoons, then pairs are formed that again have their natural frequency close to the wave frequency. This shows that the optimized K_p indeed lie at the global optimum.

Furthermore, the eigenfrequencies of the array can be linked to the effect of efficiency on energy capture. In Table 6-2, one can see that the energy capture of Reactive control with an efficiency of 0.7 divided by 0.7 is lower than energy capture with an efficiency of 1.0. This is caused by the lower natural frequency of the array with 0.7 efficiency, because lower values of K_p save energy when there is efficiency to be accounted for (as was explained in Chapter 4).

7-2 Comparison with other wave energy converters

A measure to compare performance of WECs in terms of power capture is the capture width ratio (CWR). It is a measure of the hydrodynamic efficiency, η_{hyd} [57], and is defined as follows:

$$\eta_{hyd} = \frac{P_{abs}}{wJ_{wave}} \quad (7-6)$$

Table 7-1: Optimized K_p , K_d and natural frequencies for monochromatic and random waves with a 0° wave direction.

Type	Wave		Array Size	$K_p \times 10^5$ (N/m)	$K_d \times 10^4$ (Ns/m)	Inverse of natural frequency (s)
	Period (s)	Height (m)				
Mono-chromatic	5.00	2.00	2×1	4.65	5.61	5.17
	6.00	2.00	2×1	3.50	5.03	5.98
	7.00	2.00	2×1	2.62	3.52	6.92
	8.00	2.00	2×1	2.00	2.56	7.92
Random	6.50	2.25	2×1	3.00	5.52	6.41
	6.50	2.25	3×1	2.72, 1.83	3.41, 5.04	6.39, 8.94
	6.50	2.25	4×1	2.98,	5.58,	6.48, 6.52,
				4.00×10^{-2} , 2.94	7.85×10^{-4} , 4.70	7.83×10

Where P_{abs} is the absorbed wave power (mechanical power), J_{wave} is the amount of power in the wave crest per meter and w is the characteristic width of the device.

The result is a dimensionless number that describes the ratio of power in the wave that the device is able to absorb along its characteristic width. The data for energy capture per sea state in Table 6-2 are presented as electrical power divided by the power in the waves, so if the data in these tables are divided by the efficiency of their corresponding power take-off (PTO) mechanism, then one would get the CWR. The average CWR throughout the year can then be computed by taking the weighted average of these with the weights in Table 2-2. Chapter 2 showed that 75 % of the waves come from the preferred direction. The energy capture for the other 25 % will be lessened by the factors found in Section 6-8 as a crude estimation for all other directions than the preferred direction. These factors were computed by dividing the power production per meter wave crest of a 2×2 array under 45° waves by that of the same array under a 0° wave direction. The values for the CWR under different wave directions and control methods can be found in Table 7-2.

Table 7-2: Overview of capture width ratios (CWRs) for all control methods and wave directions (WDs).

Control	Efficiency	CWR dominant WD	CWR other WDs	Average CWR
Reactive	1.00	39.0 %	30.4 %	36.8 %
Reactive	0.700	23.0 %	21.9 %	22.7 %
Resistive	0.700	12.1 %	9.17 %	11.4 %

The average CWR in this work can be compared to that of other WECs. Such a comparison has been made by Babarit [58] in Figure 7-2 for many different WEC types and sizes under passive control. This passive control is presumably the same as Resistive control but is not further explained. Some of the sources used by Babarit [58] do explain the type of control that they used and this is indeed Resistive Control. The category that the array in this thesis falls in is the ‘floating oscillating wave surge converter (OWSC)’ category, as it captures most of its energy in the surge (horizontal) direction. The characteristic dimension is the width of the pontoons, 23 m. One can see that the value of the CWR for Resistive control is about

average for the floating OWSCs group. It surpasses all other floating OWSCs when Reactive control is used, but this is not a fair comparison since the results for other OWSCs do not use this more advanced form of control.

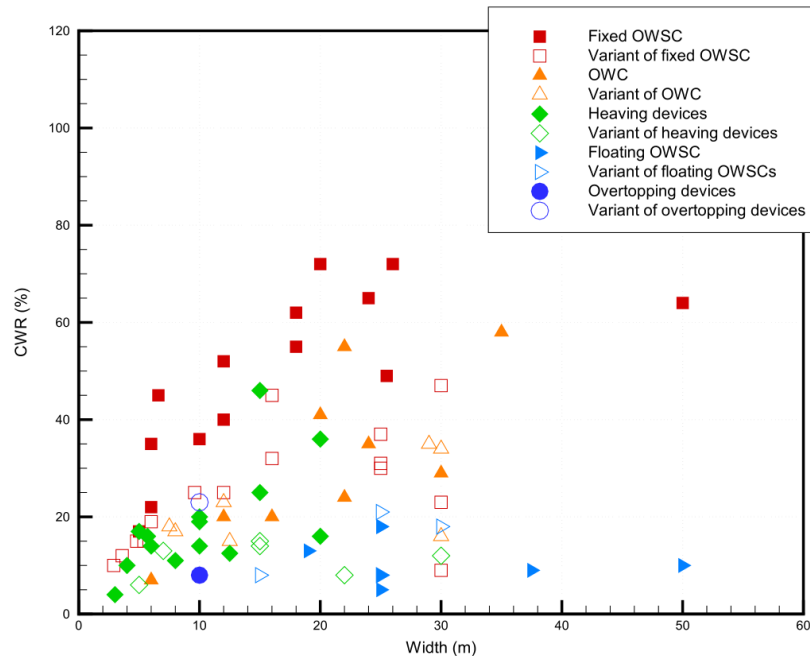


Figure 7-2: Capture width ratio for wave energy converter types and sizes, from Babarit [58].

7-3 Improvement on energy capture with more wave information

The control method used in this work uses sea state information to optimize its parameters. This means that it is not optimized per wave, but for the ‘average’ wave in the sea state and thus energy will not be optimally harvested for all waves. There are more advanced controllers, such as MPC [59, 60] that optimize their control input for each incoming wave. To see how much such methods can improve upon Reactive control, the energy production of the dominant sea state can be compared to energy production of a monochromatic wave with the same energy and a period that is the weighted average of the sea state. A wave with the same energy as the dominant sea state was computed by using the same procedure as in Chapter 4, but instead of 1000 waves, only one wave was used. The height and period of the monochromatic wave are 1.58 m and 5.91 s respectively. Equation (2-1) can be used to check that indeed, the average power in the monochromatic wave is the same as the dominant sea state (14.5 kW/m).

The energy captured for this monochromatic wave in comparison to random waves can be found in Figure 7-3. One can see that the captured energy is between 15 % and 50 % greater than when sea state information is used, but this percentage is smaller when the number of pontoons increases. An explanation for this is that for monochromatic waves, the first two pontoons already take most of the power out of the waves, so that there is not much left for the other pontoons. Reactive control with an efficiency of 1.00 extracts 75.6 % of the total

power in monochromatic waves. For random seas this is 50.6 %, which leaves more energy for the other pontoons to collect.

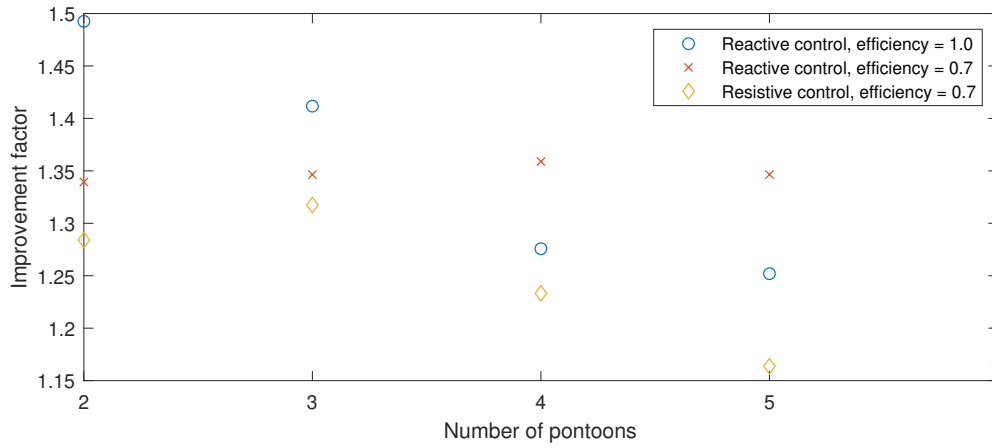


Figure 7-3: Comparison of energy capture between arrays in monochromatic and random waves. The improvement factor is computed by dividing energy capture of arrays in monochromatic waves by energy capture in random waves.

Chapter 8

Proof of concept

This chapter gives an example of how the system design in Chapter 3 can be implemented in reality. It is not necessarily the best design, but its purpose is to show the usability of the system design.

8-1 Top view design

The top view design is changed slightly with respect to the one in Chapter 3. It was not designed to withstand rotation around the vertical axis there, which is something that it should be able to do in practice. For this reason, the single connections in the centre of the pontoons are replaced by two connections more to the sides, as can be seen in Figure 8-1. When the pontoons intend to rotate around their vertical axis, then the connections present a countering torque to push the pontoons back to their original orientation. The stiffness and damping constants of the connections should be halved in order to keep the same dynamical behaviour for energy harvesting.

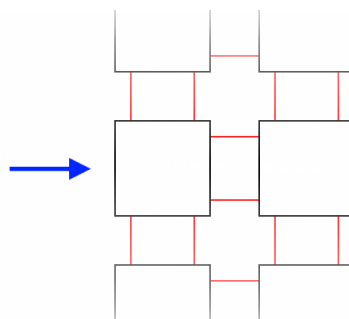


Figure 8-1: Top view of the proof of concept design. Pontoons are drawn in black, connections in red and the blue arrow is the dominant wave direction.

8-2 Power take-off mechanism

Reactive control described in Chapter 5 uses parameters K_p and K_d . These parameters can be seen as ideal springs and dampers respectively. The power take-off (PTO) mechanism can use real springs and dampers (hydraulic pistons) to get approximately the same behaviour as in the mathematical model. The stroke of the PTO as determined in the system design in Chapter 3 is 8 m, on which a 25 % safety margin will be applied. Thus the stroke is 10 m and the spacing between pontoons should be minimized to keep the bending moment as low as possible and maximize space efficiency. The absolute minimal possible spacing is 5 m, as the maximum stroke is 10 m. However, the mechanism itself needs space as well, so this minimal spacing cannot be reached. The next subsections explain the mechanisms that act as dampers and springs and how the space between pontoons is minimized.

8-2-1 Dampers

Ideal viscous dampers can be approximated by hydraulic pistons, as is done by Cargo et al. [61]. They design a hydraulic piston and motor combination for a wave energy converter (WEC) that consists of a buoy that moves up and down and is connected to the ground through the piston. The same system can be applied to the array designed in this work, where the pistons reside in the connections and the motors in the pontoons. A simplified hydraulic system is depicted in Figure 8-2. Four check valves rectify the flow coming from the piston, such that the motor always gets the same flow direction and a buffer can be build up in accumulators A (high pressure) and B (low pressure). An electric generator is connected to the hydraulic motor to generate electricity.

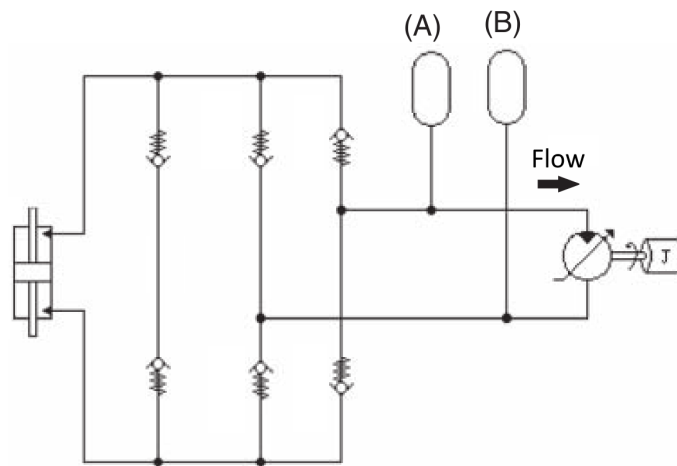


Figure 8-2: Schematic of the hydraulic part of the power take-off mechanism. Adapted from Cargo et al. [61].

The hydraulic motor is of the variable displacement type, because this makes it possible to adjust the damping constant. Variable displacement motors and pumps have been researched for some time [62–68] and can be bought from several suppliers [69–71]. An important component of a variable displacement motor is a disk under an angle, which is called the swash plate. Pistons are connected to it in a circle, as can be seen in Figure 8-3. When pressurized

fluid pushes the pistons out, the swash plate rotates and when the pistons are on their way back, they are connected to a low pressure reservoir to get a steady rotation. The amount of fluid that flows through the motor per rotation (the motor displacement) can be regulated by varying the angle of the swash plate.

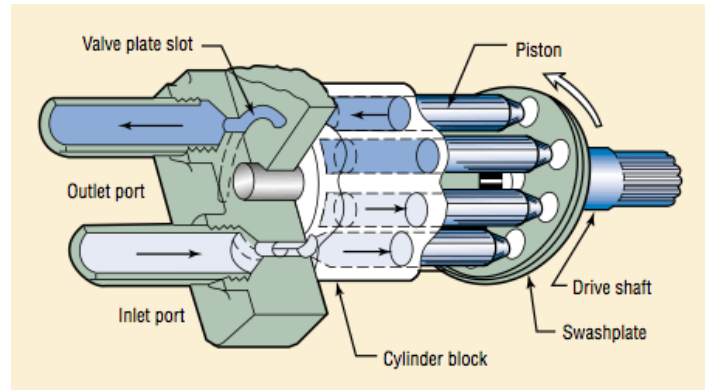


Figure 8-3: Working principle of a variable displacement motor, from [72].

A hydraulic piston functions differently than a pure viscous damper because it is governed by several differential equations regarding flow and pressure. Furthermore, it only starts moving when the force on the piston becomes greater than the pressure differential in the accumulators multiplied with the piston area. Cargo et al. [61] therefore not talk about damping for hydraulic pistons, but effective damping (α), which has the same units as regular damping and can be computed from piston parameters as follows:

$$\alpha = \left(\frac{A_p}{D_{hm}} \right)^2 b_{gen} \quad (8-1)$$

Where A_p is the surface area of the piston, D_{hm} is the motor displacement and b_{gen} is the damping coefficient of the electric generator.

Cargo et al. [61] perform simulations with viscous dampers and hydraulic pistons, to see which system can perform better and what the optimal parameters are. They find out that the WEC captures more energy with a hydraulic piston than a viscous damper and that the optimal effective damping for the hydraulic piston is 1.5-2 times greater than for the viscous damper. The optimal viscous damping coefficients in this work for an efficiency of 1.0 lie between 3.51×10^4 and 7.04×10^4 N s/m, with a value of 5.52×10^4 N s/m for the dominant sea state that lies approximately in the middle of this range, as can be seen in Table D-4. One can design the approximate dimensions of the hydraulic system with the power that is generated in the viscous damper case, its viscous damping coefficient, the relationship found between effective and viscous damping [61] and realistic hydraulic motor and electric generator parameters. These values for the dominant sea state can be found in Table 8-1 and some were computed using Equations (8-2) to (8-5) [61].

$$P_{hm} = \Delta p_{hm} D_{hm} \omega_{hm} \quad (8-2)$$

$$\Delta p_{hm} = p_A - p_B \quad (8-3)$$

$$b_{gen} = \frac{T_{gen}}{\omega_{gen}} = \frac{P_{gen}}{\omega_{gen}^2} \quad (8-4)$$

$$F_p = A_p \Delta p_{hm} \quad (8-5)$$

Where among previously mentioned variables, P_{hm} and P_{gen} are the power of the hydraulic motor and electric generator respectively, p_A and p_B are the pressure in accumulators A and B, ω is angular velocity of the generator and motor, T_{gen} is the generator torque and F_p is the piston force.

Table 8-1: Data and computed parameters for the hydraulic part of the power take-off mechanism. Top: Specifications from manufacturers. Middle: Power and viscous damping for a 2×1 array in random seas with $H_s = 6.50$ m, $T_p = 6.50$ and 0° wave direction. Bottom: Computed parameters for the hydraulic part of the power take-off mechanism.

Parameter	Symbol	Value	Source
Rated power of generator FLSES 315LB	$P_{gen,max}$	200 kW	[73]
Rated speed of generator FLSES 315LB	$\omega_{gen,max}$	$2\pi \frac{1514}{60}$ rad/s	[73]
Range motor displacement of motor FMV 250	D_{hm}	110-257 cm ³ /rev	[69]
Average motor displacement of motor FMV 250	\bar{D}_{hm}	184 cm ³ /rev	[69]
Max pressure of motor FMV 250	p_{max}	380 bar	[69]
Average PTO power	\bar{P}_{hm}	130 kW	Section 8-3
Average electric power	\bar{P}_{gen}	104 kW	Section 8-3
Optimized viscous damping constant PTO	K_d	5.52×10^4 N s/m	Table 7-1
Average Pressure difference accumulator A and B	$\Delta \bar{p}_{hm}$	281 bar	Equation (8-2)
Damping coefficient electric generator	b_{gen}	4.18 Nm/(rad/s)	Equation (8-4)
Surface area piston	A_p	4.40×10^{-3} m ²	Equation (8-1)
Force piston at average pressure	\bar{F}_p	124 kN	Equation (8-5)

To see if the values found in Table 8-1 make sense, one can compare the force at the average pressure, with the force that is exerted by the optimized viscous damper in random seas. Figure 8-4 shows that the average force of the hydraulic piston indeed lies in the range of the viscous damper force. The damping constant can be adapted to each sea state by changing the motor displacement D_{hm} according to the desired damping and the relationship in Equation (8-1).

A regular hydraulic piston with a stroke of 10 m would mean a distance of 15 m in between pontoons at rest (20 m at maximum length and 10 m at minimum length). This can be seen in Figure 8-5a. The distance in between pontoons should be minimized, so a triple piston mechanism can be used to reduce this, as is shown in Figure 8-5b. It is possible to go to an even smaller minimum distance, but as can be seen in the next section, the spring is then the limiting factor and needs a minimum of 10 m in between pontoons. A triple piston mechanism is thus enough. The surface area of the outer two pistons summed should be equal to the inner piston, which is 2.20×10^{-3} m². This is the value found in Table 8-1 of A_p divided by two because there are two connections between the pontoons instead of one.

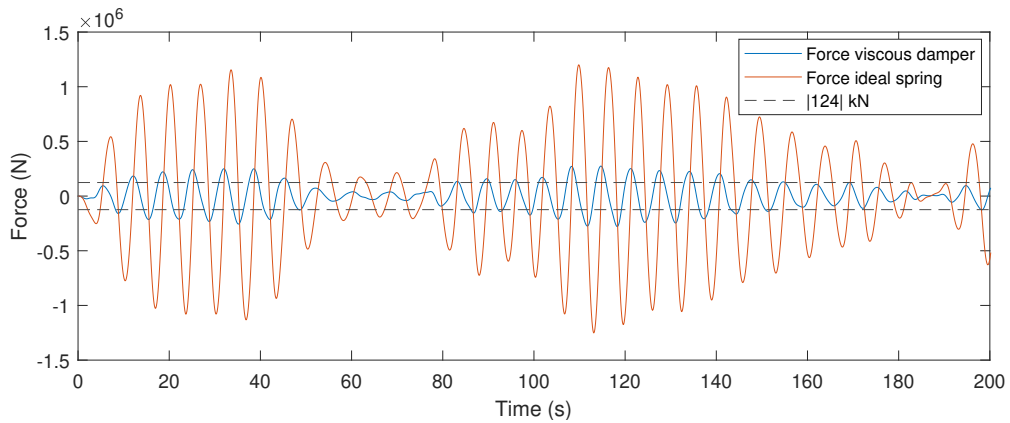
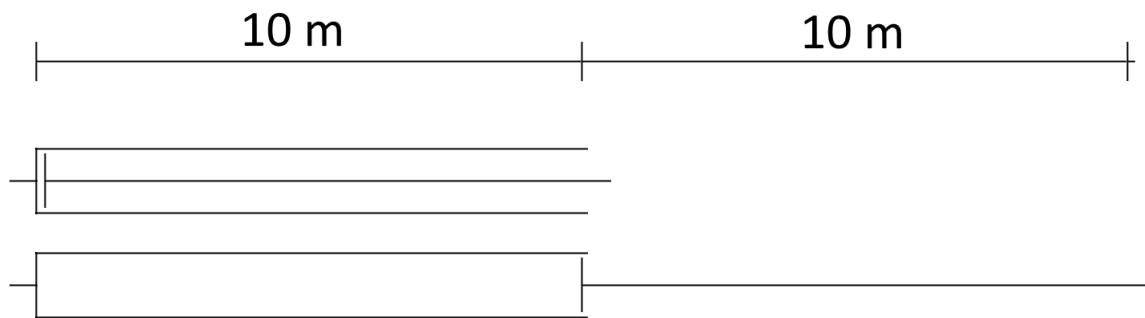
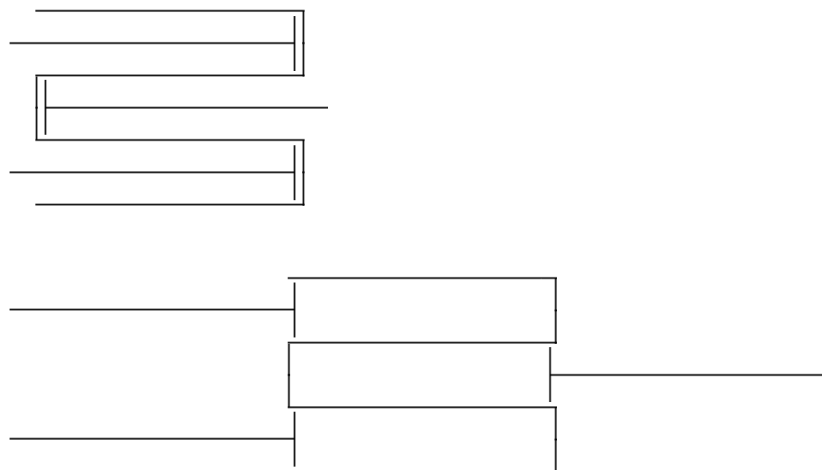


Figure 8-4: Forces exerted by optimized power take-off mechanism of a 2×1 array in random seas with $H_s = 6.50$ m, $T_p = 6.50$ and 0° wave direction.



(a) Single piston mechanism.



(b) Triple piston mechanism.

Figure 8-5: Schematic drawing of hydraulic piston mechanisms.

8-2-2 Springs

Ideal springs can be approximated by real springs. The dimensions of a real spring can be computed from the spring stiffness using the following formulas [74, 75]:

$$F_s = \frac{\pi d_s^3 \tau}{8D_s} \quad (8-6)$$

$$s_s = \frac{8F_s D_s^3 n_s}{G_s d_s^4} \quad (8-7)$$

$$k_s = \frac{F_s}{s_s} = \frac{G_s d_s^4}{8D_s^3 n_s} \quad (8-8)$$

$$\tau' = K_w \tau = \frac{8F_s D_s K_w}{\pi d_s^3} \quad (8-9)$$

$$K_w = \frac{4c_s - 1}{4c_s - 4} + \frac{0.615}{c_s} \quad (8-10)$$

$$c_s = \frac{D_s}{d_s} \quad (8-11)$$

$$t_s = \frac{s_s + s_{s,max}}{n_s} + d_s \quad (8-12)$$

where F_s = Spring force

d_s, D_s = Wire and spring diameter

τ = Uncorrected shear stress (used in static loading)

τ' = Corrected shear stress (used in cyclic loading)

G_s = Shear modulus

s_s = Deflection

n_s = Number of active spring coils

K_w = Wahl factor

k_s = Spring stiffness

c_s = Spring index

t_s = Pitch

Usually springs are either used in tension or compression, but these equations hold for both, with the exception that a tension spring might have pretension in it. The springs in this work need to be used in tension and compression, which is possible, but one must ensure that the spring is not overstretched, i.e. the pitch must not be too great. Compression springs usually have a maximum pitch of $0.5D_s$ [76] and care is taken that this value is not exceeded.

The spring constants found for all sea states are displayed in Table D-3. One can see that most lie between 2.41×10^5 and 3.68×10^5 N/m, the remaining values represent sea states where not enough energy is present to warrant the extra cost for the increased spring dimensions. One way to vary spring stiffness is to vary the number of windings (n_s), as can be seen in Equation (8-8). A mechanism to clamp to different parts of the spring in order to vary the active windings is depicted in Figure 8-6.

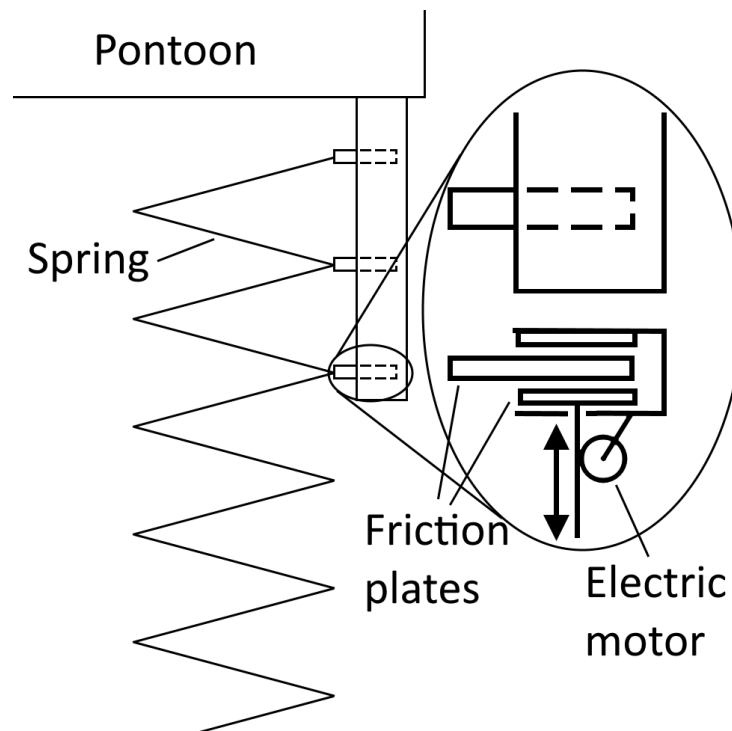


Figure 8-6: Schematic drawing of a variable winding spring. Overall drawing: Top view of mechanism with part of array. Zoomed drawing: Top view and front view of mechanism.

The spring is designed for the dominant sea state, which has a stiffness of 2.99×10^5 N/m. So when this is used as the basis, the variable winding spring design should allow for an increase in the number of windings with a factor of 0.81 to 1.23. The spring diameter should not be much larger than 2 m because that is the height of the pontoon. With some trial and error, it was noticed that this limited the minimum free length of the spring to around 8 m, which multiplied with a factor of 1.23 comes to around 10 m for the whole variable spring mechanism. Therefore the spring was designed to match the 10 m space in between pontoons that is necessary for the triple piston mechanism in Figure 8-5b. This means that the spring at the dominant sea state has a free length (L_0) of $\frac{10}{1.23} = 8.13$ m. This free length is designed by optimizing the spring index (c_s), which usually lies between 4 and 16 [74]. The rest of the parameters follow from Equations (8-8) to (8-11).

The spring dimensions that were found are shown in Table 8-2. The tensile strength is extrapolated, because the wire diameter is larger than in most application. The extrapolation can be found in Figure 8-7.

8-2-3 Attachment of power take-off mechanisms to pontoons

One of the requirements in Chapter 2 was that forces on the connections should be controllable (i.e. fully depend on damping and stiffness coefficients), to make sure that the mechanism does not break. The way to do this is to make the mechanism in such a way that the pontoons can move in all degrees of freedom. This can be done by attaching the PTO mechanisms to the pontoons by ball joints. This gives the pontoons the ability to rotate and translate in all

Table 8-2: Properties and computed parameters for the spring in the power take-off mechanism at dominant sea state. Top: Material properties. Middle: Spring requirements. Bottom: Computed spring parameters.

Parameter	Symbol	Value	Source
Tensile strength chromium silicon steel	σ_t	1.10 GPa	Extrapolated from [74]
Maximum shear stress for infinite life	τ'_{max}	$0.440\sigma_t$	[74]
Shear modulus	G	79.3 GPa	[74]
Spring stiffness	k_s	1.5×10^5 N/m	Table D-3
Maximum deflection	$s_{s,max}$	5 m	Section 8-2
Free length	L_0	8.13 m	Section 8-2-2
Spring index	c_s	9.78	Section 8-2-2
Maximum spring force	$F_{s,max}$	7.50×10^5 N	Equation (8-8)
Wahl factor	K_w	1.15	Equation (8-10)
Wire diameter	d_s	0.210 m	Equation (8-9)
Spring diameter	D_s	2.06 m	Equation (8-11)
Number of active windings	n_s	14.9	Equation (8-8)
Maximum pitch	$t_{s,max}$	0.882 m	Equation (8-12)

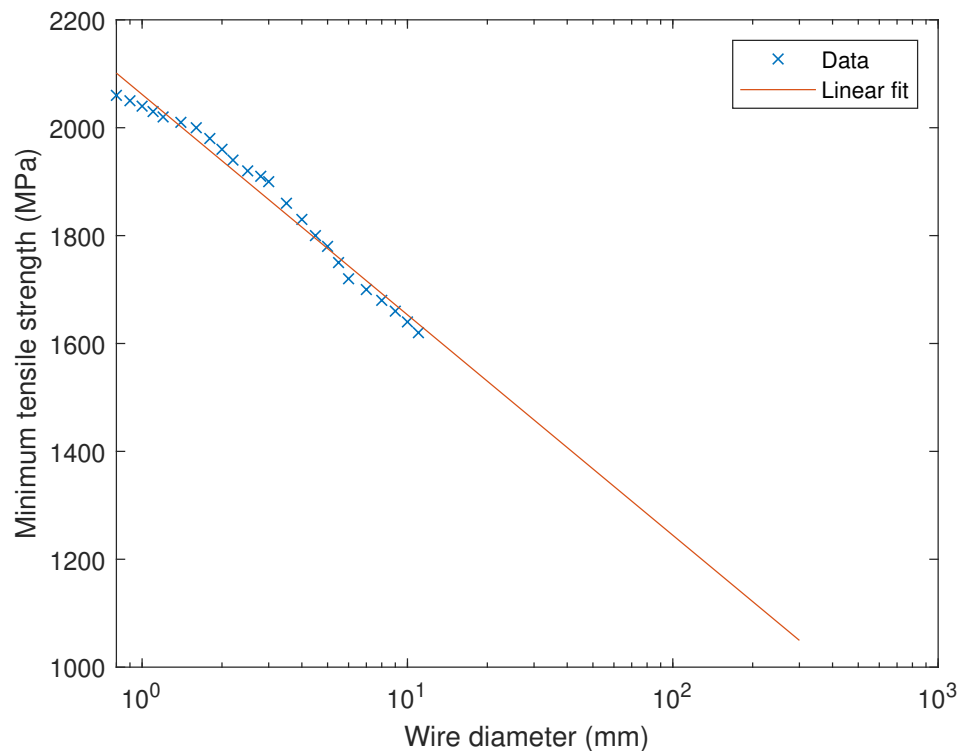


Figure 8-7: Data [74] and extrapolation for the minimum tensile strength of chromium silicon steel SAE J157.

directions with respect to each other.

To give an idea of how the whole array looks together with solar panels, a render can be found in Figure 8-8 and an overview of its parameters in Table 8-3.

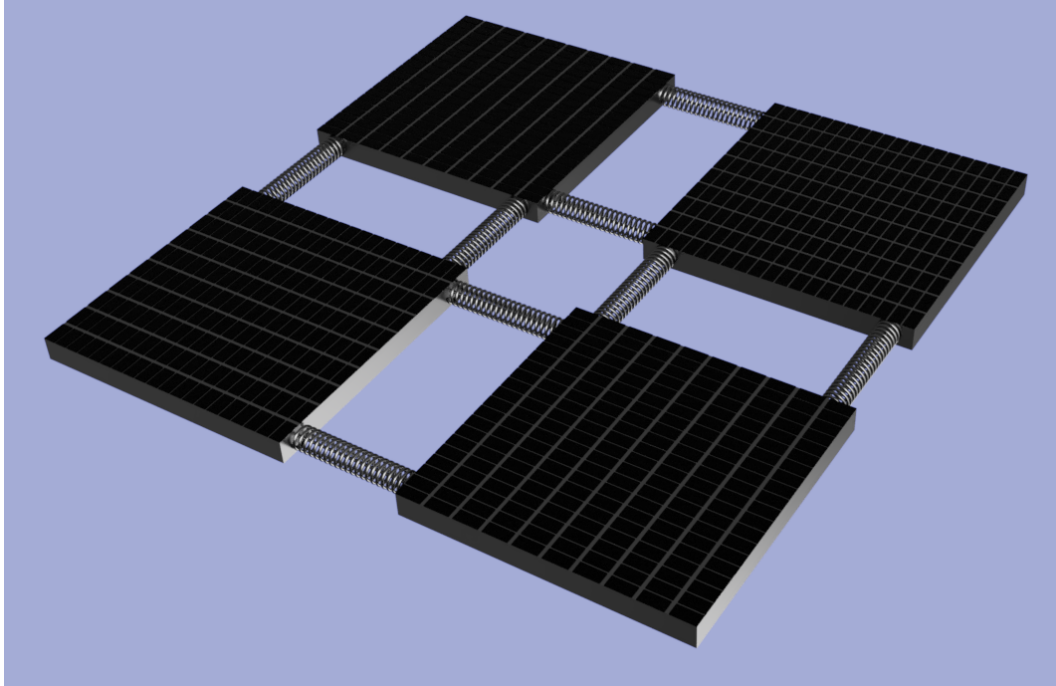


Figure 8-8: Render of a 2×2 array.

Table 8-3: Overview of array parameters.

Parameter	Value
Width of pontoon	23.0 m
Height of pontoon	2.00 m
Mass of pontoon	5.42×10^5 kg
Moment of inertia of pontoon in pitch and roll	2.40×10^7 kg m ²
Stiffness range of connections	$1.21-1.84 \times 10^5$ N/m
Damping range of connections	$1.38-7.55 \times 10^4$ N s/m

8-3 Energy capture

For the optimization runs in Chapter 6, the efficiency of the whole PTO mechanism was presumed as the same, i.e. the same efficiency holds for the spring and the damper. However, this is not true for the proof of concept in this chapter. For the hydraulic system, Cargo et al. [61] show that its efficiency is 0.8.

For springs however, no formulas exist yet to the best of this author's knowledge that can compute their efficiency by using spring parameters (such as dimensional and material properties). However, the efficiency of springs can be computed by using free decay experiments.

This is done in Appendix E. The efficiency of springs comes so close to 1.0, that it is assumed to be 1.0.

An efficiency of 1.0 for the springs and 0.8 for the hydraulic system means that the eigenfrequency is optimally tuned to the sea state, such as for the data in the top of Table 6-2, except for the sea states where the spring stiffness is too high or too low. For these sea states, energy capture of Resistive control (at the bottom of Table 6-2) will be used. The captured energy in the top table must be multiplied with 0.8 and the bottom with $\frac{0.8}{0.7}$ to get the actual usable energy in the form of electricity, because the efficiency was set to 1.0 and 0.7 respectively in these tables. The average electricity production can then be computed by calculating the weighted average of this usable energy per sea state and also taking other wave directions into account. Chapter 2 showed that 75% of the waves comes from the preferred direction. The energy capture for the other 25% will be lessened by a factor of $\frac{2.68}{3.44}$ as a crude estimation for all other directions than the preferred direction, which is the factor for power production of a 2×2 array under 45° waves found in Section 6-8. The average power production is then 1.56 kW/m along the wave crest that comes in contact with the pontoons at the preferred direction and 1.21 kW/m in the other directions. This adds up to a total average power of 77.8 kW (682 MWh yearly) for a 2×2 array, which is the equivalent of the electricity needs of 234 households in the Netherlands [77]. If solar panels with an efficiency of 20% would cover the whole surface of the four pontoons, a yield of 433 MWh on average would be expected. This was computed using the yearly solar irradiation in the Netherlands of 1.02 MWh/m² [78].

Conclusions and recommendations

9-1 Conclusions

The first part of the goal of this study was to make a system design of an efficient wave energy converter array of a type that is lacking research but has promise. Indeed, care has been given to optimize efficiency through design (for example spacing and size of the pontoons) and through control. It is possible to get even more power with the same amount of pontoons, by using rotary generators in addition to the linear generator for example, but practicality and some cost effectiveness has also been taken into account.

The second part of this study's goal was to implement, compare and evaluate scalable Resistive and Reactive control. Previously, all control for wave energy converters found in literature was done for devices that move vertically and are attached to the sea floor. It was therefore interesting to see that Reactive control can generate up to three times more energy than Resistive control. Distributed Reactive control was proposed and tested to combat the curse of dimensionality and reduces the computation time for arrays of large dimension.

It was found in simulation that the array performs average in the group of floating oscillating wave surge converters when Resistive control is used. However, when Reactive control is used, the threefold improved energy capture makes it possible for a 2×2 array to provide the electricity equivalent of 234 households in the Netherlands. The end result is a wave energy converter (WEC) array that harvests a great deal of energy.

9-2 Recommendations

Firstly, the system design made in this work is a recommended starting point for physical designs of WECs of this type. Together with this comes research into the best materials that can withstand sea water and anchoring of the array. A cost analysis would be very interesting for the economic viability, since revenue can be computed from this work, but costs remain unknown. The pontoons are a part of the system design that all physical designs will have in

common. The forces on these pontoons can already be computed, so a material choice and strength analysis can already be done without a physical design.

Secondly, experiments are recommended. It is the next step for model verification. Experiments can also unearth unexpected behaviour and give more insight into the system.

Thirdly, it was shown in Section 7-3 that more advanced control has the potential to improve energy capture between 15 and 50 %. It is thus a logical next line of research.

Fourthly, it was noticed that control papers are often not concerned with how the control input (the force of the power take-off (PTO) mechanism) can be realised in practice. Realizing the control input for energy harvesting systems is not trivial and it was settled on an approximation of the control input in this work for the proof of concept design. More advanced control will most likely also result in a more challenging control input to implement in real life. The design of a PTO mechanism that can freely vary its force and still be efficient could therefore be an interesting topic.

Optimal damping constants of simplified energy harvesters

This chapter shows that the energy production of a simplified energy harvester does not depend on the amount of displacement of generator. The optimal damping coefficients do change however. There are two situations that are compared in this chapter, first is a simplified energy harvester consisting of a mass damper system that is excited by a sinusoidal force, as depicted in Figure A-1a. Second is the same simplified system, but now the displacement of the generator is made different by a rack and pinion gear that is depicted in Figure A-1b. Power that is dissipated in the damper is seen as harvested energy.

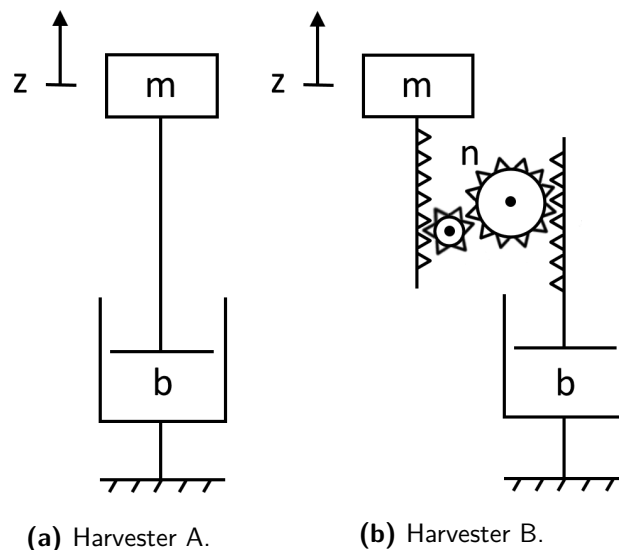


Figure A-1: Simplified energy harvesters with mass m , damping constant b , vertical displacement of mass z and gear ratio n .

A-1 Optimal damping constant for mass damper system A

The starting point of computing the optimal damping constant and the harvested energy is the equation of motion.

The force that excites the mass is given as: $G \cos(t)$, where G is the amplitude of the force and t is time.

The equation of motion for the mass damper system in Figure A-1a is then:

$$F = m\ddot{z} \quad (\text{A-1})$$

$$G \cos(t) + F_{damp} = m\ddot{z} \quad (\text{A-2})$$

$$G \cos(t) - b\dot{z} = m\ddot{z} \quad (\text{A-3})$$

Where b is the damping constant of the damper, m is the mass and z is the vertical displacement of the mass.

A steady state solution is proposed in the form of:

$$z = C \sin(t) - D \cos(t) \quad (\text{A-4})$$

The equation of motion with this solution changes into:

$$G \cos(t) = b(C \cos(t) + D \sin(t)) + m(-C \sin(t) + D \cos(t)) \quad (\text{A-5})$$

The steady state solution is correct if the following two equations hold:

$$G = bC + mD \quad (\text{A-6})$$

$$bD = mC \quad (\text{A-7})$$

Rewriting these to solve for C and D results in:

$$C = \frac{bG}{b^2 + m^2} \quad (\text{A-8})$$

$$D = \frac{mG}{b^2 + m^2} \quad (\text{A-9})$$

The optimal damping constant is computed by minimizing the total energy harvested (harvested energy is negative) for one cycle (2π s). It only needs to be optimized for one cycle because the steady state solution repeats this cycle. The captured energy E in one cycle is:

$$E_{cycle} = \int_0^{2\pi} P(t) dt = \int_0^{2\pi} F_{damp} \dot{z} dt = \int_0^{2\pi} -b\dot{z}^2 dt \quad (\text{A-10})$$

Using the steady state solution for z , the energy harvested per cycle becomes:

$$E_{cycle} = \frac{-\pi G^2 b}{b^2 + m^2} \quad (\text{A-11})$$

The energy per cycle is minimized when $b = m$:

$$E_{cycle} = \frac{-\pi G^2}{2m} \quad (\text{A-12})$$

To see if this is indeed correct, Matlab scripts were written to simulate the mass damper system (with random values for G and m) and b was optimized using the `fminsearch` optimizer [79]. The result of the optimizer was that $b = m$ is the correct optimum with the predicted energy per cycle.

A-2 Optimal damping constant for mass damper system B

The equation of motion for mass damper system B is the same as for A, except for the force of the damper (F_{damp}). The gear ratio of n makes the force applied on the mass by the damper n times greater and also makes the damper go with n times the speed. This results in the following equation of motion:

$$G \cos(t) + nF_{damp} = m\ddot{z} \quad (\text{A-13})$$

$$G \cos(t) - n^2 b \dot{z} = m\ddot{z} \quad (\text{A-14})$$

Following the same derivations as in Equations (A-4) to (A-10), the energy per cycle becomes:

$$E_{cycle} = \frac{-\pi G^2 n^2 b}{n^4 b^2 + m^2} \quad (\text{A-15})$$

This equation has its minimum at $b = \frac{1}{n^2}m$ and results in the same energy per cycle as in Equation (A-12).

The goal of this chapter was to prove that the two mass damper systems in Figure A-1 produce the same energy when optimized but have different damping values. It can be concluded that this is indeed the case.

Appendix B

Motion of generators for two different generator placements

This chapter shows that the motion of generators changes depending on where they are positioned. This means that the optimal damping constants will also change. Figure B-1 shows the two different generator layouts that will be considered.

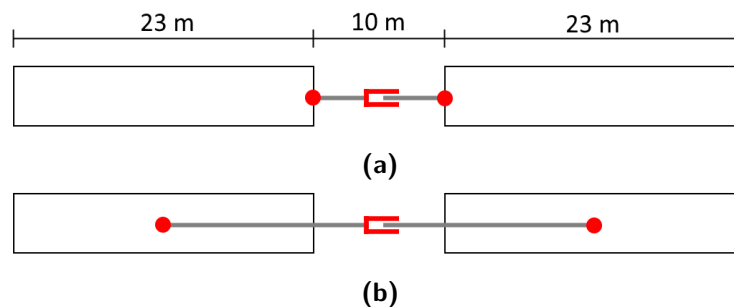


Figure B-1: Generator placement; (a) rotary generators on either end of the pontoons, (b) rotary generators in the middle of the pontoons.

Based on simulation results in Chapter 6, it is known that the pontoons move a maximum of ± 2.0 m horizontally (x), ± 1.0 m vertically (z) and ± 0.15 rad in pitch (θ). Table B-1 shows the amount of displacement in the generators when the pontoons move in the same or opposite direction. One can see that the displacement of the linear generator does not change much, as the largest motion is in the horizontal direction and this is the same for both layouts. However, there is a greater difference for the rotary generators. Generator layout (b) has less motion than (a), so the damping constants will have to be greater for (b) for the same amount of power.

Table B-1: Movement of pontoons that results in displacement of the generators. For generator motion, first number is a result of pontoons moving in opposite directions, second number in the same direction.

Generator layout	Pontoon movement	Linear generator displacement (m)	Rotary generator displacements (rad)
(a)	Horizontal: ± 2.0 m	4.0/0.0	0.0/0.0
	Vertical: ± 1.0 m	0.19/0.0	0.20/0.0
	Pitch: ± 0.15 rad	0.82/0.26	0.47/0.15
(b)	Horizontal: ± 2.0 m	4.0/0.0	0.0/0.0
	Vertical: ± 1.0 m	0.061/0.0	0.061/0.0
	Pitch: ± 0.15 rad	0.0/0.0	0.15/0.15

Appendix C

Computation of hydrostatic and gravitational stiffness coefficient in pitch

Figure C-1 shows a drawing of a pontoon that is submerged in water and has an angle in pitch (θ). The moment around the centre of mass (in the centre of the pontoon) can be computed with Archimedes' principle. The red and blue area's indicated in the figure are above and under water respectively when rotated and vice versa when in rest. This means that the resulting moment can be computed from the displaced water volume in these area's multiplied with their moment arm.

The displaced water volume (V) can be computed from the area of the blue and red triangles, which is the base of the triangle multiplied with its height divided by two:

$$V = \frac{1}{8}w^3 \sin(\theta) \quad (\text{C-1})$$

The moment arm can be computed from the point of application of the forces, which is the centre of mass (R_m) of those area's. For a triangle with uniform mass such as in Figure C-2, the centre of mass is $\frac{2}{3}$ along the horizontal axis.

The red and blue triangles are tilted at an angle, so the moment arms for each are $\frac{1}{2}w\frac{2}{3}\cos(\theta)$, with w being the width of the pontoon. The resulting moment M then becomes:

$$M = 2\rho_w g V \frac{1}{2}w\frac{2}{3}\cos(\theta) \quad (\text{C-2})$$

$$= \frac{1}{12}\rho_w g w^4 \sin(\theta)\cos(\theta) \quad (\text{C-3})$$

Where g is the gravitational acceleration of earth.

The hydrostatic and gravitational restoring coefficient in pitch can then be computed by linearising M at $\theta = 0$ rad :

$$\frac{dM}{d\theta} = \frac{1}{12} \rho_w g w^4 (\cos^2(\theta) - \sin^2(\theta)) \quad (\text{C-4})$$

$$\left. \frac{dM}{d\theta} \right|_{\theta=0} = \frac{1}{12} \rho_w g w^4 \quad (\text{C-5})$$

The linearised hydrostatic and gravitational stiffness coefficient as computed by Equation (C-5) for a pontoon with a width of 23 m is then 2.3449×10^8 N m/rad, which is a 1.28 % difference from what NEMOH computes.

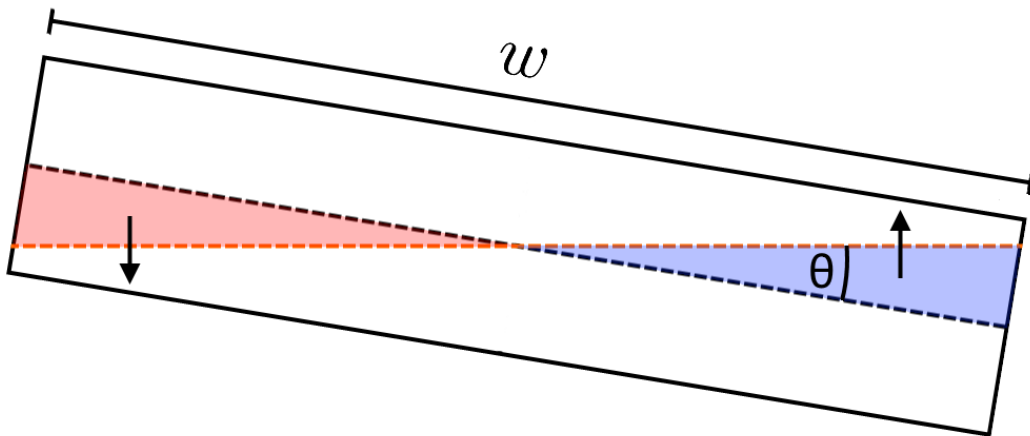


Figure C-1: Side view of a rotated pontoon in still water with hydrostatic and gravitational forces indicated by arrows. The orange dashed line indicates the water level. The blue area is above water when in rest, but under water when rotated and the red area is under water in rest, but is above water when rotated.

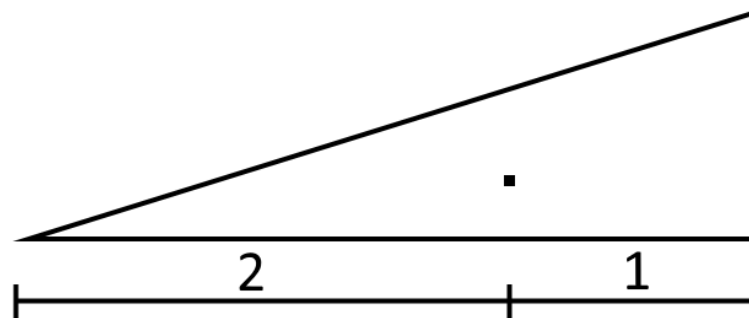


Figure C-2: Triangle and its center of gravity.

Appendix D

Extra Data

D-1 Ten consecutive optimization runs

Values for energy capture and control parameters for ten consecutive runs can be found in Table D-1. Simulations were done for a 2×1 array in random seas with $H_s = 2.25$ m, $T_p = 6.50$ s and a 0° wave direction.

D-2 Energy harvested per sea state

Table D-2 shows raw data for energy capture for all sea states that have a 1% or higher part in the total average energy in the waves. The control parameters were optimized for each sea state separately.

D-3 Spring and damping constants

Optimized spring and damping constants for Reactive control with an efficiency of 1.0 can be found in Table D-3 and Table D-4 respectively.

Table D-1: Overview of all found values for energy capture and control parameters for ten consecutive two hour long runs per control strategy. Simulated for a 2×1 array in random seas with $H_s = 2.25$ m, $T_p = 6.50$ s and a 0° wave direction.

Type of control	Energy (GJ)	K_p (N/m) 10^{-5}	K_d (N s/m) 10^{-5}
Reactive control Efficiency=1.00	1.17	2.99	0.554
	1.19	3.00	0.573
	1.17	3.01	0.573
	1.20	3.00	0.552
	1.20	3.01	0.559
	1.19	2.99	0.550
	1.19	2.99	0.554
	1.21	3.00	0.556
	1.15	2.99	0.572
	1.16	2.99	0.558
Reactive control Efficiency=0.700	0.486	2.57	1.69
	0.479	2.58	1.71
	0.479	2.58	1.70
	0.475	2.57	1.70
	0.496	2.58	1.70
	0.485	2.58	1.70
	0.478	2.58	1.70
	0.483	2.58	1.70
	0.477	2.58	1.70
	0.472	2.58	1.70
Resistive control Efficiency=0.700	0.247		3.30
	0.246		3.31
	0.244		3.31
	0.248		3.30
	0.246		3.31
	0.245		3.31
	0.241		3.32
	0.244		3.33
	0.245		3.32
	0.248		3.31

Table D-2: Overview of energy capture in two hours by a 2×1 array for random seas with 0° wave direction. Values are in GJ. Top: Reactive control with an efficiency of 1.0, middle: Reactive control with an efficiency of 0.7, bottom: Resistive control with an efficiency of 0.7.

H_s (m)	3.5-6.0				4.84	3.51	2.39
	3.0-3.5				2.26	1.73	
	2.5-3.0				1.79	1.66	
	2.0-2.5				1.18	1.15	
	1.5-2.0			0.447	0.722		
	1.0-1.5		0.0926	0.230	0.387		
	0.5-1.0	0.0288	0.0325	0.0818	0.132		
	3-4	4-5	5-6	6-7	7-8	8-9	9-10
	T_p (s)						

H_s (m)	3.5-6.0				1.98	1.51	1.08
	3.0-3.5				0.913	0.718	
	2.5-3.0				0.710	0.664	
	2.0-2.5				0.489	0.450	
	1.5-2.0			0.207	0.284		
	1.0-1.5		0.0397	0.0991	0.150		
	0.5-1.0	0.0104	0.0127	0.0359	0.0539		
	3-4	4-5	5-6	6-7	7-8	8-9	9-10
	T_p (s)						

H_s (m)	3.5-6.0				1.046	0.796	0.593
	3.0-3.5				0.469	0.368	
	2.5-3.0				0.376	0.331	
	2.0-2.5				0.254	0.218	
	1.5-2.0			0.111	0.149		
	1.0-1.5		0.0233	0.0548	0.0741		
	0.5-1.0	0.00500	0.00730	0.0190	0.0264		
	3-4	4-5	5-6	6-7	7-8	8-9	9-10
	T_p (s)						

Table D-3: Overview of optimized spring constants of a 2×1 array with an efficiency of 1.0 for random seas at a 0° wave direction. Values are in $\text{N/m} \times 10^5$.

H_s (m)	3.5-6.0					2.58	2.16	1.68
	3.0-3.5					2.42	1.99	
	2.5-3.0				3.04	2.41		
	2.0-2.5				2.99	2.42		
	1.5-2.0			3.68	2.98			
	1.0-1.5		7.06	3.67	2.98			
	0.5-1.0	8.30	7.03	3.68	2.97			
	3-4	4-5	5-6	6-7	7-8	8-9	9-10	
	T_p (s)							

Table D-4: Overview of optimized damping constants of a 2×1 array with an efficiency of 1.0 for random seas at a 0° wave direction. Values are $\text{Ns/m} \times 10^4$.

H_s (m)	3.5-6.0					4.80	4.25	4.53
	3.0-3.5					5.26	4.74	
	2.5-3.0				5.99	4.94		
	2.0-2.5				5.52	4.74		
	1.5-2.0			7.04	5.43			
	1.0-1.5		3.69	6.86	5.22			
	0.5-1.0	5.46	3.51	6.82	5.27			
	3-4	4-5	5-6	6-7	7-8	8-9	9-10	
	T_p (s)							

Appendix E

Efficiency of springs

The efficiency of springs can be computed with free decay experiments. In a free decay experiment, a mass with a spring attached to it is given an initial displacement and the amplitude is measured over time. The efficiency as used in Chapter 4 can be computed from these kind of experiments by first looking at how this efficiency affects energy going in and out of the power take-off (PTO) mechanism: Every time energy is going in or out of the PTO mechanism, the useful energy is lessened by a factor of the efficiency (energy is thus always ‘lost’). In one oscillation, the spring builds up or releases energy four times (see fig. E-1), which means that after one oscillation, the spring only has the amount of energy that was present in the beginning multiplied with the efficiency to the power of four. A formula for the amount of energy in a spring left at time t_1 after starting at t_0 (and thus having gone through $\frac{(t_1-t_0)\omega_n}{2\pi}$ oscillations) can then be formulated as:

$$E_s(t_1) = E_s(t_0)\eta_s^{4(t_1-t_0)\omega_n/(2\pi)} \quad (\text{E-1})$$

Where E_s is the energy in the spring, η_s is the spring efficiency, ω_n is the natural frequency and t is time. One should note that this only holds for complete cycles, i.e. $\frac{(t_1-t_0)\omega_n}{2\pi}$ should be an integer.

The maximum potential energy in an oscillating spring [74] is:

$$E_s(t) = 0.5K_p u_{max}^2(t) \quad (\text{E-2})$$

where u_{max} is the maximum displacement of the oscillating spring with respect to its resting position.

One can substitute Equation (E-2) in Equation (E-1) and rewrite it to compute η_s from the number of cycles and amplitudes measured in a free decay experiment:

$$0.5K_p u_{max}^2(t_1) = 0.5K_p u_{max}^2(t_0)\eta_s^{4(t_1-t_0)\omega_n/(2\pi)} \quad (\text{E-3})$$

$$\frac{u_{max}^2(t_1)}{u_{max}^2(t_0)} = \eta_s^{2(t_1-t_0)\omega_n/\pi} \quad (\text{E-4})$$

$$\left(\frac{u_{max}(t_1)}{u_{max}(t_0)}\right)^{\frac{\pi}{(t_1-t_0)\omega_n}} = \eta_s \quad (\text{E-5})$$

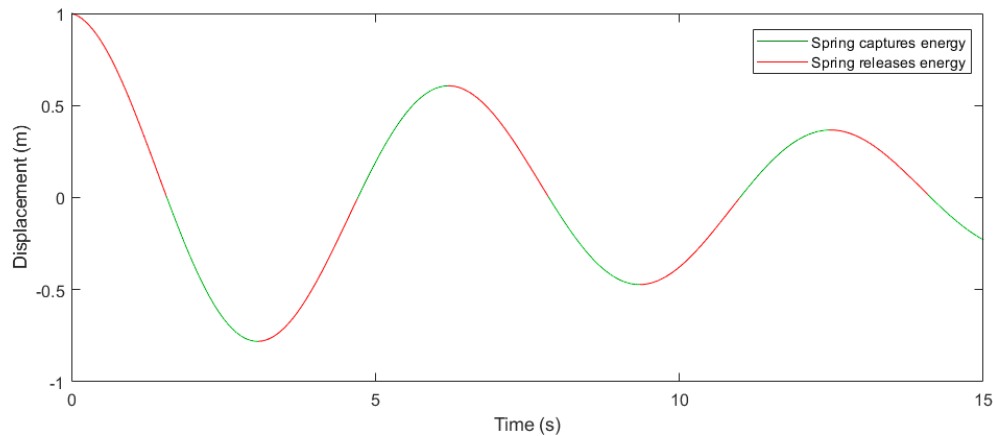


Figure E-1: Example of the displacement of an arbitrary spring with an efficiency of 0.78 after it is released from an initial position.

Free decay experiments with small springs and masses are done by Libii [80] and Triana and Fajardo [81]. They measure the amplitude of the displacement as a function of the amount of oscillations after an initial displacement. Libii [80] performs a free decay experiment three times with different masses. For the median mass, the initial displacement is 2.2 cm and goes to an amplitude of 0.2 cm in 1168 oscillations. The efficiency of that spring is thus $\left(\frac{0.2}{2.2}\right)^{0.5/1168} = 0.998$. The efficiency of that spring with the smallest and greatest mass are 0.999 and 0.997 respectively. Triana and Fajardo [81] perform free decay tests for multiple springs with different outer diameters to the same mass. What they find out is that the damping of springs goes down as the outer diameter increases. The efficiency of the smallest and greatest springs are 0.988 and 0.996 respectively. The springs of the PTO mechanism designed in Chapter 8 have a larger diameter to length ratio than the springs in the previous two experiments. This could mean that the efficiency will thus also be greater, but this cannot be said with certainty since other factors can influence the efficiency (such as wire thickness and the number of windings). However, since all springs in the experiments come very close to an efficiency of 1.0, it will be assumed for energy computation that the efficiency of the springs designed in Chapter 8 is 1.0.

Bibliography

- [1] J. Hansen, M. Sato, R. Ruedy, K. Lo, D. W. Lea, and M. Medina-Elizade, “Global temperature change,” *Proceedings of the National Academy of Sciences*, vol. 103, no. 39, 2006.
- [2] KNMI, “Temperatuur door historische grens van 40 graden Celsius,” 2019.
- [3] J. C. Stroeve, M. C. Serreze, F. Fetterer, T. Arbetter, W. Meier, J. Maslanik, and K. Knowles, “Tracking the Arctic’s shrinking ice cover: Another extreme September minimum in 2004,” *Geophysical Research Letters*, vol. 32, no. 4, pp. 1–4, feb 2005.
- [4] J. Cook, N. Oreskes, P. T. Doran, W. R. Anderegg, B. Verheggen, E. W. Maibach, J. S. Carlton, S. Lewandowsky, A. G. Skuce, S. A. Green, D. Nuccitelli, P. Jacobs, M. Richardson, B. Winkler, R. Painting, and K. Rice, “Consensus on consensus: A synthesis of consensus estimates on human-caused global warming,” *Environmental Research Letters*, vol. 11, no. 4, apr 2016.
- [5] M. K. van Aalst, “The impacts of climate change on the risk of natural disasters,” *Disasters*, vol. 30, no. 1, pp. 5–18, mar 2006.
- [6] Statistics Netherlands, “The Netherlands on the European scale,” Tech. Rep., 2019. [Online]. Available: <https://www.cbs.nl/en-gb/publication/2019/20/the-netherlands-on-the-european-scale-2019>
- [7] D. Magagna and A. Uihlein, *2014 JRC Ocean Energy Status Report*, 2015.
- [8] M. M. Kramer, L. Marquis, and P. Frigaard, “Performance Evaluation of the Wavestar Prototype,” in *Proceedings of the 9th European Wave and Tidal Conference*, 2011, pp. 5–9.
- [9] Wavestar Energy, “Concept | Wavestar,” 2019. [Online]. Available: <http://wavestarenergy.com/concept>
- [10] F. Ferri, S. Ambühl, B. Fischer, and J. P. Kofoed, “Balancing power output and structural fatigue of wave energy converters by means of control strategies,” *Energies*, vol. 7, no. 4, pp. 2246–2273, 2014.

- [11] C. B. Boake, T. J. T. Whittaker, M. Folley, and H. Ellen, "Overview and Initial Operational Experience of the LIMPET Wave Energy Plant," in *Proceedings of The Twelfth (2002) International Offshore and Polar Engineering Conference*, 2002.
- [12] I. Hashem, H. S. Abdel Hameed, and M. H. Mohamed, "An axial turbine in an innovative oscillating water column (OWC) device for sea-wave energy conversion," *Ocean Engineering*, pp. 536–562, 2018.
- [13] L. Hogervorst, "Ocean wave energy converter arrays - A review of devices and control," 2018.
- [14] B. Zanuttigh and E. Angelelli, "Experimental investigation of floating wave energy converters for coastal protection purpose," *Coastal Engineering*, vol. 80, pp. 148–159, 2013. [Online]. Available: <http://dx.doi.org/10.1016/j.coastaleng.2012.11.007>
- [15] C. Beels, P. Troch, J. P. Kofoed, P. Frigaard, J. Vindahl Kringelum, P. Carsten Kromann, M. Heyman Donovan, J. De Rouck, and G. De Backer, "A methodology for production and cost assessment of a farm of wave energy converters," *Renewable Energy*, vol. 36, no. 12, pp. 3402–3416, dec 2011. [Online]. Available: <http://dx.doi.org/10.1016/j.renene.2011.05.019><http://linkinghub.elsevier.com/retrieve/pii/S0960148111002473>
- [16] J. P. Kofoed, P. Frigaard, E. Friis-Madsen, and H. C. Sørensen, "Prototype testing of the wave energy converter wave dragon," *Renewable Energy*, vol. 31, no. 2, pp. 181–189, feb 2006. [Online]. Available: <http://linkinghub.elsevier.com/retrieve/pii/S0960148105002582>
- [17] F. Fusco, G. Nolan, and J. V. Ringwood, "Variability reduction through optimal combination of wind / wave resources - An Irish case study," *Energy*, vol. 35, no. 1, pp. 314–325, 2009. [Online]. Available: <http://dx.doi.org/10.1016/j.energy.2009.09.023>
- [18] H. Polinder, M. E. C. Damen, and F. Gardner, "Linear PM Generator System for Wave Energy Conversion in the AWS," *IEEE transactions on energy conversion*, vol. 19, no. 3, pp. 583–589, 2004.
- [19] Italgrou, "HCD Series hydraulic motor," 2019. [Online]. Available: <https://www.italgroup.eu/en/products/hydraulic-motors/swivelling-type/line/hcd-series/>
- [20] S. Wang, L. Lin, and Z. L. Wang, "Nanoscale triboelectric-effect-enabled energy conversion for sustainably powering portable electronics," *Nano Letters*, vol. 12, no. 12, pp. 6339–6346, 2012.
- [21] S. R. Anton and H. A. Sodano, "A review of power harvesting using piezoelectric materials (2003-2006)," *Smart Materials and Structures*, vol. 16, no. 3, pp. 1–21, 2007.
- [22] M. Mueller, "Electrical generators for direct drive wave energy converters," *IEE Proceedings - Generation, Transmission and Distribution*, vol. 149, no. 4, p. 446, 2002.
- [23] B. Drew, A. R. Plummer, and M. N. Sahinkaya, "A review of wave energy converter technology," *Proceedings of the Institution of Mechanical Engineers, Part A: Journal of Power and Energy*, vol. 223, no. 8, pp. 887–902, 2009.

- [24] M. S. Lagoun, A. Benalia, and M. E. Benbouzid, "Ocean wave converters: State of the art and current status," *2010 IEEE International Energy Conference and Exhibition, EnergyCon 2010*, pp. 636–641, 2010.
- [25] I. López, J. Andreu, S. Ceballos, I. Martínez De Alegría, and I. Kortabarria, "Review of wave energy technologies and the necessary power-equipment," *Renewable and Sustainable Energy Reviews*, vol. 27, pp. 413–434, 2013. [Online]. Available: <http://dx.doi.org/10.1016/j.rser.2013.07.009>
- [26] K. H. Mohamed, N. C. Sahoo, and T. B. Ibrahim, "A survey of technologies used in wave energy conversion systems," *Proceedings - 2011 International Conference on Energy, Automation and Signal, ICEAS - 2011*, pp. 594–599, 2011.
- [27] H. Titah-Benbouzid and M. Benbouzid, "Ocean wave energy extraction: Up-to-date technologies review and evaluation," *2014 International Power Electronics and Application Conference and Exposition*, pp. 338–342, 2014. [Online]. Available: <http://ieeexplore.ieee.org/document/7037878/>
- [28] K. E. Graves, D. Toncich, and P. G. Iovenitti, "Theoretical comparison of motional and transformer EMF device damping efficiency," *Journal of Sound and Vibration*, vol. 233, no. 3, pp. 441–453, 2000.
- [29] F. Geos, *Wind and wave frequency distributions for sites around the British Isles*. Great Britain, Health and Safety Executive, 2001.
- [30] C. Beels, J. C. C. Henriques, J. D. Rouck, M. T. Pontes, G. D. Backer, and H. Verhaeghe, "Wave Energy Resource in the North Sea," *7th European Wave and Tidal Energy Conference*, p. 10, 2007.
- [31] G. S. Payne, J. R. Taylor, and D. Ingram, "Best practice guidelines for tank testing of wave energy converters," *The Journal of Ocean Technology*, vol. 4, pp. 38–70, 2009.
- [32] J. N. Newman, *Marine hydrodynamics*. MIT press, 2017.
- [33] T. Hedges, "Regions of validity of analytical wave theories," in *Proceedings of the Institution of Civil Engineers-Water Maritime and Energy*, 1995.
- [34] A. Fournier and W. T. Reeves, "A simple model of ocean waves," *ACM SIGGRAPH Computer Graphics*, vol. 20, no. 4, pp. 75–84, aug 1986. [Online]. Available: <http://portal.acm.org/citation.cfm?doid=15886.15894>
- [35] NEMOH, "General notations and conventions," 2019. [Online]. Available: <https://lhea.ec-nantes.fr/software-and-patents/nemoh-theory-217704.kjsp>
- [36] Z. Liu and P. Frigaard, "Random seas," *Aalborg University*, 1997.
- [37] K. Hasselmann, T. P. Barnett, E. Bouws, H. Carlson, D. E. Cartwright, K. Enke, J. A. Ewing, H. Gienapp, D. E. Hasselmann, P. Kruseman, A. Meerburg, P. Muller, D. J. Olbers, K. Richter, W. Sell, and Walden, "Measurements of wind-wave growth and swell decay during the Joint North Sea Wave Project (JONSWAP)," *Deutsche hydrographische Zeitschrift*, 1973.

- [38] M. Folley, A. Babarit, B. Child, D. Forehand, L. O. Boyle, K. Silverthorne, J. Spinneken, V. Stratigaki, and P. Troch, "A Review of Numerical Modelling of Wave Energy Converter Arrays," in *ASME 2012 31st International Conference on Ocean, Offshore and Arctic Engineering*, 2012, pp. 535–545.
- [39] W. Cummins, "The impulse response function and ship motions," in *Symposium on Ship Theory at the Institut für Schiffbau der Universität Hamburg*, 1962.
- [40] M. Penalba, T. Kelly, and J. V. Ringwood, "Using NEMOH for Modelling Wave Energy Converters: A Comparative Study with WAMIT," in *Proceedings of the 12th European Wave and Tidal Energy Conference (EWTEC2017), Cork, Ireland*, 2017.
- [41] A. Babarit and G. Delhommeau, "Theoretical and numerical aspects of the open source BEM solver NEMOH," 2015. [Online]. Available: <https://hal.archives-ouvertes.fr/hal-01198800/>
- [42] A. J. Nambiar, D. I. Forehand, M. M. Kramer, R. H. Hansen, and D. M. Ingram, "Effects of hydrodynamic interactions and control within a point absorber array on electrical output," *International Journal of Marine Energy*, vol. 9, pp. 20–40, 2015. [Online]. Available: <http://dx.doi.org/10.1016/j.ijome.2014.11.002>
- [43] T. Perez and T. I. Fossen, "A Matlab Toolbox for Parametric Identification of Radiation-Force Models of Ships and Offshore Structures," *Modelling, Identification and Control*, vol. 30, no. 1, pp. 1–15, 2009.
- [44] M. L. Killi, "Hydrodynamic Interaction Among the pontoons of a Floating Bridge : Effect of Global Responses," Master Thesis, NTNU, 2018.
- [45] DNV GL, "Frequency domain hydrodynamic analysis of stationary vessels | Wadam," 2019. [Online]. Available: https://www.dnvgl.com/services/frequency-domain-hydrodynamic-analysis-of-stationary-vessels-wadam-2412?utm_campaign=structure_sesam&utm_source=google&utm_medium=cpc&gclid=EAIaIQobChMIutP3xa6C5QIV0-R3Ch22cQ86EAAYASAAEgITpPD_BwE
- [46] A. G. Abul-Azm and M. R. Gesraha, "Approximation to the hydrodynamics of floating pontoons under oblique waves," *Ocean Engineering*, 2000.
- [47] P. Andersen and H. Wuzhou, "On the calculation of two-dimensional added mass and damping coefficients by simple Green's function technique," *Ocean Engineering*, 1985.
- [48] J. A. Myers, *Handbook of equations for mass and area Properties of various geometrical shapes*, 1962.
- [49] L. Wang, J. Engström, M. Leijon, and J. Isberg, "Coordinated control of wave energy converters subject to motion constraints," *Energies*, vol. 9, no. 6, 2016.
- [50] K. J. Åström and H. Tore, *PID controllers: theory, design, and tuning*. Instrument society of America Research Triangle Park, NC, 1995.
- [51] J. A. Nelder and R. Mead, "A Simplex Method for Function Minimization," *The Computer Journal*, vol. 7, no. 4, pp. 308–313, 1965. [Online].

- Available: <https://academic.oup.com/comjnl/article-abstract/7/4/308/354237https://academic.oup.com/comjnl/article-lookup/doi/10.1093/comjnl/7.4.308>
- [52] S. Chen, J. Montgomery, and A. Bolufé-Röhler, “Measuring the curse of dimensionality and its effects on particle swarm optimization and differential evolution,” *Applied Intelligence*, pp. 514–526, 2015.
- [53] L. Han and M. Neumann, “Effect of dimensionality on the Nelder - Mead simplex method,” *Optimization Methods and Software*, vol. 21, no. 1, pp. 1–16, 2006.
- [54] F. Vázquez, F. Morilla, and S. Dormido, “An iterative method for tuning decentralized PID controllers,” *IFAC Proceedings Volumes*, vol. 32, no. 2, pp. 1501—1506, 1999.
- [55] K. J. Åström and R. M. Murray, *Feedback Systems*, 2009.
- [56] B. Ralph E, “Basic vibration theory,” in *Harris’ Shock and Vibration Handbook*, 1961.
- [57] A. Babarit, J. Hals, M. J. Muliawan, A. Kurniawan, T. Moan, and J. Krokstad, “Numerical benchmarking study of a selection of wave energy converters,” *Renewable Energy*, vol. 41, pp. 44–63, 2012. [Online]. Available: <http://dx.doi.org/10.1016/j.renene.2011.10.002>
- [58] A. Babarit, “A database of capture width ratio of wave energy converters,” *Renewable Energy*, vol. 80, pp. 610–628, 2015. [Online]. Available: <http://dx.doi.org/10.1016/j.renene.2015.02.049>
- [59] G. Li and M. R. Belmont, “Model predictive control of sea wave energy converters - Part II: The case of an array of devices,” *Renewable Energy*, vol. 68, pp. 540–549, 2014. [Online]. Available: <http://dx.doi.org/10.1016/j.renene.2014.02.028>
- [60] M. Starrett, R. So, T. K. Brekken, and A. McCall, “Increasing power capture from multibody wave energy conversion systems using model predictive control,” in *2015 IEEE Conference on Technologies for Sustainability (SusTech)*, 2015, pp. 20–26. [Online]. Available: <http://ieeexplore.ieee.org/document/7314316/>
- [61] C. J. Cargo, A. R. Plummer, A. J. Hillis, and M. Schlotter, “Determination of optimal parameters for a hydraulic power take-off unit of a wave energy converter in regular waves,” vol. 226, pp. 98–111, 2011.
- [62] P. Kalafetis and T. Costopoulos, “Modelling and simulation of an axial piston variable displacement pump with pressure control,” *Mechanism and Machine Theory*, vol. 30, no. 4, pp. 599–612, 1995.
- [63] H. Murrenhoff and E. Weishaupt, “Recent developments for the control of variable displacement motors with impressed pressure,” *Proceedings of the JFPS International Symposium on Fluid Power*, vol. 1996, no. 3, pp. 79–84, 1996.
- [64] G. Zeiger and A. Akers, “Dynamic Analysis of an Axial Piston Pump Swashplate Control,” *Proceedings of the Institution of Mechanical Engineers, Part C: Journal of Mechanical Engineering Science*, vol. 200, no. 1, pp. 49–58, 1986.

- [65] Hongliu Du and N. Manring, "A single-actuator control design for hydraulic variable displacement pumps," in *Proceedings of the 2001 American Control Conference*. (Cat. No.01CH37148). IEEE, 2001, pp. 4484–4489 vol.6. [Online]. Available: <http://ieeexplore.ieee.org/document/945685/>
- [66] Z. Shi, G. Parker, and J. Granstrom, "Kinematic analysis of a swash-plate controlled variable displacement axial-piston pump with a conical barrel assembly," *Journal of Dynamic Systems, Measurement and Control, Transactions of the ASME*, vol. 132, no. 1, pp. 1–8, jan 2010.
- [67] H. X. Chen, P. S. Chua, and G. H. Lim, "Dynamic vibration analysis of a swash-plate type water hydraulic motor," *Mechanism and Machine Theory*, vol. 41, no. 5, pp. 487–504, may 2006.
- [68] S. L. Nie, G. H. Huang, and Y. P. Li, "Tribological study on hydrostatic slipper bearing with annular orifice damper for water hydraulic axial piston motor," *Tribology International*, vol. 39, no. 11, pp. 1342–1354, nov 2006.
- [69] Liebherr, "Variable displacement motors," 2019. [Online]. Available: <https://www.liebherr.com/en/nzl/products/components/hydraulics/hydraulic-pumps-and-motors/axial-piston-motors-adjustable/axial-piston-motors-adjustable.html>
- [70] Saihydraulics, "Hydraulic Motor - Variable Displacement Motor," 2019. [Online]. Available: <http://www.saihydraulics.com/en/products/motors/variable-displacement/bv/?idC=61683&idCil=11863&idS=11600>
- [71] Parker, "Bent Axis Motors," 2019. [Online]. Available: <https://ph.parker.com/nl/en/bent-axis-motors>
- [72] Informa, "Engineering Essentials: Fundamentals of Hydraulic Pumps," 2019. [Online]. Available: <https://www.hydraulicspneumatics.com/200/TechZone/HydraulicPumpsM/Article/False/6401/TechZone-HydraulicPumpsM>
- [73] Leroy-Somer, "High-efficiency IE2 and Premium efficiency IE3 three-phase induction motors with aluminum frame," 2019. [Online]. Available: <https://acim.nidec.com/motors/leroy-somer/products/induction-motors/3-phase-motors-for-standard-applications/lse>
- [74] Society of Automotive Engineers, *Spring Design Manual*. SAE AE-21, 1982.
- [75] A. M. Wahl, *Mechanical springs*. Penton Publishing Company, 1963.
- [76] V. Jadon and S. Verma, *Analysis and Design of Machine Elements*, 2010.
- [77] Statistics Netherlands, "Trends in the Netherlands," 2018. [Online]. Available: <https://longreads.cbs.nl/trends18-eng/economy/figures/energy/>
- [78] W. G. J. H. M. Van Sark, L. Bosselaar, P. Gerrissen, K. Esmeijer, P. Moraitis, M. Van Den Donker, and G. Emsbroek, "Update of the dutch pv specific yield for determination of pv contribution to renewable energy production," in *29th European Photovoltaic Solar Energy Conference and Exhibition*, 2014. [Online]. Available: <http://statline.cbs.nl/statweb/>,

-
- [79] J. C. Lagarias, J. A. Reeds, M. H. Wright, and P. E. Wright, “Convergence Properties of the Nelder–Mead Simplex Method in Low Dimensions,” *SIAM Journal on Optimization*, vol. 9, no. 1, pp. 112–147, 1998.
- [80] J. N. Libii, “Demonstration of energy dissipation in a spring-mass system undergoing free oscillations in air,” *World Transactions on Engineering and Technology Education*, vol. 7, no. 1, pp. 28–33, 2009.
- [81] C. A. Triana and F. Fajardo, “Experimental study of simple harmonic motion of a spring-mass system as a function of spring diameter,” *Revista Brasileira de Ensino de Física*, vol. 4305, 2013.

Glossary

List of Acronyms

PTO	power take-off
WEC	wave energy converter
CWR	capture width ratio
OWSC	oscillating wave surge converter
GM	gain margin
PM	phase margin

List of Symbols

α	Effective damping (N s/m)
β	Wave direction (rad)
η	Wave elevation (m)
η_s	Spring efficiency
η_{hyd}	Hydrodynamic efficiency
λ	Wavelength (m)
ω	Frequency (rad/s)
ω_n	Natural frequency (rad/s)
ρ	Density (kg/m ³)
σ_t	Tensile strength (Pa)
τ	Uncorrected shear stress (Pa)
τ'	Corrected shear stress (Pa)
θ	Pitch (rad)

\mathbf{A}_M	Added mass (kg)
$\mathbf{B}(\omega)$	Added damping (N s/m)
\mathbf{C}	Hydrostatic and gravitational restoring coefficients matrix
$\mathbf{f}_{pto}(t)$	Force of power take-off mechanism (N)
$\mathbf{f}_{wave}(t)$	Wave force and torque (N and N m)
$\mathbf{k}(t)$	Radiation impulse response matrix (N/m)
\mathbf{M}	Mass matrix (kg)
\tilde{F}_e	Wave excitation force factor (N or N m)
A	Amplitude
A_m	Cross-sectional area of magnets (m ²)
A_p	Surface are of a hydraulic piston (m ²)
b	Damping constant (N s/m)
B_0	Magnetic flux density amplitude (T)
c_s	Spring index
d_m	Distance between two magnets with the same orientation (m)
D_s	Spring diameter (m)
d_s	Wire diameter (m)
d_w	Water depth
D_{hm}	Hydraulic motor displacement (L/rad)
E	Energy (J)
F	Force (N)
f	Frequency (Hz)
f_p	Peak frequency of wave spectrum (Hz)
G	Amplitude of force (N)
g	Gravitational acceleration of earth, 9.81 m/s ²
G_s	Shear modulus (Pa)
H	Height (m)
h	Height (m)
H_s	Significant wave height (m)
I_x	Moment of inertia in roll (kg m ²)
I_y	Moment of inertia in pitch (kg m ²)
k	Number of power take-off mechanisms in the array
k_s	Spring stiffness (N/m)
K_w	Wahl factor
L	Length (m)
L_0	Free length of spring (m)
M	Moment (N m)
m	Mass (kg)
N	Number of coil windings
n	Number of pontoons

n_s	Number of active spring coils
P	Power (W)
p	Pressure (Pa)
q	Number of generators
R	Resistance (Ω)
r	Radius (m)
R_m	Centre of mass (m)
s	Deflection (m)
T	Period (s)
t	Time (s)
T_p	Wave peak period (s)
t_s	Spring pitch (m)
T_{gen}	Generator torque (N m)
u	Displacement (m)
V	Volume (m ³)
v_m	Velocity of magnets (m/s)
w	Width (m)
x	Distance or displacement (m)
z	Distance or displacement (m)
<i>abs</i>	Absorbed
<i>damp</i>	Damper
<i>ext</i>	External
<i>e</i>	Excitation
<i>gen</i>	Generator
<i>hm</i>	Hydraulic motor
<i>hyd</i>	Hydrodynamic
<i>int</i>	Internal
<i>m</i>	Magnet
<i>pto</i>	Power take-off mechanism
<i>p</i>	Piston
<i>s</i>	Spring
<i>w</i>	Water

